System Integration of Flexible and Multifunctional Thin Film Sensors for Structural Health Monitoring

by

Andrew Robert Burton

A dissertation submitted in partial fulfillment
of the requirements for the degree of
Doctor of Philosophy
(Civil Engineering)
in the University of Michigan
2018

Doctoral Committee:

Professor Jerome P. Lynch, Chair
Professor Michael P. Flynn
Assistant Professor Branko Kerkez
Professor Victor C. Li
Associate Professor Kenneth J. Loh

Andrew R. Burton
arburt@umich.edu
ORCID iD: 0000-0003-3326-7724

© Andrew R. Burton
2018

DEDICATIONS

To my parents, Bob & Margaret Burton,
in appreciation of their guidance, example, and friendship.

ACKNOWLEDGEMENTS

Many have contributed to my education and development that has culminated in the completion of this work. Most importantly, my parents: Bob & Margaret Burton. Throughout my life they have contributed tremendous support and unconditional love as I have grown and worked toward various goals. They worked tirelessly and sacrificed to provide me with incredible opportunity and I will be forever grateful. I would also like to thank my sisters: Eleanor, Alison, Hilary, and Laurel. They have served as role models, provided encouragement, and advised me throughout my life. They, and now their families, are an incredible source of happiness and strength. My girlfriend, Rhani Franklin, was also great source of love and support during PhD process. It has been great to grow together through challenges and successes as we each begin our careers.

I benefitted greatly from the input of my advisor and friend Professor Jerome Lynch. He provided tremendous support and coaching throughout the PhD process. Professor Lynch has an incredible skillset that is complemented by great drive and passion for the work. This provided an exemplary model to follow as I grew as a researcher under his guidance. He also showed a great openness for allowing me to shape my own path and follow my own interests during my time in Ann Arbor. I will always appreciate his persistent passion for research and education and the continual effort he makes to best support his students.

I could not have completed the PhD process without many friendships that I value deeply. Supportive friends included peers from the University of Michigan, townies from around Ann Arbor, and others from around the country. The Michigan Rugby Football Club provided breaks from the lab, friendships, and memories that I will continue to treasure. Long-term friends from Kansas and California continue to provide perspective and encouragement. The most important resource to a graduate student is often other students. I had the pleasure of working alongside and learning from many great LISTers, LNF users, and GG Brown residents. I will miss the camaraderie, advice, and humor that were shared as we worked toward our degrees.

The completion of this research at the University of Michigan was also the result of efforts from other faculty and staff. I appreciate the time and advise from my dissertation committee throughout the final stages of the degree. I also benefitted from the efforts of the staff in the civil engineering department and Lurie Nanofabrication Facility. I am especially thankful for Pilar Herrera-Fierro who provided great technical and practical guidance as I learned a new field of engineering and navigated the PhD process. I also want to acknowledge the Center for Entrepreneurship (including Jonathan Fay and Aaron Crumm) for strengthening me as a professional and providing valuable insight into career opportunities.

My time at Michigan was a direct result of educators from my undergraduate degree at the University of California, Davis. Specifically, I would like to thank Professor Ken Loh (now at University of California, San Diego) for his instruction, mentoring, and the opportunities he provided. He provided an engaging research opportunity that ignited my interest and the mentoring to follow my resulting career goals. His impact was in tandem with the invaluable mentoring of Dr. Bryan Loyola, his doctoral student at the time, who introduced me to the research process and guided me through my first project. I also benefitted greatly from instruction, mentoring, and

guidance from many others in the Department of Civil and Environmental Engineering at Davis, for which I am grateful.

This research is supported by the National Science Foundation (NSF) under Grants CMMI-1436631 and CMMI-1362513. This research was additionally supported by the Office of Naval Research under Grant N00014-16-1-2738. Funding was also provided by the Michigan Space Grant Consortium (MSGC). I am also grateful for the funding that contributed to this work provided by NSF and the Japanese Society for the Promotion of Science (JSPS) for the East Asia Pacific Summer Internship (2013). Additional funding was provided by the University of Michigan.

TABLE OF CONTENTS

DEDICATIONS .... **ii**

ACKNOWLEDGEMENTS .... **iii**

LIST OF FIGURES .... **xi**

LIST OF TABLES .... **xvii**

ABSTRACT .... **xviii**

CHAPTER 1. INTRODUCTION **1**

1.1 NEED FOR SENSING IN CIVIL INFRASTRUCTURE 1

1.2 MEMS AND MICROSYSTEMS AS SENSING TECHNOLOGY DRIVERS 3

1.3 MULTIFUNCTIONAL MATERIALS AND FLEXIBLE ELECTRONICS 5

1.4 CNT-POLYMER COMPOSITE MATERIALS 7

1.5 APPLICATIONS OF SENSING STRAIN INCLUDING STRUCTURAL HEALTH MONITORING. 9

1.6 RESEARCH OBJECTIVES AND DISSERTATION OUTLINE 13

1.6.1 Design and Fabrication of Flexible RLC Primitives 13

1.6.2 Theory of Fabrication 14

1.6.3 Implementation of Thin Film Systems for a Variety of Strain Sensing Applications 15

1.6.4 Key Intellectual Contributions of This Work 17

CHAPTER 2. FABRICATION OF RLC PRIMITIVES AND METHODS FOR SYSTEM INTEGRATION **19**

2.1 INTRODUCTION 19

2.2 FABRICATION OF CNT-POLYMER THIN FILM COMPOSITES 20

2.2.1 Layer-By-Layer Fabrication Method *20*

2.2.2 Lithographic Patterning of CNT-Polymer Composites *22*

2.2.3 Illustration: Strain Sensitive Thin Film Resistors of Various Widths *25*

2.3 UTILIZATION OF METALS FOR THIN FILM SYSTEMS 32

2.3.1 Metal Patterning Using Optical Lithography *32*

2.3.2 Etching of Metal Layers *32*

2.3.3 Electroplating Gold and Copper for Metal Layers *33*

2.3.4 Illustration: Fabrication of Thin Film Inductors *33*

2.4 FABRICATION METHODS FOR POLYIMIDE AS A SUBSTRATE AND DIELECTRIC LAYER 35

2.4.1 Polyimide Substrate Fabrication *35*

2.4.2 Reactive Ion Etching of Polyimide *36*

2.4.3 Polyimide Surface Preparation for Metal or CNT-Polymer TF Deposition *37*

2.4.4 Illustration: Fabrication of Thin Film Capacitors *38*

2.5 INTEGRATION OF DISSIMILAR SYSTEM COMPONENTS AND RAPID RESEARCH PROTOTYPING 39

2.5.1 Integration of Dissimilar Components *40*

2.5.2 Shadow Masking for Rapid Prototyping *42*

2.6 CHAPTER SUMMARY 42

CHAPTER 3. FULLY INTEGRATED CARBON NANOTUBE COMPOSITE THIN FILM STRAIN SENSORS ON FLEXIBLE SUBSTRATES FOR STRUCTURAL HEALTH MONITORING 45

3.1 INTRODUCTION 45

3.2 FABRICATION OF CNT-POLYMER THIN FILM SENSORS AND INTEGRATED ELECTRONICS ON FLEXIBLE SUBSTRATE 49

3.2.1 Materials *49*

3.2.2 Overview of the Fabrication Process *50*

3.2.3 Substrate Preparation *52*

3.2.4 *Metal Stack Fabrication* 54

3.2.5 *Layer-By-Layer Film Fabrication* 57

3.2.6 *System Construction* 58

3.2.7 *Process Yield* 60

3.3 FILM CHARACTERIZATION 60

3.4 EXPERIMENTAL VALIDATION 65

3.5 MONITORING A STEEL BEAM-COLUMN UNDER LATERAL LOADING 70

3.6 CHAPTER SUMMARY 75

CHAPTER 4. POLYMER NANOCOMPOSITE RESISTIVE ARRAYS FOR SPATIAL STRAIN SENSING 78

4.1 INTRODUCTION 78

4.2 FABRICATION OF PATTERNED CNT-POLYMER THIN FILM ARRAY 81

4.2.1 *Materials* 81

4.2.2 *Layer-By-Layer Film Fabrication* 81

4.2.3 *Overview of System Fabrication Process* 82

4.2.4 *System Instrumentation* 83

4.3 INVERSE ALGORITHM FOR RESISTIVE ARRAY 83

4.3.1 *Kirchhoff Equations for Resistor Network* 85

4.3.2 *Reordering of Node Numbers* 86

4.3.3 *Schur Complement of* $\boldsymbol{K^*}$ 86

4.3.4 *Moore-Penrose Pseudoinverse of* $\boldsymbol{\Gamma}$ 86

4.3.5 *The Jacobian Matrix* 87

4.3.6 *Determine the Partial Derivative of* $\boldsymbol{\Gamma}$ 87

4.3.7 *Linear Approximation and the Jacobian* 88

4.4 EXPERIMENTAL TESTING 89

4.4.1 *Data Acquisition for Resistive Array* 89

4.4.2 *Validation of Resistive Array Algorithm for Thin Film System* 90

4.4.3 *Illustration of Resistive Array in SHM Application* ... *91*

4.5 RESULTS AND DISCUSSION ... 92

4.5.1 *Validation of Resistive Array EIT Algorithm* ... *92*

4.5.2 *Illustration of Resistive Array in SHM Application* ... *95*

4.6 CHAPTER SUMMARY ... 99

CHAPTER 5. FUSED RFID STRAIN SENSOR FOR STRUCTURAL HEALTH MONITORING ... 101

5.1 INTRODUCTION ... 101

5.2 DESIGN AND FABRICATION ... 104

5.2.1 *Thin Film LCR Components* ... *104*

5.2.2 *Fused Sensors for Strain Sensing* ... *108*

5.2.3 *Wireless Strain Threshold Sensing System* ... *110*

5.3 EXPERIMENTAL TESTING ... 112

5.3.1 *Thin Film LCR Components* ... *112*

5.3.2 *Fused Sensors for Strain Sensing* ... *113*

5.3.3 *Wireless Strain Threshold Sensing System* ... *114*

5.4 RESULTS AND DISCUSSION ... 115

5.4.1 *Thin Film LCR Components* ... *115*

5.4.2 *Fused Sensors for Strain Sensing* ... *117*

5.4.3 *Wireless Strain Threshold Sensing System* ... *124*

5.5 CHAPTER SUMMARY ... 129

CHAPTER 6. CONCLUSION ... 131

6.1 SUMMARY AND THESIS CONTRIBUTIONS ... 131

6.1.1 *Fabrication of RLC Primitives and Methods for Integration in Thin Film Sensors* ... *132*

6.1.2 *Fully Integrated Carbon Nanotube Composite Thin Film Strain Sensors on Flexible Substrates for Structural Health Monitoring* ... *132*

6.1.3 *Scaling Nanocomposites to Sense Strain Over Large-Areas* ... *134*

6.1.4 Wireless Inductive Strain Sensor..*136*

6.2 FUTURE WORK 137

REFERENCES.. 139

LIST OF FIGURES

Figure 1-1. Enabling technologies for structural health monitoring. 10

Figure 2-1. LbL thin film fabrication process. 21

Figure 2-2. Fabrication flow for patterning fibrous LbL films. 23

Figure 2-3. Fabrication stages for small-scale sensing skins: (a) polyimide on glass slide; (b) CNT thin film covering PR and polyimide on slide; (c) patterned CNT sensing skin with sensing elements of thickness 100, 250, 500, 1000, and 1500 microns from left to right as fabricated and tested; (d) polyimide substrate epoxy bonded to PVC coupon with silver colloidal paste used to attach electrodes. 26

Figure 2-4. Images of patterned sensors magnified at 20x showing some limited roughness along patterned film edges. 29

Figure 2-5. Change in resistance under cyclic loading for sensing elements of thickness: (a) 10 microns; (b) 250 microns; (c) 500 microns; (d) 1000 microns; (e) 1500 microns; (f) measured specimen strain using a tradition strain gage. 30

Figure 2-6. Electrical properties of sensing elements: (a) Initial resistance; (b) gage factor. 31

Figure 2-7. (a) Image of fabricated inductor and (b) phase and impedance curves for TF inductor. 34

Figure 2-8. Image (a) and phase and impedance curves (b) for a thin film capacitor of 10 mm side length. 39

Figure 3-1. Process flow for fully integrated thin film sensing systems. 51

Figure 3-2. Metal stack design durable to process parameters. 55

Figure 3-3. Substrate at various stages during fabrication: (a) layout of patterned thin film and metal stack; (b) patterned SWNT-PSS/PVA thin film (black strips) on top of metal stack and polyimide; (c) complete sensor. 56

Figure 3-4. Schematic of the Wheatstone bridge circuit of the fully integrated CNT thin film strain sensor (with reference surface mount resistors, R_{ref}, and strain-sensitive thin film resistors, R_s). 57

Figure 3-5. (a) Optical microscope view of CNT thin film sensor connection to bond pad on polyimide (PI) substrate; (b) optical microscope view of patterned CNT thin film on PI; (c) and (d) SEM image of CNT patterned film at perimeter where tearing mechanisms are evident. 61

Figure 3-6. Optical microscope images of 10 micron wide SWNT-PSS/PVA thin film: (a) patterned thin film at the bond pad; (b) away from the bond pad area. 62

Figure 3-7. Profilometer showing film thickness at three locations on each SWNT-PSS/PVA patterned film (termed “strips”). Measurements are taken at the top, middle, and bottom of each sensor are indicated (x) while the mean is indicated with a circle (note that each strip on slide 1 bridge 1 was limited to two data points due to film damage). 63

Figure 3-8. (a) Schematic and (b) photograph of load frame used to test sensors. 64

Figure 3-9. Fully integrated strain sensor behavior: time history of strain (measured by metal foil gage) and change in output voltage of Sensor 2 for (a) 4 cycles of ± 500 με, (c) four cycles of ± 3000 με, and (e) two cycles of ± 3000 με with pause at the second tensile peak; corresponding output voltage versus measured strain for (b) 4 cycles of ± 500 με, (d) four cycles of ± 3000 με, and (f) two cycles of ± 3000 με with pause at the second tensile peak. 67

Figure 3-10. Sensor 4 strain time history of measured strain (by metal foil gage) and fully integrated sensor output voltage: (a) from 0 to 1000 seconds; (b) from 700 to 1000 seconds. 68

Figure 3-11. Sensor 5 loaded to failure: (a) strain time history of measured strain (by metal foil gage) and fully integrated sensor output voltage; (b) corresponding output voltage versus measured strain for load cycle to 5,000 microstrain; (c) sensor functioning with nonlinearity in final load cycle; (d) linearity of sensor as strain is increased to failure. 69

Figure 3-12. (a) Steel frame test assembly for cyclic load testing; (b) two prototype fully integrated strain sensors were located on the beam web near the bottom flange 13.8 in. (35 cm) from the edge of the column. 71

Figure 3-13. Web strain of steel beam-column assembly under cyclic loading: (a) metal foil measured strain and fully integrated strain sensor output time histories and (b) corresponding output voltage versus strain as measured 0.87 in. (22 mm) above the flange at 2% column displacement; (c) metal foil measured strain and fully integrated strain sensor output time histories and (d) corresponding output voltage versus strain as measured at 3% column displacement. 72

Figure 3-14. Fully integrated sensor observing damage on steel structure: (a) time history of fracture event as measured by prototype fully integrated strain sensor and traditional metal foil gage; (b) strain sensor output versus strain during fracture event; (c) failure point in test loading procedure; (d) image of beam flange fracture observed. 74

Figure 4-1. Design layout of electrodes and CNT sensing array. 82

Figure 4-2. Rectangular resistor network schematic. 85

Figure 4-3. Nodal details for assembling Kirchhoff matrix. 85

Figure 4-4. Custom circuit board and terminal block utilized for data acquisition. 89

Figure 4-5. Resistor network tested for algorithm validation. 90

Figure 4-6. Photos of (a) fabricated sensing grid with wires connected for measuring resistance prior to bridging electrodes, (b) standalone sensing skin prior to testing, and (c) schematic of numbering of sensors and nodes. 91

Figure 4-7. Film sensors bonded to PVC bars at the angles of (a) 0° and (b) 45° for mechanical testing. 91

Figure 4-8. True values and algorithm estimates of conductance values in two resistor networks. 92

Figure 4-9. True values and algorithm estimates of 60 bilayer nanocomposite sensor array. 94

Figure 4-10. Testing loading procedure (a) and cost function on each iteration for sensor at 0° to strain direction. 94

Figure 4-11. Conductance response of array sensors aligned on the x-axis along strain direction during 0° test. 96

Figure 4-12. Conductance response of array sensors aligned on the y-axis during 0° test. 96

Figure 4-13. Testing loading procedure (a) and cost function on each iteration for sensor at 45° to strain direction. 97

Figure 4-14. Conductance response of sensors aligned on rotated x-axis during 45° test. 98

Figure 4-15. Conductance response of sensors aligned on rotated y-axis during 45° test. 98

Figure 5-1. Illustration of capacitor strain sensitivity. 104

Figure 5-2. Fabrication process flow of capacitor. 105

Figure 5-3. Planar design of square coil inductor. 106

Figure 5-4. Fabrication process flow for the copper thin film inductor. 107

Figure 5-5. Fuses tested for use in empirical design. 109

Figure 5-6. Fuse fabrication process flow. 109

Figure 5-7. System layout for wireless threshold strain sensor. 110

Figure 5-8. System fabrication flow. Note that step six shows a different cross section than previous steps to illustrate fuse fabrication. 111

Figure 5-9. Loading procedure for testing fused sensors under increasing strain in tension. 113

Figure 5-10. Loading procedure for testing fused sensors under cyclic loading of increasing strain magnitudes. 113

Figure 5-11. Illustration of wireless sensor readout. 114

Figure 5-12. Loading procedure for LC sensing system. 115

Figure 5-13. Capacitor values for parallel plates of varying side length. 115

Figure 5-14. Mechanical testing of capacitors with side lengths of (a) 10 mm, (b) 4 mm, and (c) 2 mm. 116

Figure 5-15. Copper thin film inductor (a) photo after fabrication and (b) phase and impedance curves for inductor characterization. 117

Figure 5-16. Tensile and compressive testing of fused sensors fabricated with an AE Evaporator sensor 1 (a) test 1 and (b) test 2 and sensor 2 (c) test 1 and (d) test 2. 117

Figure 5-17. Tensile and compressive testing of fused sensors fabricated with an Enerjet Evaporator sensor 1 (a) test 1 and (b) test 2 and sensor 2 (c) test 1 and (d) test 2. 119

Figure 5-18. Example fuse response to strain over first loading cycle for fuse with (a) width of 0.5 mm, length of 1 mm, and thickness of 100 nm and (b) width of 0.5 mm, length of 1 mm, and thickness of 200 nm. 120

Figure 5-19. Yield points of sensors tested. 120

Figure 5-20. Two cycle loading test showing behavior of fuses at high and repeated strains. 121

Figure 5-21. Plot showing strain at which 2x, 10x, and 20x initial resistance (x-axis) is reached. Default design values (w=500 nm, L=1 mm, th=200 nm) are plotted in (a), width is altered to 100 nm in (b) and 1 mm in (c). Length 123

is altered to 100 nm in (d) and 2 mm in (e). Thickness is altered to 100 nm in (f) and 300nm in (g).

Figure 5-22. Picture of sensing system. 124

Figure 5-23. Microscope images of fuse point (a) and (b), corner of capacitor (c), and inductor copper (d). 125

Figure 5-24. (a) Phase of read inductor with and without a sensing system in the proximity of the read inductor. 126

Figure 5-25. Phase response of the (a) reference peak and (b) fuse peak responding to tensile strain during initial loading. 126

Figure 5-26. Phase response of the (a) reference peak and (b) fuse peak responding to tensile strain under a second progression of tensile loading. 127

Figure 5-27. Frequency peak vs strain of the reference LC circuit. 128

LIST OF TABLES

Table 3-1. Initial resistance of CNT films, bridged sensor sensitivity, linearity, and limit strains for the five sensors tested (note that positive strain is tensile strain). 66

Table 4-1. Recognized conductance in the resistor network subjected to various current injection patterns. 95

ABSTRACT

Greater information is needed on the state of civil infrastructure to ensure public safety and cost-efficient management. Lack of infrastructure investment and foreseeable funding challenges mandate a more intelligent approach to future maintenance of infrastructure systems. Much of the technology currently utilized to assess structural performance is based on discrete sensors. While such sensors can provide valuable data, they can lack sufficient resolution to accurately identify damage through inverse methods. Alternatively, technologies have shown promise for distributed, direct damage detection with flexible thin film and multifunctional polymer-nanocomposite materials. However, challenges remain as significant past work has focused on material optimization as opposed to sensing systems for damage detection. This dissertation offers novel methods for direct and distributed strain sensing by providing a fabrication methodology for broadly enabling thin film sensing technologies in structural health monitoring (SHM) applications. This fabrication methodology is presented initially as a set of materials and processes which are illustrated in analog circuit primitive forms including flexible, thin film capacitors, resistors, and inductors. Three sensing systems addressing specific SHM challenges are developed from this base of components and processes as specific illustrations of the broader fabrication approach.

The first system developed is a fully integrated strain sensing system designed to enable the use of multifunctional materials in sensing applications. This is achieved through the development of an optimized fabrication approach applicable to many multifunctional materials. A layer-by-layer (LbL) deposited nanocomposite is incorporated with a lithography process to produce a sensing system. To illustrate the process, a strain sensing platform consisting of a

nanocomposite film within an amplified Wheatstone bridge circuit is presented. The study reveals the material process is highly repeatable to produce fully integrated strain sensors with high linearity and sensitivity. The thin film strain sensors are robust and are capable of high strain measurements beyond 3,000 $\mu\epsilon$.

The second system developed is an array of resistive distributed strain sensors and an associated algorithm to provide an alternative to electrical impedance tomography for spatial strain sensing. An LbL deposited polymer composite thin film is utilized as the piezoresistive sensing material. An inverse algorithm is presented and utilized for determining the resistance of array elements by electrically stimulating boundary nodes. Two polymer nanocomposite arrays are strain tested under cyclic loading. Both arrays functioned as networks of strain sensors confirming the viability of the approach and computational benefits for SHM.

The third system developed is a thin film wireless threshold strain sensor for measuring strain in implanted and embedded applications. The wireless sensing system is comprised of two thin film, inductor-capacitor circuits, one of which included a fuse element. The sensor is fabricated on polyimide with metal layers used to pattern inductive antennas and a strain sensitive parallel plate capacitor. A titanium thin film fuse is designed to fail, or have a large resistance increase, when a strain threshold is exceeded. Three prototype systems are interrogated wirelessly while under increasing tensile strain. One of two sensor resonant peaks disappear at a strain threshold as designed, validating the sensing approach and thin film form for use in SHM systems. The fuse approach provides a platform for various systems and sensing elements. The reference peak remains intact and is used for continuous real-time strain sensing with a sensitivity of 0.5 and a noise floor below 50 microstrain.

CHAPTER 1.

INTRODUCTION

1.1 Need for Sensing in Civil Infrastructure

Greater information is needed on the state of civil infrastructure systems to ensure their continued use is safe and maintenance is cost-effective. This is clear from a broad perspective as America's infrastructure recently received a D+ from the American Society of Civil Engineers (ASCE) in the 2017 report card (performed every four years) [1]. The low grade is indicative of a general lack of investment in the nation's infrastructure such as bridges, levees, pipelines, dams, and roads. Lack of investment and maintenance has led to potentially serious deterioration of critical infrastructure systems. Lack of funding also means infrastructure is increasingly being used beyond intended design lives specified as the period over which engineers can ensure adequate structural performance at reasonable maintenance costs. The associated threat to public safety and continued limitations on funds for infrastructure require a paradigm shift in how we approach and solve the challenge of aging infrastructure. Infrastructure asset managers need greater information to inform them of when a critical structure is at risk. They also need to make maintenance and rehabilitation decisions with limited funds. Current attempts at garnering such information include manual visual inspection of structures and point-sensing on a limited basis. Manual inspection in the form of visual investigation is expensive, time consuming, and subjective as individual

inspectors travel to infrastructure assets and provide qualitative information on visible components of the structure [2]. Today, visual inspection covers the majority of management methods used. However, structural monitoring is emerging as an option. Point sensors, such as strain gages, only observe structural behavior on a very limited area of the structure and are likely to miss signs of damage unless the point sensor is very close spatially to the damage site. Also, data collected often is used as input to inverse methods that infer damage based on measured structural responses. This approach has proven difficult to pursue due to the ill-posed nature of the problem [3].

The situation clearly lays out a need for better information gathering to identify potential damage in a structure, to characterize the structural state, and finally to prescribe actionable structural maintenance for a decision maker. Without advances toward such capabilities, aging infrastructure will continue to require resources while public safety will be less certain.

This compelling need has led many researchers to attempt to address the challenge of structural health monitoring (SHM) of civil structures. The following sections will discuss research trends relevant to SHM and present pressing needs for achieving SHM in practice. First, various advances in sensing technologies that have advanced the potential for structural health monitoring since the inception of the field will be discussed. Sensing advances include the proliferation of microelectromechanical systems and the vast set of fabrication technologies native to the MEMS field. Additionally, progress in multifunctional materials and flexible electronics have allowed for advanced design of sensing materials and capabilities in forms previously unattainable. These trends will be discussed broadly then their implications for improved sensing will be illustrated through a deep discussion of the application of carbon nanotube-based polymer composites as sensors. Existing approaches to SHM will be discussed and the merits of various methodologies

considered. Finally, a path for advancing SHM through the integration of new materials and technologies is presented.

1.2 MEMS and Microsystems as Sensing Technology Drivers

Microelectromechanical systems (MEMS) are systems of integrated mechanical and electrical components fabricated (typically in silicon) with features at the micron-scale [4]. These systems generally include sensors or actuators, data acquisition or drive circuitry, and interfaces to higher-level control. The field of MEMS emerged as engineers modified fabrication technologies associated with integrated circuits (IC) and created new fabrication technologies to realize miniaturized mechanical devices such as sensors. MEMS advances have included miniaturization of devices, lowered manufacturing cost through parallel fabrication, improved interface and calibration for integrated microsystems, and benefits to fundamental science.

MEMS sensors and actuators are created through a design process that must account for system layout, fabrication processes, and testing. Transducer layout must consider the function of components as mechanical, electrical, or both mechanical and electrical in MEMS devices and design. Additionally, MEMS are commonly laid out with monolithic integration to nearby IC electronics, resulting in smaller system sizes and improved sensing performance. These are created using a trove of fabrication processes anchored by additive fabrication processes, subtractive fabrication processes, patterning, material modification, and packaging [5]. Perhaps most characteristic of MEMS is patterning using photolithography where a polymer is spun on a substrate, selective areas are exposed to light, and then exposed areas are removed so that a stencil-like mask has been created [4]. Additive processes include evaporation and sputtering of metals among other processes. Subtractive processes are the removal of materials through wet (or chemical) methods or dry (often reactive ion plasma) etching. Providing the packaging,

electronics, and environment to test sensors can also be an involved task that must be accounted for in initial MEMS designs. This necessary systems approach to MEMS designs has served certain silicon MEMS devices especially well.

Advances in MEMS have been complemented by advances in computing through Moore's law [6] and wireless communication [7] to culminate in greatly improved capabilities for sensors and sensing systems built with MEMS sensors. The cumulative result is that sensors and sensor networks are far more capable and affordable than in recent history. This has influenced many fields of engineering as new capabilities for collecting information on the state of systems and processing this information for actionable intelligence emerge.

The MEMS field has grown and matured to the present day to provide a vast number of exciting technologies influencing many application areas. For example, one set of transducers illustrating the achievements of MEMS are navigation sensors including accelerometers and gyroscopes such as the complementary metal-oxide-semiconductor (CMOS) capacitive sensing amplified accelerometer by Wu et al. fabricated using a monolithic process and micromachining [8]. A second example set of sensors is force and strain sensors such as the resonant strain sensor by Azevedo et al. constructed with silicon carbide for harsh sensing environments [9]. A third example class illustrating MEMS is display technologies such as the digital micromirror display by Texas Instruments that utilize highly repeatable lithography and array-based MEMS processes to create arrays of hinged mirrors for high definition light projection which led to commercial success of digital projectors [10]. As a whole, the impact of MEMS on miniaturizing sensors, lowering sensor cost, and improving sensor performance has offered society vastly enhanced capabilities for obtaining information from the world around us. This has also resulted in access

to sensing capabilities for researchers in various engineering and related fields that would have been unthinkable 20 years ago.

1.3 Multifunctional Materials and Flexible Electronics

Alongside MEMS, the field of multifunctional materials has also emerged as one with broad implications across multiple research disciplines. Multifunctional materials are material systems that have been designed for more than one functionality such as load support, sensing, actuation, and power harvesting. Such materials lend themselves to a vast range of applications: for example, Hou et al. [11] used carbon nanotube composites for strain sensing, Mishra et al. [12] proposed zinc oxide (ZnO) tetrapod networks for gas sensing, Persano et al. [13] proposed arrays of nanofibers for piezoelectric pressure sensing, and Wang et al. [14] proposed a magnetic mesoporous silica nanocomposite for Hg2+ detection. These are just some examples of recent advances in the field. The broad range of multifunctional materials and their many applications have been reported by numerous review articles [15], [16]. In the context of SHM, multifunctional materials have also been explored including self-sensing construction materials (e.g., self-sensing concretes) [17]–[19] and self-sensing coatings that are mechanically robust to harsh environments [20]. Multifunctional thin films have also been shown to be capable of serving as a sensing appliqué (or skin) that can provide spatial mappings of structural health based on repeated electrical probing (such as through electrical impedance tomography (EIT)) [17], [20]–[22]. Of the various multifunctional materials explored for SHM, the most promising have been composites consisting of a conductive filler dispersed in a polymer matrix [22], [23]. Polymer composite materials, multifunctional and otherwise, have been shown to be useful for conforming to structures and providing flexible sensors.

The flexibility of multifunctional thin films is critical to their applications for structural sensing technologies. Sensor flexibility is very important for practical considerations such as the need to conform to rough, curved, or irregular surfaces as might be present in tight spaces on steel structures, curved composites on airplane wings, curves on critical connections of various material types, and curved structures in the human body to name a few illustrative examples. Flexible sensors must be able to bend and potentially stretch with the structures on which they are sensing, otherwise they will not provide an accurate reading and may provide undesired local stiffness masking structural behavior. Furthermore, flexible sensors can be far more durable to impact and loading than sensors with rigid packaging. The benefits of flexible sensors have led researchers to build fully flexible electronics such as those with organic transistors [24], thin and wavy semiconductors [25], and other approaches.

While flexible electronics is an exciting research topic, rigid conventional ICs are cheaper, more prevalent, durable, and adhere to higher performance standards [26], [27]. This gap in capabilities necessitates integrating flexible film electronics with rigid electronics to currently achieve the benefits of flexible sensors with functionalities well-beyond those currently achievable with systems only based on flexible electronics. The creation of this gap between the promise of flexible sensors and the impact of flexible sensors when coupled with broadly available electronics is easy to understand in the context of MEMS systems. Dissimilar technologies are not often coupled due to the considerable challenges associated with designing and fabricating such systems.

Research teams have begun to explore the integration of multifunctional thin films with integrated circuitry on flexible substrates [25], [28]. A key element of integrating multifunctional thin films in a sensing system is the ability to control their deposited geometries on a substrate (flexible or rigid). Methods previously explored to pattern multifunctional thin films include inkjet

printing [29], imprint (or soft lithography) [30], nano-transfer printing [31], optical lithography [32], and direct laser writing [33], among others [34]–[38].

Specific to SHM, Glisic et al. [36] proposed the integration of strain sensing elements in large-area sensing sheets for SHM applications. Flexible large-area substrates were designed with thin film silicon electronics and dense arrays of traditional metal foil strain gages integrated. While this work illustrated the benefits of fully-integrated sensing systems on flexible substrates, it relied on commercial metal foil gages glued to the substrate as the strain sensing element. This missed the important capability of polymer-based thin film materials for distributed sensing in SHM and left out this broad class of materials in the framework for rigid-flexible circuit integration proposed by the researchers. The vast field of thin film flexible sensors offers compelling features and applications; hence bridging existing gaps between the optimization of such materials and their practical implementation in sensing systems is warranted.

1.4 CNT-Polymer Composite Materials

Progress in multifunctional materials can be considered in a variety of material platforms. One platform with recent importance in SHM is carbon nanotube (CNT) filler-based polymer composites. Since the discovery of the carbon nanotube (CNT) by Ijima et al. [39] and characterization of their physical and electrical properties, many researchers have sought methods to include CNTs in composite materials to alter the bulk mechanical and electrical properties of the composite. This was motivated by the compelling material properties of CNTs such as extremely high aspect ratios, high strength and stiffness, and semiconducting or metallic electrical properties [40]–[42]. Generally, in multifunctional materials and polymer composites, researchers have sought to optimize material fabrication parameters to enhance material sensing capabilities at bulk scale, as is apparent with those using CNT fillers [23], [24], [43]. Objectives have included

enhancing mechanical strength and stiffness [44], electrical properties [45], [46], and sensing response [22], [35], [47]. Various methods exist to include CNTs in a composite including layer-by-layer (LbL) deposition, mixing in epoxies, and spraying with polymer solutions, among others [23], [48], [49]. A vast range of end-use functionalities of CNTs in engineered systems has been proposed including, but not limited to, sensing, structural reinforcement, and electronics.

Early attempts at using these multifunctional materials for structural sensing focused on depositing them onto structural surfaces (e.g., as a coating) but precise control of their placement was not a primary consideration. For example, the initial sensing skin work by Hou et al. [21] adopted a strategy of coating entire structural surfaces with uniform, monolithic self-sensing multifunctional materials with electrical impedance tomography (EIT) used to create tomographic mappings of film conductivity. EIT is an inverse method that maps body conductivity based on boundary electrical measurement (voltage) for repeated cases of electrical stimulation (current) at the boundary. EIT for SHM was later advanced by Hallaji et al. [19] and Tallman and Wang [50], among others. The substantial number of electrodes associated with EIT is a challenge when applied outside the laboratory setting where electrode installation is expensive and prone to damage in harsh field conditions. Other researchers have optimized CNT materials as classical piezoresistive strain sensors functioning, to varying degrees, as distributed sensors [47], [51]–[53]. These studies illustrate the vast research performed for the development of CNT-based strain sensors, however much less work has been done to illustrate a practical means to achieving these benefits in a final designed system for SHM. To realize the benefits of multifunctional materials in SHM applications, there is a need to create both spatially placed films and fully integrated thin film systems where the multifunctional material is combined with electronics to provide a more functional interface for sensor readings.

1.5 Applications of Sensing Strain Including Structural Health Monitoring

With the proliferation of sensors and technologies such as those utilized by the MEMS field, many efforts have been made to collect data on mechanical responses to better monitor structural systems. In infrastructure, structural health monitoring (SHM) has emerged as an approach for structural owners and operators to assess the health and performance of their assets using quantitative data derived from sensors [54]. A variety of new sensor types have been adopted in SHM in recent years: adopted sensors include MEMS sensors such as piezoresistive accelerometers by Lynch et al. implemented with wireless sensing units for low-cost sensing on a laboratory test system [55], fiber optic sensors such as those used by Glisic and Inaudi to detect cracks in bridges in laboratory tests and an on-site demonstration [56], and piezoelectric sensors and actuators as used by Ihn and Chang for sensing crack growth in metallic structures [57], to name a few.

SHM sensors, in similar fashion to the MEMS transducers previously discussed, must be designed as a complete system considering not only the appropriateness of a given sensor for a structure, but also the readout electronics, data acquisition system, and signal processing needed to transform mechanical excitations into engineering insights and actionable information (Figure 1-1). Readout electronics are increasingly accessible through lower cost and more powerful electronics such as microprocessors that have advanced according to Moore’s law over recent decades. Wireless communications and networks have been advanced by researchers and installed in true SHM applications for cheaper and easier sensor deployments [58], [59]. Signal processing has advanced through research achievements in machine learning applied to sensing structural systems [60]. Collection, archiving, and processing of vast amounts of data have also become more

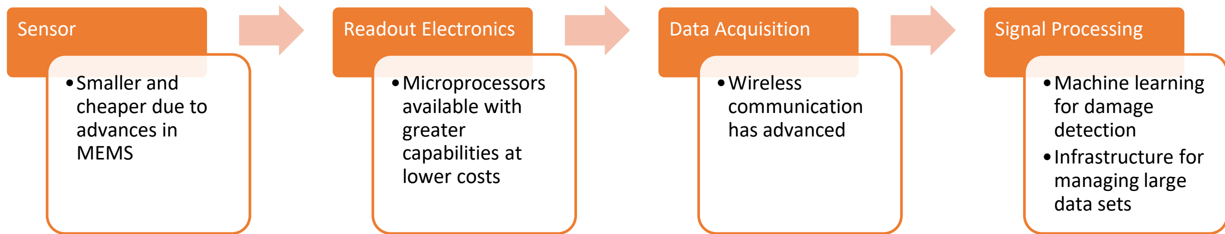

Figure 1-1. Enabling technologies for structural health monitoring.

viable through growing use of cloud computing and storage. These complementary technologies have improved the practicality of collecting actionable information on the functional state of structural systems and aiding decision makers to better manage their structures.

The potential of robust and conformable flexible electronics holds promise for many strain sensing applications both inside and outside the domain of built infrastructure systems. The SHM systems deployed to date in operational structures include measures of structural strain. Strain is an important structural response because if a material constitutive law is assumed, a state of stress can be assessed. This is highly convenient because the safe limit state of a structure is based often on stress levels in structural components [61].

One SHM application outside of civil structures area that will be explored in this thesis is the use of thin film strain sensors in a medical domain; specifically monitoring orthopedic systems (such as implants) which are essentially a structure. Such applications require not only conformable sensors, but ones that are biocompatible and that have wireless interfaces. Past efforts relevant to *in vivo*, strain sensing include a comprehensive work more than fifteen years ago by Burny et al. [37] providing an early attempt at a wireless system capable of strain monitoring in orthopedic implants and highlighting the design demands of the problem. Korduba et al. [38] presents the current state of radio frequency identification (RFID) based wireless sensors in orthopedic implants as feasible but requiring detailed design consideration in the communication

and robustness of these systems. Numerous more specific sensor proposals have also been proposed. For example, Greve et al. [62] put forth a wireless surface acoustic wave strain sensor in an intramedullary nail for monitoring fracture healing. Umbrecht et. al. [63] proposed a wireless implantable strain sensor based on a microfluidic reservoir sensor and ultrasonic wireless interrogation of the sensor. Melik et al. [64] proposed an implantable strain sensor based on split ring resonators using telemetric readout. Separately, Jia et al. [65] proposed an inductor (L)-capacitor (C), or LC, sensor on polyimide for structural health monitoring. However, use of sensors in implants remains sparse and needs remain for simple, viable sensing systems in vivo for applications such as osseointegrated prosthetics.

The various new tools available to researchers and numerous examples of deployed SHM systems by researchers necessitates a discussion on the fundamental state of the field and needs for achieving the goal of SHM. The field of SHM has three fundamental aspirations that fully characterize the damage state of a structure: namely the identification of the severity, location, and failure mode of significant damage a structure has incurred. SHM studies are almost always some subset of this broad challenge. Much of the field has focused on using networks of sensors to characterize the global response of a structural system to then infer damage based on detected changes in the global response [60]. However, this often fails to accurately identify location or damage type.

While inferred damage detection may have its place in certain structural systems, the potential for missing local damage at critical points in structures leaves many systems vulnerable to false negatives (situations where damage is present, but the system is identified as functioning normally) and false positives (which erode user confidence in SHM). The nature of many structural systems such as steel frames and composite materials results in damage that will manifest in

concentrated locations far earlier than it will be visible in the global response of the system. This then creates a situation where the cardinal sin of health monitoring, an indication of safety that is in error, placing stakeholders in danger, can result from a lack of local information at critical points. The sensor system design challenge that follows is one of the necessity for sensor density. If we are afraid to limit our sensor network to widely spaced sensor locations for fear of missing local damage, then how local is local and is it realistic to use the necessary number of sensors for local to be defined at a safe level? This is where we reach a second limitation of our current approach to SHM in that the use of point sensors is inadequate. To collect comprehensive local damage information would require a density of sensors that would not scale in a manner practical for SHM applications. Trying to densely place strain sensors leads to two practical limitations: namely, (1) it is unrealistic to instrument and wire the required number of sensors; and (2) this approach will indiscriminately create huge amounts of data that will require significant effort to save and process and will likely obscure damage information without substantial processing. This requires some manner of distributed sensing, which is capable of sensing over areas on structures instead of the current limitation to sensing at a point.

The challenge of SHM is one that must be resolved by observing the holistic behavior of the structural system. It should aim to achieve direct damage detection with precision and efficiency when it can to reduce dependence on inverse methods that have yet to prove sufficiently general and robust. In short, this is simply the obvious point that sensing approaches must be tailored to the functionality and failure mode of the structural system being monitored. However, when fully unpackaged, it illustrates the need for designing a limited number of distributed sensors to have the spatial capability to measure (not just infer) local damage but the efficiency of a lower number of overall sensors for ease of instrumentation, data storage, and processing. Moreover, if

these distributed sensors are designed geometrically for critical components on the structure, such as connections in steel frames, they can be assured to have the resolution necessary for the structural system and can be designed to isolate damage location and failure mode. These needs require geometrically patterned, distributed sensors that can sense damage directly over large areas to avoid the blind spots that are unavoidable in indirect or point sensing-based approaches to SHM.

1.6 Research Objectives and Dissertation Outline

The above discussion illustrates the need for creating flexible thin film and polymer composite materials for strain sensing, enabling these materials through integration with conventional ICs, and utilizing these materials through intelligent, system-level design for SHM. With these motivating research needs, this thesis strives toward the following primary objectives:

- design and fabricate flexible TF components for conformable electronics and strain sensing;
- enable a broad class of polymer composite and multifunctional materials through processing and system design integrating dissimilar electrical components;
- improve structural sensing technologies through novel system design as demonstrated with realistic experimental testing.

These objectives are pursued in the following four chapters with three types of efforts described as follows. The work and intellectual contribution are concluded in a final chapter.

1.6.1 Design and Fabrication of Flexible RLC Primitives

In Chapter 2, processes are described for creating thin film (TF) analog circuit building blocks with the fabrication of resistors, capacitors, and inductors. These fundamental electrical

components are fabricated in a thin film (TF), flexible form for utilization as sensors and circuit components in sensing systems. This chapter also serves as a high-level overview for much of the processing contained throughout the thesis and a fundamental toolkit for the fabrication of TF strain sensors. The chapter begins with processes for patterning, etching, and electroplating metal films and an illustration of these processes in the fabrication of a thin film inductor. Next, processes are described for processing polyimide as a broadly useful polymer substrate material and illustrated in the fabrication of TF, parallel-plate capacitors. Processing of polyimide substrate systems is then described by creating polymer nanocomposite thin films based on layer-by-layer fabrication methodologies, which enables the creation a vast set of materials. Resistors are fabricated with a carbon nanotube-polymer composite material using the layer-by-layer process. Resistors are patterned to control bulk resistance and gage factor of resistors is observed by varying patterned device dimensions. This completes the basic set of building blocks for designing flexible thin film analog circuit sensors. Finally, methods are described for integrating dissimilar system components and lowering the cost of SHM TF sensor development. This chapter will have redundancies with later sensor system fabrication chapters but is meant to provide an overview of capabilities and design concepts and not the detailed fabrication descriptions of specific TF sensing systems as presented in later chapters.

1.6.2 Theory of Fabrication

In Chapters 3 through 5, the progression from fundamental building blocks to a complete, functional system for strain sensing is based on a comprehensive theory that accounts for the capabilities and limitations of described technologies for fabrication and use. The fabrication is, in appropriate applications, designed to incorporate flexible thin film materials and conventional IC

components for reasons described above. This is achieved by starting the process with a robust polymer substrate and metal electrode layers. Next, novel material processing is completed. Finally, off-the-shelf components and ICs are bonded to the system where appropriate. This is intellectually important as it sets a broad process for creating sensing systems that incorporate these materials of varying class and capability. More specifically, the proposed processing steps present a clear framework for advancing the vast body of research in polymer composite sensors to sensing systems ready to achieve their respective intended impact in practice. Furthermore, the proposed metal stacks are designed to be robust to many processes and are broadly valuable for many flexible materials.

1.6.3 Implementation of Thin Film Systems for a Variety of Strain Sensing Applications

The power of the processing methods introduced is illustrated through the design and fabrication of three sensing systems embodying important concepts for obtaining information on the functionality of structural systems.

First, in Chapter 3 a sensor is designed that integrates carbon nanotube (CNT) thin film sensors into a bridge circuit with an instrumentation amplifier. The circuit is designed for two objectives: (1) to illustrate the use of a polymer composite for distributed strain sensing in a SHM setting and (2) to illustrate the design and fabrication of an integrated system incorporating flexible polymer components and rigid conventional ICs. This is intellectually important for multifunctional materials and sensor design as it illustrates the previously noted fabrication methodology for realizing the benefits of flexible and conventional IC components in the same system, addresses many of the toughest fabrication challenges to the broad class of multifunctional materials in this process, and provides the basis for integrating rigid and flexible components in the same system. It is intellectually important for health monitoring as it shows a full field

deployment of multifunctional materials, which many have researched at the material level with an eye on potential SHM applications. It further illustrates the basis for distributed sensing and novel sensor fabrication for advanced damage detection sensors capable of sensing failure modes.

Second, in Chapter 4 a sensor system comprised of an array of CNT composite-based resistors is fabricated for spatial damage detection to improve on current EIT methods for sensing strain over a spatial area. This is intellectually important as it improves a sensing system and algorithm that provides many of the benefits of EIT without convergence problems that are often a critical limitation in EIT methods. Additionally, the approach provides a problem that is mathematically more tractable and as such can handle large changes in resistance within the sensing materials as is valuable when monitoring for SHM damage. As in previous examples, this is achieved by taking a system-level view of the design processing that factors in various fabrication capabilities in the context of system use and functionality. The algorithm for estimating array element resistance is illustrated to validate functionality and show unique algorithm capabilities. The fabricated sensor array is then utilized with the algorithm for spatial strain sensing as desired in SHM applications.

Third, in Chapter 5 flexible sensing system design approaches are considered by creating a wireless, implantable strain sensor for embedded sensing based on thin film inductor and capacitor components. The sensing system is built with two inductor-capacitor circuits with inductors for wireless interrogation, capacitors to set resonant frequencies and sense strain, and a fuse element in one of the LC circuits designed to provide threshold strain sensing. This is intellectually important as it presents a wireless implantable strain sensor that is robust and adaptable to installations in various environments, surpassing current limitations to wireless implantable strain sensing. The fused element in the system is intellectually valuable as it provides a SHM sensing

methodology that is easily read and interpreted in a manner that can be executed for a vast set of SHM environments and measurands. The fuse element is developed experimentally by testing various designs and fabrication methods of titanium thin films and observing the predictability and repeatability of their failure behavior. Multiple completed thin film sensing systems are tested, and the results are discussed in the context of future SHM utilization.

1.6.4 Key Intellectual Contributions of This Work

The previous discussion illustrates the need for direct measurement of strain and improved interrogation of strain sensors to prove a solution that can be utilized over a spatial area for monitoring structural integrity. Multifunctional and other thin film materials have shown great promise for such sensing. However, these lack the system fabrication maturity for deploying and interrogating such systems in realistic application environments. With this motivation, the fundamental contribution of this thesis is a broad theory of fabrication for flexible thin film systems in structural health monitoring applications.

The theory of fabrication herein is intended to produce SHM solutions that are low cost, large area, conformable, wireless, and analog. Chapter 2 provides the first significant contribution to this overarching effort in an optimized approach to patterning fibrous polymer-nanocomposite materials using optical lithography tools that are widely available in MEMS and IC fabrication environments. This provides a broadly applicable patterning technology to this non-conventional material. Additionally, the design of resistive and strain sensing components is put forth using these methods and the nanocomposite material.

Next, Chapter 3 provides a key intellectual contribution in detailing a fabrication process that broadly enables the use of thin film sensors alongside dissimilar materials for achieving sensing in SHM applications. This process includes a detailed design of a robust metal stack on a polyimide

substrate to provide a base layer for a vast set of film technologies and uses. Additionally, methods for compartmentalizing dissimilar materials in the staging of fabrication and planar sensor layout are presented as broadly useful for such thin film systems. Finally, an CNT-polymer nanocomposite sensing material is integrated with on-film dissimilar components and tested in a realistic SHM setting. This is the first such test (to the author's knowledge) that advances such materials from their current use in laboratory settings to a form that can be installed, interrogated, and maintained in a true SHM application. Chapter 4 makes an important intellectual contribution in detailing an array-based alternative to the fabrication and inverse algorithmic readout of a polymer nanocomposite sensing skin spatial strain sensor. This is highly valuable as it presents a fundamentally different approach that enables more direct mathematical processing of signals from boundary nodes of a sensor network that alleviates important uncertainties in current EIT methods. The proposed algorithm and thin film system are constructed and tested in an application that validates this approach to strain sensing.

Finally, Chapter 5 provides multiple important intellectual contributions to the advancement of thin film sensors for SHM. First, a novel design of a thin film inductor-capacitor sensors is fabricated and illustrated as a wireless readout technology with potential use for a vast range of thin film sensors. Second, a sensor fabrication theory of utilizing metal films as "fused sensors" for strain sensing is presented. This creates a sensing approach that can be readily interrogated and interpreted wirelessly, providing a clear decision metric for SHM. Additionally, the thin film form of this fused-sensing approach opens the door for use of fuses of many different material types and responsive to many different stimuli by simply replacing this modular element in the wireless strain sensing system design presented.

CHAPTER 2.

FABRICATION OF RLC PRIMITIVES AND METHODS FOR SYSTEM INTEGRATION

2.1 Introduction

In this chapter, fabrication processes and methodologies are described to provide the basis for the remainder of the thesis and similar future work. The purpose of the chapter is twofold. First, processes descriptions in this chapter provide the basis for sensor and system designs in the following three application chapters. This set of capabilities is laid out as the fabrication of fundamental electrical building blocks in thin film inductors, capacitors, and resistors. Additionally, a description of methodologies for integrating dissimilar components in thin film systems is provided. Second, this illustrates for researchers a core set of technologies based on thin film and cleanroom fabrication for building sensors in numerous applications. Processes described range from the highly unique to the layout of well-trodden, fundamental processes for the basis of constructing thin film sensors and the detail and specificity of process descriptions will vary accordingly. The chapter begins with a few fundamental processes for fabricating metals layers in thin film systems. This section concludes with the fabrication of a thin film inductor with the processes described. Next, best practices are discussed for utilizing polyimide as a robust, flexible substrate for thin film technologies. The section concludes with the utilization of described technologies for the fabrication of thin film capacitors. Following this, methods for multifunctional

thin film fabrication are described and utilized in the design of strain sensitive resistors. Finally, methods for rapid prototyping, system integration, and characterization are discussed. The section is written as a high-level description of fundamental capabilities for the vast range of disciplines that utilize flexible or conformable thin film sensing systems and as such does not have the depth or detail provided in later chapters that is likely desired by those experienced in micro and nanofabrication.

2.2 Fabrication of CNT-Polymer Thin Film Composites

Polymer composites and other organic thin film materials comprise an important class of engineering materials for the future of sensors and devices. In this section, fabrication CNT-polymer thin film composites are details as an example class of such materials that unlock many of the material design capabilities that make this space so compelling for utilization in engineered thin film systems. While this is a small class out of the vast range of existing TF polymer composites, it exemplifies opportunities and challenges that apply when attempting to utilize a vast range of thin film materials.

2.2.1 Layer-By-Layer Fabrication Method

In this work, the primary fabrication methodology for thin film sensing nanomaterial design is the layer-by-layer fabrication process. This process has been widely utilized in the past for a variety of electronic [66], [67], mechanical [68], [69], and sensing applications [70]–[72]. Our approach to layer-by-layer fabrication is based on methods developed by Loh et. al. [70].

Process:

1. Prepare solutions for processing

- PSS Preparation: Weigh one weight percent PSS into deionized water. Mix with bath sonication until PSS is dissolved.
- PSS-CNT solution preparation: Weigh and mix one mg/mL CNTs into PSS solution in 20 mL vials. Bath sonicate the vials (135W, 42 kHz, 180 minutes). Tip sonicate the vials (3.178 mm tip, 150 W, 22 kHz, 30 minutes) with pulses of 5 seconds on and 5 seconds off to prevent overheating.
- PVA Preparation: Weigh one weight percent PVA into deionized water in a 600 mL jar. Heat the solution to 90°C until the PVA dissolves and the solution becomes clear. After cooling, add hydrochloric acid incrementally until the pH of the solution becomes 1.7.

2. Prepare substrate surface for thin film adhesion
   - If using glass slides: Soak in piranha solution (hydrogen peroxide and sulfuric acid – caution: highly volatile) for 20 minutes. Rinse and dry.
   - If using polyimide: Immerse in poly-L-lysine for 5 minutes. Rinse and dry.

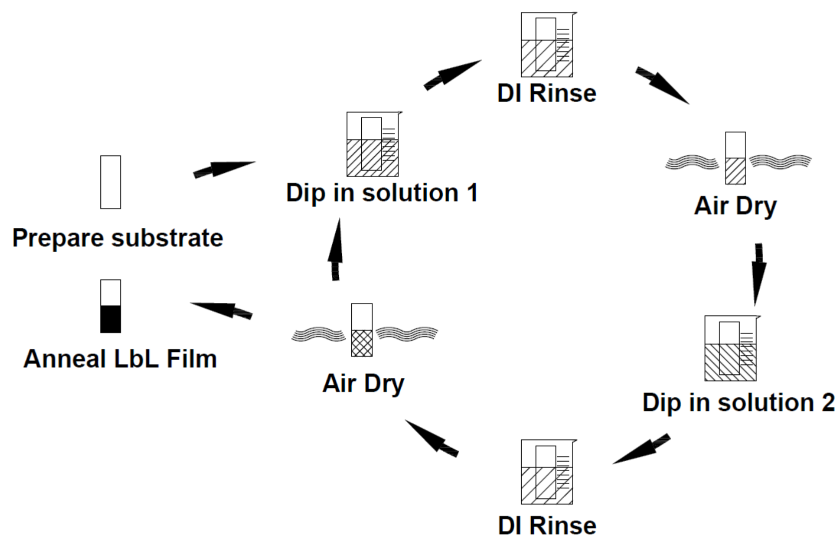

Figure 2-1. LbL thin film fabrication process.

3. Sequentially build film using hand dipping or automated process as shown in Figure 2-1
    - First monolayer: Dip in CNT-PSS solution for 2 minutes. Rinse thoroughly in deionized water. Dry thoroughly.
    - Second monolayer: Dip in PVA solution for 2 minutes. Rinse thoroughly in deionized water. Dry thoroughly.
    - Following layers: The first two monolayers combined to comprise one bilayer of thin film material. This sequence is repeated until the desired number of bilayers have been deposited.
4. Anneal LbL film
    - Anneal films in convection oven at 250 C. Ramp at 5 C/minute from room temperature then hold at 250 C for 20 minutes. Allow for gradual cooling.
5. Instrument annealed films
    - Release films from rigid backing to free flexible substrate. Connect wires or conductive copper tape to films using silver paste or conductive epoxy. Encase with silicone to provide a protective layer and enhance sensor robustness.

2.2.2 Lithographic Patterning of CNT-Polymer Composites

This section describes patterning of layer-by-layer polymer composites described in the previous section using optical lithography in a similar manner to that described for metals in Section 2.2.1. This allows for patterning of various polymer composite materials with methods generally available in cleanroom environments. Although the ease and ability to pattern LbL films is dependent on the specific material being patterned, this section provides a general overview of available processes and best practices for handling flexible substrates through such fabrication. An illustration of the patterning process can be seen below in Figure 2-2.

Process:

1. Bond polyimide film to rigid wafer for processing

    - For low temperature processing: Bond polyimide to a rigid silicon wafer using beeswax. Heat the silicon to 130°C and spread beeswax on the silicon wafer (wax will melt as it contacts wafer). Lay polyimide over wax, provide even, compressive force, and cool while compressed. Polyimide substrates should be detached and re-bonded in this manner anytime the substrates have been immersed in solution for best processing results.
    - For high temperature processing: Bond polyimide to rigid silicon wafer or glass substrate using Kapton tape at the edges of the substrate.

2. Spin, expose, and develop photoresist for masked patterning of LbL film

    - Spin photoresist on polyimide film: Clean film prior to process with an acetone rinse followed by an isopropanol rinse. Spin photoresist using spinner tool as generally available in a cleanroom environment. Soft bake the photoresist according to product specifications for the resist used.
    - Expose photoresist: Calculate exposure time based on the photoresist used, patterned area, and lamp on the exposure tool used to align and provide ultraviolet

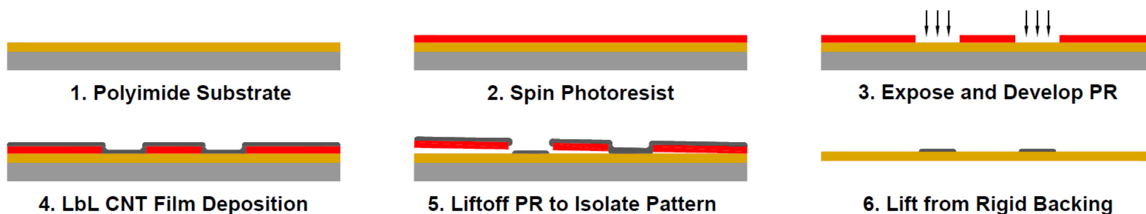

Figure 2-2. Fabrication flow for patterning fibrous LbL films.

light. Many photoresists need a post-exposure bake after exposure and before the photoresist is developed.

- Develop photoresist: Use a bath of developer or developer tool to remove the exposed photoresist. The development time is set based on the thickness of the photoresist and area exposed.
- Notes on thick and thin photoresists: In this dissertation optical lithography processes generally need either a relatively thin or thick photoresist layer depending on the thickness and mechanical strength of the material deposited. An example of each is provided below.
    i. Thin photoresist example: Thin resist with a target thickness of three microns is spun at 3,000 rpm and soft baked for 90 seconds at 115°C. The resist is then exposed for 10 seconds, as necessitated by the patterned area, in a mask aligner exposure tool and a post-exposure bake is performed for 90 seconds at 115°C soon after exposure. The photoresist is developed for 30 seconds in developer solution.
    ii. Thick photoresist example: Thick resist with a target thickness of seven microns is spun at 2,000 rpms and soft baked for 15 minutes at 80°C. The resist is exposed for 30 seconds in a mask aligner exposure tool. The exposure may need to be broken into two or three separate exposures over the same area to avoid burning the photoresist as is often possible in aligner tools. The photoresist is then allowed to outgas for an hour prior to post-exposure bake. The photoresist is posed-exposure baked for 90 seconds at

115°C. The resist is then developed using two rinses held for 60 seconds each in developer solution.

3. Deposit LbL film
   - Fabricate layer-by-layer film according to the process described in Section 4.2.1.
4. Liftoff LbL film
   - Soak completed film in acetone to dissolve photoresist and liftoff unwanted areas of polymer nanocomposite film. Bath sonication is necessary to facilitate film tearing at the edges of the patterned area. Generally, films are allowed to soak for 10 minutes initially then sonicated for 30 second time periods every 5-10 minutes to enhance film tearing.
5. Continue processing with patterned LbL film
   - Remaining processing is then conducted including annealing, additional cleanroom fabrication for other system components, or instrumentation.
   - Silicone to provide a protective layer and enhance sensor robustness.

2.2.3 Illustration: Strain Sensitive Thin Film Resistors of Various Widths

The broad use of polymer composite and multifunctional materials described in Chapter 1 illustrate numerous potential applications for such thin film materials. Here, a method for patterning such films is developed using tools and materials that are widely available in cleanroom fabrication environments. The processes for this and impact on resistive and sensing parameters for a specific polymer composite film are described and explored. The development of patterned polymer nanocomposite films is achieved here using the layer-by-layer fabrication process described in Section 2.4.1 and patterning process in Section 2.4.2.

PI-2525 polyimide and VM-651 polyimide adhesion promoter were obtained from HD Microsystems. Poly(vinyl alcohol) (PVA) and poly(sodium 4-styrenesulfonate) (PSS) were obtained from Sigma-Aldrich. HiPCO Single walled carbon nanotubes (SWNT) were obtained from Unidym, Inc. SPR 220-3.0 photoresist from Rohm and Haas Co. and AZ 726 developer from Clariant Corporation were used as supplied by the Lurie Nanofabrication Facility at the University of Michigan. Silver paste and copper tape were obtained from Ted Pella, Inc. All solutions were made using 18 MΩ cm deionized (DI) water.

Fabrication is completed by layering thin films on a glass slide followed by detachment of the fabricated materials from the slide to yield a free-standing thin film. This process begins by spin coating adhesion promoter and then polyimide on a cleaned glass slide. The polyimide is spun at 2000 rpm resulting in a thickness of around 12 microns for each polyimide layer. Four polyimide layers are deposited to produce a polyimide film with a thickness of around 48 microns (Figure 2-3a). The polyimide is cured on a hot plate by ramping the temperature from 25°C to 300°C at 5°C/minute and then holding the temperature at 300 °C for one hour. Next, photoresist (PR) is patterned on the substrate using optical lithography. This begins with drying and priming the polyimide for PR using an image reversal oven to apply a hexamethyldisilazane (HMDS) layer.

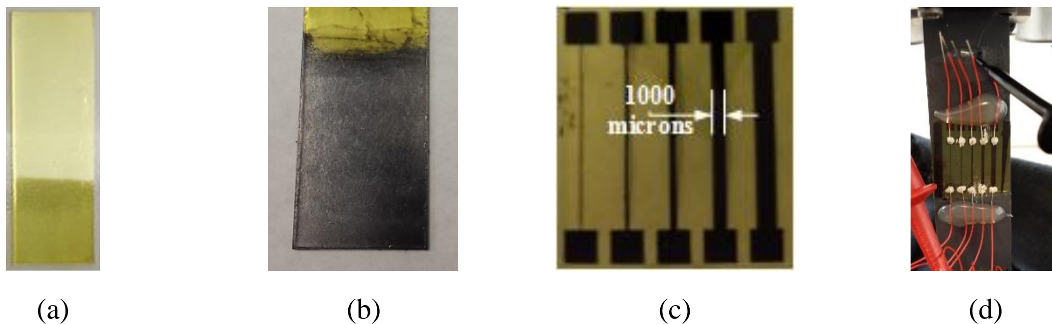

Figure 2-3. Fabrication stages for small-scale sensing skins: (a) polyimide on glass slide; (b) CNT thin film covering PR and polyimide on slide; (c) patterned CNT sensing skin with sensing elements of thickness 100, 250, 500, 1000, and 1500 microns from left to right as fabricated and tested; (d) polyimide substrate epoxy bonded to PVC coupon with silver colloidal paste used to attach electrodes.

Next, a PR layer is spun over the sample at 2000 rpm and soft baked for 90 seconds at 115°C. The PR is then exposed under a mask. A post exposure bake is completed for 90 seconds at 115°C and then the PR is developed with AZ 726 developer for two rounds lasting 60 seconds each.

After PR is patterned on the polyimide substrate, the process transitions to the fabrication of the CNT thin film. The polyimide that is not covered with PR is treated with poly-l-lysine by soaking for five minutes to promote surface adhesion with the polyelectrolytes that will comprise the nanocomposite film. The nanocomposite film is then deposited over the polyimide and PR by the LbL directed-assembly method (Figure 2-3b). When this is complete, the CNT composite film is lifted off the PR covered areas by placing the samples in an acetone bath for 10 minutes and then placing this bath in a bath sonicator to apply surface energy to aid in tearing of the CNT composite film. During bath sonication, energy is applied for 30 seconds and then the samples sit still for one minute. This process continues for approximately 10 minutes until the PR film has fully lifted from the surface.

The specimens fabricated by robotic LbL assembly on glass slides (termed herein as small-scale sensing skins) are patterned as 5 parallel strips roughly 2 cm long with varying thicknesses: 100, 250, 500, 1000 and 1500 microns (Figure 2-3c). At the end of the strips are square pads where silver past can be applied to create a wired electrical connection to a data acquisition system that is used to measure film resistances.

The nanocomposite sensing skins are fabricated with an established layer-by-layer fabrication process. This process utilizes oppositely charged polyelectrolyte solutions to attract thin layers of each solution to the substrate surface. The substrate is sequentially dipped in two solutions of opposite charge to build up a well-controlled, uniform thin film. The positively charged solution used here is 1.0 wt. % PVA and the negatively charged solution is 1.0 wt. % PSS.

Single wall carbon nanotubes (0.1 wt. %) are non-covalently dispersed in the PSS solution using deep tip (3.178 mm tip, 150 W, 22 kHz, 90 minutes) and bath (135W, 42 kHz, 360 minutes) sonication. The deposition sequence for one layer of one polyelectrolyte solution consists of dipping in the solution (PSS or PVA) for four minutes followed by submersing in DI water twice for two minutes each. These steps are then followed by low pressure air drying for seven minutes and high-pressure air drying for one minute. This results in the application of a single monolayer (PSS or PVA). Once this process is completed, the process is repeated using the oppositely charged polyelectrolyte solution to yield a single thin film bi-layer. The bilinear process is repeated until a film with a thickness of 50 bilayers is fabricated. The fabrication process is automated with a LbL robotic fabrication setup. Further explanation of the layer-by-layer process is available in previous publications [8]. Once the nanocomposite film is deposited and patterned by the lift-off process, the film is annealed for 20 minutes at 180°C on a hot plate. Finally, the polyimide substrate is removed from the substrate by etching away a layer of glass using buffered hydrofluoric acid.

Fabricated small-scale sensing skins are epoxy bonded to PVC composite specimens for uniaxial tensile testing. This requires the addition of electrodes to the patterned sensing skins. Colloidal silver paste is used to glue copper wires to the film surface that serve as electrodes. As previously mentioned, bond pads are designated in the film design to allow for increased area over which colloidal paste can be applied. A digital multimeter is used to probe the attached electrodes and to determine film resistance once electrodes are dry. The multimeter is used to measure resistance and these values are collected throughout uniaxial cyclic testing. A picture of the instrumented PVC coupon is shown in Figure 2-3d.

The mechanical-electrical response of the sensing skins is determined using uniaxial cyclic testing on a hydraulic load frame. In this process the films are loaded for three cycles of tension-

compression. The strain in the structural member is also monitored using a traditional 120Ω metal foil strain gage opposite the patterned thin film sensor. The ambient behavior of the small-scale sensing skins on the structural members is observed for five minutes prior to each test. This allows for the observation of a drift that is commonly displayed by this type of sensing film. The specimen is then loaded at a rate of 0.5 mm/min and strain data is collected throughout the loading at a 1 Hz sample rate.

A macroscopic view of the patterned sensing elements is presented in Figure 2-3c. To see more clearly the quality of the patterned films, the films are imaged under a traditional optical microscope; microscope images (20 times magnification) of the edges of the nanocomposite films can be seen in Figure 2-4. All sensor geometries attempted were patterned successfully using standard optical lithography processes. There was no noticeable deterioration of pattern quality with decreasing feature size, indicating that the lower limit on feature sizes was near that of conventional lithography materials (i.e., approximately 2 microns). There was difficulty at times in achieving nanocomposite film tearing during lift-off resulting in an incomplete lift-off process but when lift-off is achieved, film geometries were defect free.

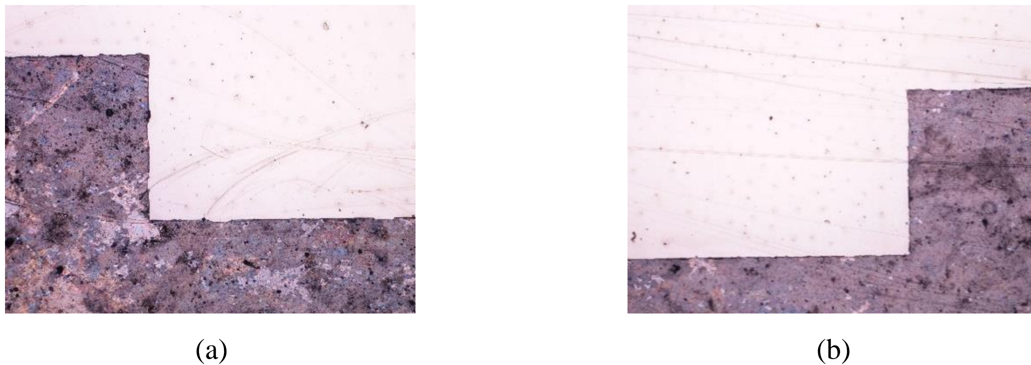

(a) (b)

Figure 2-4. Images of patterned sensors magnified at 20x showing some limited roughness along patterned film edges.

The resistance of each instrumented small-scale sensing skin was observed for five minutes prior to cyclic loading of the PVC bar. This observation displayed a rapid exponential signal decay that is commonly observed in such sensing skins [8]. The results for each sensor under cyclic loading can be seen in Figure 2-5. Here it is clear that each sensor was effective in tracking the strain of the specimen (note that Figure 2-5f is the measured strain using the metal foil gage). It

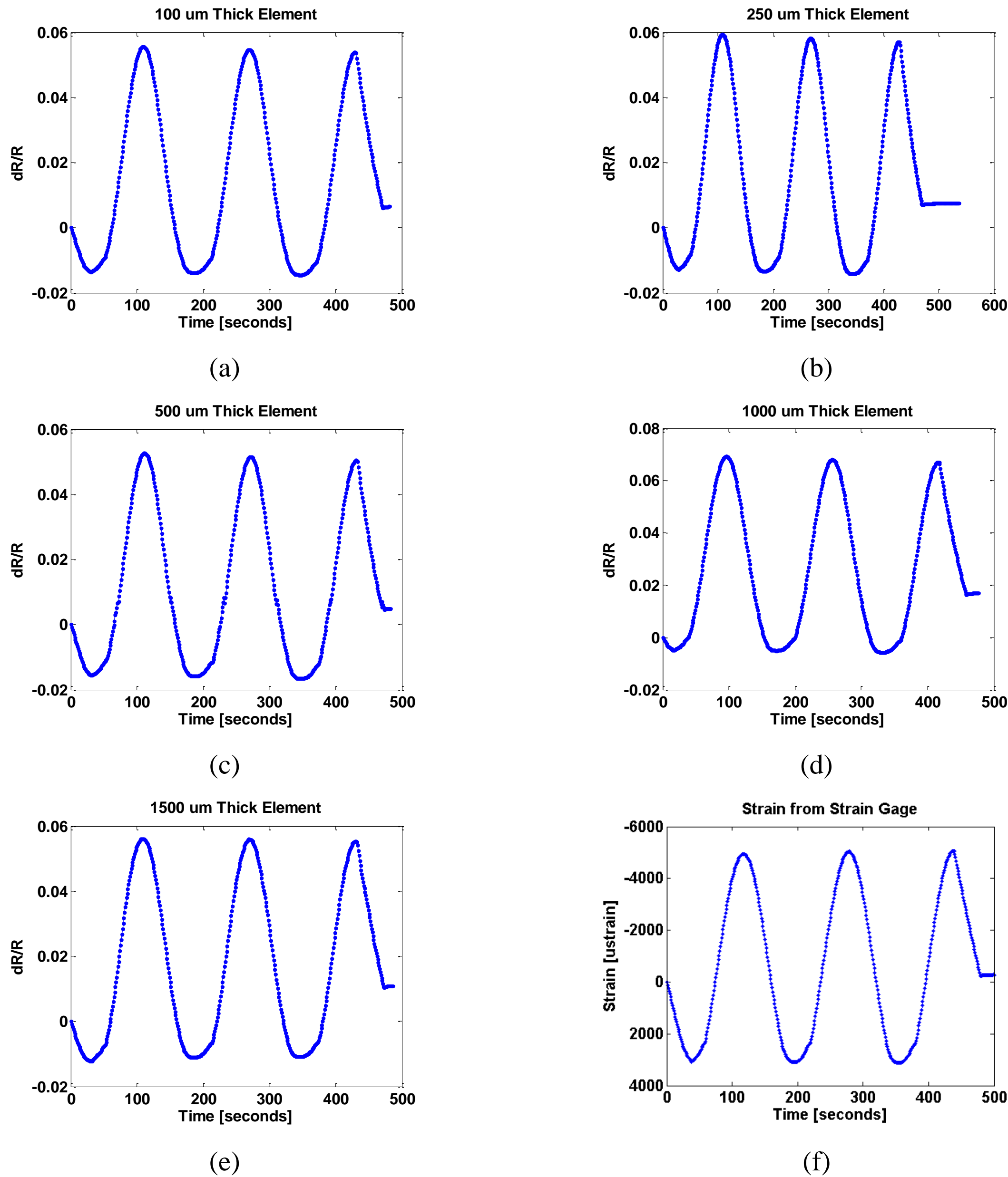

Figure 2-5. Change in resistance under cyclic loading for sensing elements of thickness: (a) 10 microns; (b) 250 microns; (c) 500 microns; (d) 1000 microns; (e) 1500 microns; (f) measured specimen strain using a tradition strain gage.

can further be observed that all sensors have similar signals with limited noise and fairy uniform sensitivities. The initial bulk resistance, sheet resistance, and gage factors of the five sensors of varying thickness can be seen in Figure 2-6. The sensing elements of larger widths are more conductive as is expected for these nanocomposite films (Figure 2-6a). The results also indicate a uniform gage factor across all sensor geometries despite the significant variance in sensor thicknesses (Figure 2-6b).

Nanocomposite sensing skins are patterned and tested for mechanical-electrical response. The sensor was fabricated on a flexible polyimide substrate using conventional optical lithography tools then epoxied to a PVC bar for testing. All geometries attempted were successfully patterned suggesting a limiting feature size near that of conventional lithography materials (2 um). Five small-scale sensing skin elements of varying width displayed similar sheet resistances and gage factors when instrumented and tested in uniaxial tension. The uniformity of gage factor with varying geometry was unexpected when considering the wide range of sensor geometries tested. The malleability of the patterning and fabrication processes utilized provides the platform for the

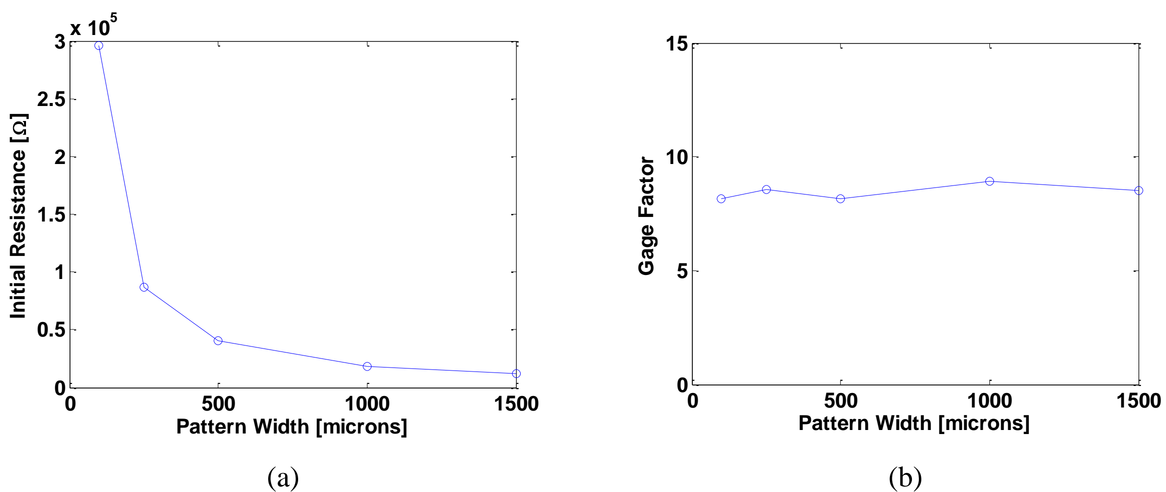

Figure 2-6. Electrical properties of sensing elements: (a) Initial resistance; (b) gage factor.

development of component-specific structural sensors for components of a vast range of structural systems.

2.3 Utilization of Metals for Thin Film Systems

Metals are a fundamental class of electrical material and important to the design of many sensing systems. As such, technologies have long existed for depositing, patterning, and removing metal layers in thin film systems. Basic capabilities that have long been established are briefly discussed here due to their importance in system design and construction. A process for inductor fabrication is described utilizing the processes described in this section.

2.3.1 Metal Patterning Using Optical Lithography

Metal patterning with optical lithography is a basic process that provides the foundation for then functionality of most electrical thin film systems [73]. Metals are conventional optical lithography materials and can be patterned in a similar manner to the lithography processes described in Section 2.2.2. Metals such as chromium, titanium, gold, silver, copper, and platinum can be patterned in this manner according to design needs.

2.3.2 Etching of Metal Layers

The removal of metal materials is important in addition to the deposition and patterning of metal materials. Metals can be removed using chemical etches by placing metal thin films in solutions in which the metal dissolves. This removal can be masked with a thin layer of photoresist to limit the areas that are etched. Undercut of the photoresist is possible so etches need to be timed to avoid this. The time required for an etch can depend on the metal, etchant, temperature and agitation of the solution during the etch.

2.3.3 Electroplating Gold and Copper for Metal Layers

Metals can be electroplated to provide thicker metal layers than can be deposited using methods such as physical vapor deposition or chemical vapor deposition. Electroplating involves depositing a seed layer thin film, immersing this in an ionic electroplating solution, attaching a power supply to the seed layer and a plate of the deposited metal, and finally building up a film by applying a potential between the attached metals. Electroplating can be patterned by patterning a seed layer then plating over the entire patterned area. Patterning is also possible by starting with a seed layer covering the entire substrate, covering this seed layer with photoresist so that material only accumulates in the metals areas not covered by photoresist, then removing the photoresist and etching a layer of metal thick enough to remove all metal from areas with only the seed layer. Stresses and thickness uniformity can be challenges in electroplating.

2.3.4 Illustration: Fabrication of Thin Film Inductors

The above processes are utilized to form thin film inductors. Inductors are designed using a square coil inductor layout. This was selected to maximize inductance over a planar area. Generally, a high quality factor, Q, as defined by the equation below is desired from inductors. This can clearly be achieved by maximizing L and minimizing R. The inductance was maximized through geometric design. To maximize inductance, the inductors are designed with as many turns as possible, a small space between traces, and large inner and outer diameters while maximizing the number of turns. However, the inductor has its own internal resistance, R, which is generally a small quantity. The inductor is fabricated by electroplating gold to allow for a thick gold layer, which increases the inductance, decreases the resistance, and thus increases the quality factor.

$$Q = \frac{\omega L}{R} \tag{2.1}$$

The process begins with a polyimide substrate bonded to a supporting silicon wafer by heating wax until melted on the wafer then placing a polyimide substrate and holding under uniform pressure until cooled. A seed layer of gold is then deposited using physical vapor deposition and patterned with optical lithography as described in Section 2.2.1. This is then electroplated as described in Section 2.2.3 to create a much thicker gold inductor than could be patterned using only lithography.

The inductor is characterized using an Agilent (now Keysight Technologies) 4294A impedance analyzer. The impedance and phase plots of fabricated inductor are used to characterize performance. The resulting inductor along with impedance and phase curves for the inductor can be seen below in Figure 2-7. A capacitor, resistor, and inductor circuit where all compents are in series is used to curve fit the inductor impedance curve and determine properties of the inductor. The fabricated inductor had an inductance of 1.7 μH a resistance of 3.7 Ω. An alternative approach

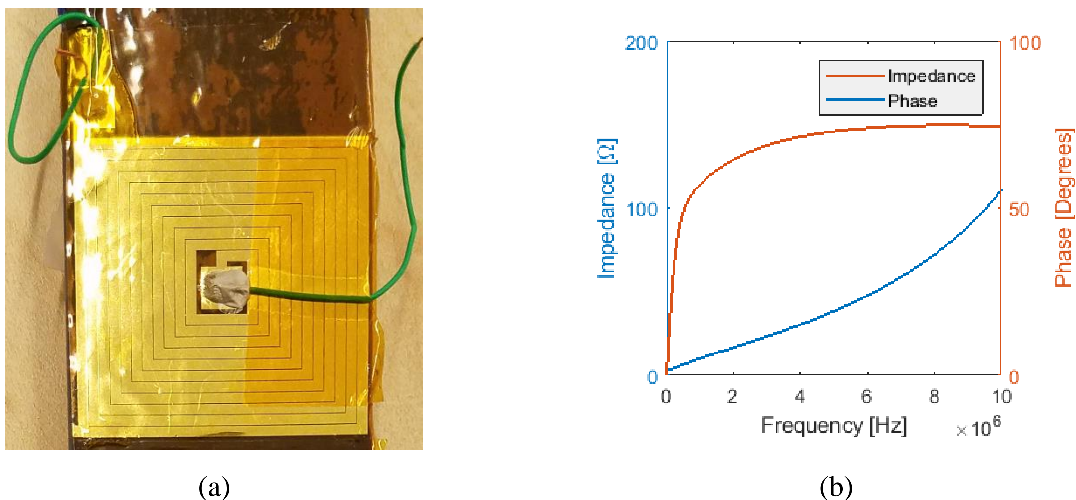

(a) (b)

Figure 2-7. (a) Image of fabricated inductor and (b) phase and impedance curves for TF inductor.

to inductor fabrication for achieving a higher quality factor with a smaller footprint is presented in Chapter 5.

2.4 Fabrication Methods for Polyimide as a Substrate and Dielectric Layer

Polyimide is thermally, chemically, and mechanically robust and functions as an ideal substrate or dielectric layer in many applications. Polyimide is especially useful in strain sensing where it has long been used as the backing material for conventional strain gages. Whether sensing for strain or other measurands, polyimide is broadly useful for conformable sensing systems [74]–[77]. Here, uses and processes for polyimide are discussed to provide a basis for design capabilities used in later chapters. Polyimide deposition, etching, and surface preparation are discussed. An example application is illustrated in the use of polyimide as a substrate and dielectric layer for capacitive strain sensors.

2.4.1 Polyimide Substrate Fabrication

Polyimide is thermally, chemically, and mechanically robust and functions as an ideal substrate or dielectric layer in many applications. The easiest use of polyimide as a substrate is to simply buy Kapton polyimide film (FT Kapton 200 HN) with a thickness of 50 microns is obtained from American Durafilm. However, the capability to spin polyimide into layers of desired thickness provides valuable design capabilities. Here, an overview of this process is laid out.

Process:

1. Spin polyimide using spinner

- Spin polyimide to desired thickness according to manufacturer's specifications. An adhesion promoter layer may be necessary prior to the polyimide layer depending on material and desired functionality.

2. Soft bake polyimide

   - Soft bake polyimide at temperature specified by manufacturer until firm to the touch.

3. Spin additional polyimide layers

   - Repeat spin and soft bake process for additional layers if a final film thickness is desired that is greater than that which can be achieved in each individual layer.

4. Cure polyimide in vacuum oven

Following soft bake of the last layer the film will need to be fully cured in an oven. This process needs to take place under a nitrogen or forming gas (nitrogen and hydrogen) environment. The curing process will include a ramp to a high temperature, such as 350 C, then then a hold at the target temperature before cooling back to room temperature.

2.4.2 Reactive Ion Etching of Polyimide

Etching polyimide is valuable as it allows for the modification of layer thickness or clearing polyimide over specific areas to allow for electrical connection to metal layers below the PI layer. Reactive ion etching can be used to etch polyimide and masked to pattern polyimide or etch only selected areas.

1. Mask etch area

   - With aluminum: An aluminum layer can be used as an etch stop to mask a polyimide etch. This can be achieved with a relatively thin (hundreds of

nanometers) aluminum layer. To do this, deposit an aluminum layer then pattern the aluminum layer using optical lithography and an aluminum etch. Perform the masked polyimide etch then strip the aluminum using an aluminum etch.

- With Kapton tape: If precise masking is not necessary a shadow mask can be made manually with polyimide and Kapton tape.

2. Etch with reactive ion etching

The material etch is a straightforward process if the necessary tools are accessible. The etch rate can be measured for a given material then the desired etch thickness can be set and achieved. Precise control of uniformity of the material deposited and etch rate can be a challenge in utilizing reactive ion etching for polyimide.

2.4.3 Polyimide Surface Preparation for Metal or CNT-Polymer TF Deposition

A few practical notes are made here on achieving adhesion between layers in thin film fabrication since this is very important for achieving quality fabrication. Without proper surface cleaning and modification delamination will likely occur between stacked thin film materials.

- Oxygen plasma etch: A short oxygen plasma "descum" etch is valuable for improving quality of patterned photoresist or activating the surface of a polyimide film prior to material deposition. Performing such a process following photoresist patterning and prior to metal deposition is a valuable best practice in such processing.
- Argon plasma etch: If exposure to oxygen is undesirable, such as when metal films are present that will corrode, an Argon plasma etch can be utilized in place of the oxygen plasma etch.

- Adhesion layers in metal deposition: A thin adhesion layer, around 50 angstroms, is needed to enhance the adhesion of many deposited metals to underlying substrates. Chromium and titanium are mainly used as adhesion layers here.

2.4.4 Illustration: Fabrication of Thin Film Capacitors

Thin film capacitors are designed using the materials and processes described in the previous sections. Capacitors are designed as square parallel plates with a polyimide dielectric layer, the capacitance of which is described by equation below where C is capacitance, d is dielectric thickness, A is the overlap area of the parallel plates, and ε is the permittivity of the dielectric material. This provides a simple geometry that maximizes capacitance over a given surface area. Gold is used for both metal layers and polyimide is used as both the substrate and dielectric. These materials create flexible thin film capacitors that are also thermally and chemically robust.

$$C = \frac{\varepsilon A}{d} \tag{2.2}$$

The process begins with a polyimide substrate bonded to a supporting silicon wafer by heating wax until melted on the wafer then placing a polyimide substrate and holding under uniform pressure until cooled. The substrate is a Kapton polyimide film (FT Kapton 200 HN) with a thickness of 50 microns is obtained from American Durafilm. The initial gold layer for bottom plate of the capacitor is then patterned using optical lithography as described in Section 2.2.1 with a chromium adhesion layer. Next, the dielectric layer is fabricated by spinning polyimide over the first patterned gold layer as described in Section 2.3.1. with surface preparation as described in Section 2.3.3. The polyimide utilized is PI-2525 from HD Microsystems, which is spun at 5,000

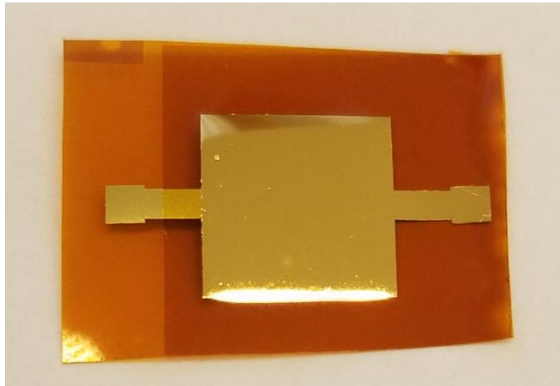

(a)

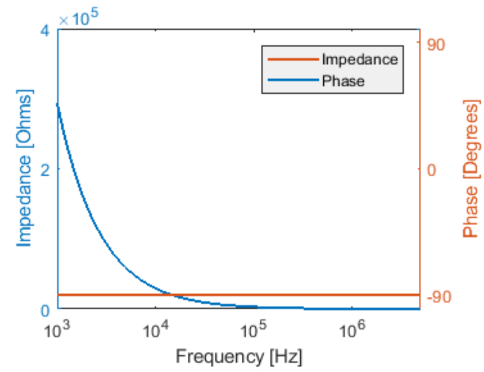

(b)

Figure 2-8. Image (a) and phase and impedance curves (b) for a thin film capacitor of 10 mm side length.

rpms for a target thickness of six microns. The polyimide is fully cured then masked with aluminum and etched in all areas that are not part of the dielectric layers as described in Section 2.3.2. Finally, a top gold layer is patterned using optical lithography.

The capacitor is characterized using an Agilent (now Keysight Technologies) 4294A impedance analyzer. The impedance and phase plots of fabricated inductor are used to characterize performance. The resulting capacitors along with impedance and phase curves for an example capacitor can be seen below in Figure 2-8. A resistor, capacitor, and inductor in series are used to fit the capacitor phase and impedance curves to provide a specific capacitance value of 531pF.

2.5 Integration of Dissimilar System Components and Rapid Research Prototyping

The processes laid out thus far in this chapter enable the fabrication of RLC thin film components, however design capabilities can be vastly extended by integrating other, potentially-dissimilar system materials and devices. These components include off-the-shelf IC electronics, which are cheap, readily available, and generally have preferable electrical performance to flexible electronics currently. Practical SHM systems are also likely to need dissimilar sensing or

mechanical materials or wires for data acquisition and interfacing with other systems. In this section, broadly valuable design capabilities for pragmatically integrating dissimilar materials and technologies are discussed. This includes concepts for system design, fabrication sequencing, and bonding. Additionally, the ability to design and test new research materials or systems is often limited by time or funding. In the practical spirit of this chapter a few methods are described for quick and inexpensive rapid prototyping and testing of thin film sensing systems.

2.5.1 Integration of Dissimilar Components

Isolation of dissimilar materials through system design and staging of fabrication can be critical to the success and robustness of SHM system design. In structural health monitoring, flexible and conformable materials are often needed along with rigid IC electronics for use in practice [78], [79]. Often, the rigid components in such systems can be isolated toward an edge or concentrated in a specific area and encased to differentiate mechanical loading between the areas designed to flex and conform and those that are not. Localizing dissimilar materials also serves the dual purpose of isolating the fabrication processes associated with the IC components from the differing fabrication processes needed for flexible system components. Efforts to separate materials and process might include bonding ICs to the rest of the system at the end of processing or potentially bonding and electrically connecting differing islands of components in the final stages of system fabrication. Additionally, even amongst thin film components there is the potential for the processing of certain materials to harm others present in the system. This can be alleviated by selecting robust materials, such as noble metals or durable polymer films, or staging fabrication so the harshest processes occur early when few materials are present if possible.

Interfacing between dissimilar components is an important consideration in design and fabrication. In the context of SHM TF systems, the most important interfacing challenges are electrically connecting thin film components with OTS components or wires in a manner that ensures the mechanical durability to withstand use conditions. Three types of connections are utilized in this work: silver paste, conductive epoxy, and soldering. Silver paste is fast and does not require low temperatures but has limited mechanical strength and durability. It is highly useful for rapid prototyping and material testing where it can be applied quickly and there is little risk from mechanical failures of the paste. An advantage of silver paste is that is can be removed with acetone and reapplied, which greatly reduces the risk of handling completed sensors as any mistakes do not cause permanent damage to the sensor. Conductive epoxy comes in many forms and with a variety of specifications and can be valuable for creating permanent electrical connections that are mechanically durable. While it is difficult to generalize considering the variety of conductive epoxies, they take longer to dry, and in some cases cure, than silver paste and often have either two phases that are mixed to initiate hardening or require heating for a curing process. Conductive epoxies take much longer to apply than silver paste but provide a permanent connection with greater mechanical robustness. Finally, soldering provides another alternative for a permanent connection between wires and thin film metals. Soldering requires high local temperatures which can damage other components or cause stresses in thin film materials and as such is best limited to isolated areas where these concerns are mitigated. The durability of connections with any of the above methods is improved by limiting the strain that connections are subject to from the wire itself. For this reason it is advantageous to use highly flexible wiring and strain relieve any wires. Strain relief is achieved by anchoring the wires near connection points

using tape, epoxy, or silicon so that strains are experienced by these mechanical anchors and not the electrical connections themselves.

2.5.2 Shadow Masking for Rapid Prototyping

Shadow masking is the use of a stencil-like mask instead of photoresist to achieve patterning in a manner like the optical lithography processes described in Section 2.2.1. For example, a thin metal plate with holes in desired areas of metal deposition can be placed over a substrate in a manner like photoresist as a metal is deposited. The removal of the plate will leave metal only in the open holes where material deposition is desired. This can be valuable in SHM-scale sensing systems as the patterning dimensions required are often much larger than those needed in device fabrication applications where photoresist patterns are commonly used. Shadow masking allows for cost savings as material designs that do not require precision can be patterned without the photoresist steps and associated mask of the optical lithography process. Shadow masking can be used to validate designs and fabrication processes prior to using conventional optical lithography for precise control and repeatability. Additionally, this provides a route to crude patterning in environments where expensive research equipment is not available. The creation of shadow masks can be time consuming so they are not recommended if fine features or numerous samples are involved. Materials such as metals, plastics, or tape are useful as shadow masks with selection depending on design and process requirements.

2.6 Chapter Summary

This chapter illustrates a fundamental set of capabilities for the design and fabrication of thin film sensors. The illustration includes the fabrication of inductor, capacitor, and resistor thin film circuit primitives and the means for integrating dissimilar materials and OTS components for

practical SHM system construction. Basic metal processing is discussed in terms of patterning, etching, and electroplating metal layers. These processes are utilized in the design and fabrication of a thin film inductor. Next, methods for fabricating, etching, and cleaning polyimide layers are described for the use of polyimide as a substrate or design layer in the creation of SHM systems. Polyimide processing is illustrated through the fabrication and testing of flexible thin film parallel plate capacitors. Next, processes for the layer-by-layer construction of nanocomposite materials are detailed. These are then utilized in the fabrication of patterned resistor elements using a CNT-polymer nanocomposite film that completes the desired set of circuit primitives and illustrates the potential of polymer-nanocomposite fabrication. The CNT-polymer composite patterning completed illustrates the use of geometry in designing bulk resistance and the impact of material composition on gage factor. Finally, best practices for integrating dissimilar components and prototyping in SHM research are described to complete the toolkit for design and fabrication of SHM systems. Approaches to design and fabrication with dissimilar SHM materials are provided along with a discussion of electrical connections between dissimilar components of these systems. The chapter concludes with a few practical notes on prototyping and testing of thin film sensors.

While the goals and approaches thin film SHM can vary widely, this Chapter provides a fundamental set of capabilities for enabling a broad set of design capabilities and for reference as specific SHM systems are designed throughout the remainder of this thesis. Fabrication of inductive, capacitive, and resistive components provides a foundation on which many SHM sensing and system approaches can be constructed. Additionally, the illustration of the use of polymer nanocomposite materials in resistive design unlocks a vast range of capabilities in this class of thin film materials. The performance requirements in practical SHM settings generally

require OTS or dissimilar components to truly utilize the thin film approaches described and an overview to these capabilities is provided.

CHAPTER 3.

FULLY INTEGRATED CARBON NANOTUBE COMPOSITE THIN FILM STRAIN SENSORS ON FLEXIBLE SUBSTRATES FOR STRUCTURAL HEALTH MONITORING

3.1 Introduction

Structural health monitoring (SHM) has emerged as an approach for structural owners and operators to assess the health and performance of their assets using quantitative data derived from sensors [1], [2]. The starting point in the design of any SHM solution is the selection of sensors for the acquisition of data pertinent to a structure's operational environment and its response to loads. A variety of new sensor types have been adopted in SHM in recent years including microelectromechanical systems (MEMS) sensors [3], fiber optic sensors [4] and piezoelectrics [5], just to name a few. Multifunctional materials in particular have shown great promise as a sensing platform in SHM applications. Multifunctional materials are material systems that have been designed for more than one functionality such as load support, sensing, actuation and power harvesting. Such materials lend themselves to a vast range of applications: for example, Hou et al. [6] used carbon nanotube composites for strain sensing, Mishra et al. [7] proposed ZnO tetrapod networks for gas sensing, Persano et al. [8] proposed arrays of nanofibers for piezoelectric pressure sensing, and Wang et al. [9] proposed a magnetic mesoporous silica nanocomposite for Hg2+ detection. The broad range of multifunctional materials and their many applications have been

reported by numerous review articles [10–13]. In the context of SHM, multifunctional materials have also been explored including self-sensing construction materials (e.g., self-sensing concretes) [16–18] and self-sensing coatings that are mechanically robust to harsh environments [17]. Multifunctional thin films can also serve as a sensing applique (or skin) that can provide spatial mappings of structural health based on repeated electrical probing (such through electrical impedance tomography (EIT)) [18–21]. Of the various multifunctional materials explored for SHM, the most promising have been composites consisting of a conductive filler dispersed in a polymer matrix [19], [22].

Past studies have largely focused on optimization of material fabrication parameters to enhance material sensing capabilities at bulk scale. This is apparent in the field of polymer composites where many researchers have attempted to optimize the bulk composite material properties using fillers such as carbon nanotubes [23–25]. Since the discovery of the carbon nanotube (CNT) by Ijima *et al.* [39] and characterization of its physical and electrical properties, many researchers have sought methods to include CNTs in composite materials in an effort to alter the bulk mechanical and electrical properties of the composite. Various methods exist to include CNTs in a composite including LbL deposition, mixing in epoxies, and spraying with polymer solutions, among others [23], [48], [49]. Early attempts at using these multifunctional materials focused on depositing them onto structural surfaces (*e.g.,* as a coating) but precise control of their placement was not a primary consideration. For example, the initial sensing skin work by Hou *et al.* [21] adopted a strategy of coating entire structural surfaces with self-sensing multifunctional materials with EIT used to create tomographic mappings of film conductivity (with EIT for SHM later advanced by Hallaji *et al.* [19] and Tallman and Wang [50]). The large number of electrodes associated with EIT is a challenge when applied outside the laboratory setting where electrode

installation is expensive and prone to damage in harsh field conditions. To realize the benefits of multifunctional materials in SHM applications, there is a need to create fully integrated thin film systems where the multifunctional material is combined with electronics to provide a more functional interface for sensor readings. Research teams have begun to explore the integration of multifunctional thin films with integrated circuitry on flexible substrates [25], [28]. A key element of integrating multifunctional thin films in a sensing system is the ability to control their deposited geometries on a substrate (flexible or rigid). Methods previously explored to pattern multifunctional thin films include inkjet printing [29], imprint (or soft lithography) [30], nano-transfer printing [31], optical lithography [32], and direct laser writing [33], among others [36–40]. Specific to SHM, Glisic *et al.* [36] proposed the integration of strain sensing elements in large-area sensing sheets for SHM applications. Flexible large-area substrates were designed with thin film silicon electronics and dense arrays of traditional metal foil strain gages integrated. While this work illustrated the benefits of fully-integrated sensing systems on flexible substrates, it relied on commercial metal foil gages as the strain sensing element.

The goal of this study is to develop a thin film sensing system that combines the benefits of multifunctional materials with conventional integrated circuitry to yield a fully integrated sensing system for SHM applications. A scalable fabrication process is needed that allows multifunctional thin films to be combined with analog and digital electronics on the same substrate to unlock the full sensing potential of the thin films. The process must also support geometric control of the thin films to allow sensing systems to be easily customized to their application. To accomplish these objectives, the study adopts optical lithography as a cost-effective method for controlling the geometric configuration of multiple material layers deposited on a substrate including multifunctional thin films offering sensing transduction mechanisms and metalized

layers that integrate the multifunctional thin film with signal conditioning circuitry for sensor readout. Another objective of the work is to fabricate the system on a flexible substrate which allows the sensing system to be installed on a variety of complex (*e.g.,* curved, rough) structural surfaces in the field. The fabrication methodology developed is intended to be scalable for the fabrication of large-area flexible sensing sheets with thin film elements included for any desired measurement configuration specific to a given SHM application.

For illustrative purposes, the study selects a thin film multifunctional composite consisting of SWNTs embedded in a polymeric matrix of polyvinyl alcohol (PVA) and polysoduium-4-styrene sulfonate (PSS) as a piezoresistive element for strain sensing [70]. This film assembly has been shown to multifunctional due to its mechanical strength (e.g., 150-250 MPa tensile strength) and the ability to encode other sensing modalities in the composite including pH and corrosion sensing [70]. Although only strain sensing is considered in this study, the processes proposed can be broadly applied to other multifunctional thin film materials. A complete strain sensing system is designed on the substrate including the use of SWNT-PSS/PVA thin films patterned as piezoresistive elements in an amplified half-bridge Wheatstone bridge configuration. The work aims to exceed the capabilities of current strain gage sensors by integrating electronics with a piezoresistive element to offer a sensor that can be integrated with a data acquisition system. Furthermore, geometric control of thin film placement on the substrate opens possibilities for deposition onto large-area sheets not possible with small, discrete strain gages such as those used by Glisic *et al.* [36]. Two prototypes are developed in the study. A first-generation prototype is developed and tested on a steel building frame exposed to cyclic lateral loading to measure strain in the web of a critical beam element. Based on its performance, the process is further refined to optimize the patterning of the multifunctional materials and maximize the robustness of the

integrated electronics. Once optimized, a set of second-generation fully integrated strain sensing prototypes are fabricated, and tensile testing performed to evaluate their mechanical-electrical response including characterization of sensor linearity and sensitivity. The outline of the paper is as follows. First, the paper begins with a detailed description of the fabrication process of the second-generation fully integrated thin film sensing system prototype. Next, the properties of the SWNT-PSS/PVA thin films are characterized by microscopic observation and profilometer measurement. The paper then presents experimental validation of the second-generation prototypes to assess their linearity, sensitivity and strain limits. Experimental tests with the first-generation prototypes are also presented to highlight how such sensors can be used in practical SHM applications including to monitor strain and damage in steel frame buildings. Finally, the paper concludes with a description of the results and a summary of the key study findings.

3.2 Fabrication of CNT-Polymer Thin Film Sensors and Integrated Electronics on Flexible Substrate

3.2.1 Materials

Kapton polyimide film (FT Kapton 200 HN) with a thickness of 50 microns is obtained from American Durafilm. PI-2525 polyimide is obtained from HD Microsystems. Polyvinyl alcohol (PVA) (fully hydrolyzed) and polysodium-4-styrene sulfonate (PSS) (M_w = 1,000,000) are obtained from Sigma-Aldrich. HiPCO (High Pressure Carbon Monoxide Process) purified SWNT with a diameter of 0.8-1.2 nm and length of 100-1000 nm are obtained from Nanointegris in powder form. SPR 220-3.0 and SPR 220-7.0 photoresist from Rohm and Haas Co., AZ 726 developer from Clariant Corporation and 4 in. (10.2 cm) diameter silicon wafers (thickness 500 microns) from Silicon Valley Microelectronics are used as supplied by the Lurie Nanofabrication

Facility at the University of Michigan. Acetone from Sigma Aldrich is used as a processing solvent. Surface mount discrete resistor components widely available from various electronic vendors are used. The instrumentation amplifier utilized is the Analog Devices AD623. Cyanoacrylate (CN) adhesive is obtained from Tokyo Sokki Kenkyuju Co., Ltd. MG Chemicals RTV615 silicone is used. EP3HTS conductive epoxy is obtained from Master Bond. Quartz Wax (0CON-200) is obtained from Logitech for bonding flexible films to rigid substrates for processing. Glass microscope slides from Fisher Scientific are used as rigid backing for the flexible substrates during LbL processing. ZeroLead surface mount solder paste (ZLSP-10CC) is obtained from Zephyrtronics. All chemical solutions for the deposition of the SWNT composites are made using 18 MΩ deionized (DI) water.

3.2.2 Overview of the Fabrication Process

The sensor fabrication process to be described herein is designed to realize any type of fully integrated sensing system that combines multifunctional thin films with electrical circuitry on a flexible substrate. For illustrative purposes, the study selects the classical Wheatstone bridge strain sensing architecture with piezoresistive CNT-polymer thin films as the strain sensitive resistive elements. The Wheatstone bridge strain sensing architecture is an ideal example to use for illustration of the fabrication process. First, it showcases the integration of circuitry with the multifunctional thin film. Second, it improves the performance of the individual piezoresistive element because it adopts a half-bridge configuration in tandem with amplification that leads to an enhanced readout sensitivity. The amplifier was further useful because it could offset the voltage allowing for easy interface between the final strain sensor and most data acquisition systems. This also allowed provided differential sensing to eliminate many upstream noise sources. While a Wheatstone-bridge strain sensor is illustrated, it should be reiterated that entirely different sensor

types can be developed by simply replacing the selected CNT-polymer with another multifunctional material sensitive to another stimulus (*e.g.,* pH, light, gases). Similarly, the Wheatstone bridge circuit can be replaced with other electrical circuits to yield a sensor with different readout capabilities. Hence, a key contribution of the work is the development of a general fabrication process for creating a fully integrated sensing system on flexible substrates using multifunctional thin films.

To develop a general fabrication process, the multifunctional material must be capable of being deposited in any shape or configuration on a substrate. Placement control of the multifunctional thin film is necessary to ensure it can be positioned appropriately on a substrate with electronics. This will be accomplished using optical lithography. While lithography offers geometric control of materials on the substrate, the fabrication process must also consider the different process parameters associated with each material to ensure the processing of one material does not alter or harm another already deposited. For example, the polymeric multifunctional thin film material for this study requires specific process parameters that create challenges when integrating them with metallic electronic layers. These include immersion of the substrate in a low pH solution and annealing at relatively high temperatures following completion of the SWNT film fabrication process. These challenges and the desire to limit exposure of the fabricated sensors to

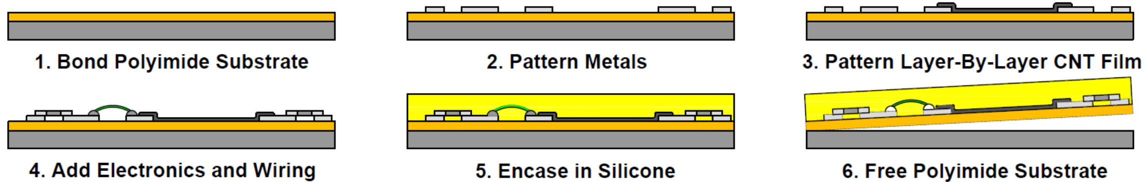

Figure 3-1. Process flow for fully integrated thin film sensing systems.

harsh temperature and chemical conditions after completion led to the design a simple but highly versatile fabrication process summarized in Figure 3-1.

The process began with a Kapton polyimide film bonded to a rigid silicon wafer for surface processing in an integrated electronics clean room environment (in this study, the Lurie Nanofabrication Facility at the University of Michigan is used). Next, a metal layer was deposited and optical lithography was used to pattern the metal layer to create electrical traces and bond pads to which sensor films and surface mounted integrated circuit (IC) components can be attached. However, the metal layer must be carefully designed to withstand both the solutions associated with the CNT film fabrication process and the high temperatures required for CNT film annealing. With this in mind, a chemically inert metal stack robust to high temperatures was deposited. A piezoresistive SWNT-PSS/PVA thin film was then deposited by LbL on the substrate with optical lithography again used for geometrical control of the final thin film placement on the substrate. The SWNT-PSS/PVA thin films were annealed in an oven to facilitate cross-linking in the polymeric matrix and to enhance material conductivity through other compositional changes. Surface mounted electrical circuit elements were then bonded to the surface of the substrate on metal bond pads. This was followed by encasement of the sensor with silicone to protect the sensor electronics and materials from the environment. Finally, the Kapton substrate was lifted from the rigid substrate to free the sensor as a conformable sensor platform for SHM applications.

3.2.3 Substrate Preparation

Kapton was selected as the substrate material for its mechanical flexibility and robustness to thermal loading and chemical exposure. Flexible Kapton substrates (50 μm thick) were used as bought from American Durafilm for the convenience and consistency of mass produced films.

Alternatively, polyimide films could be spun from solution for greater control of flexible substrate properties. Kapton films were fixed to the top surfaces of rigid silicon 4 in. (10.2 cm) wafers for processing by heating quartz wax on rigid wafers, bonding the flexible films, and then cooling the bonded materials. Kapton films mounted using wax could delaminate from their supporting silicon wafers which would adversely affect the quality of the materials deposited on the substrate during processing. To avoid this issue, flexible substrates with little initial stress should be used, stress compensation in metal stacks adopted where possible, and Kapton films lifted and re-bonded following each submersion in solution (such as solvents or etchants). Hence, the Kapton is lifted and re-bonded after each submersion in solution with Kapton tape applied at the edge of the Kapton film to firmly hold it to the silicon wafer during submersion if needed. Flexible substrates were lifted from the rigid 4 in. wafer backing using acetone; this occurred after the metals deposition and photoresist steps. Alternatively, substrates can be lifted by initiating delamination at a point on the edge of the Kapton film with tweezers then gently coaxing delamination gradually across the substrate. Remaining wax can then be cleaned from the polyimide substrate using acetone.

The lifted films were cut down to fit on glass microscope slides to allow the SWNT film fabrication process to occur using a robotic LbL assembly process. Alternatively, the substrates could have been kept on the 4 inch wafer with a manual LbL assembly process adopted. Each glass slide consisted of two independent fully integrated sensing systems with each sensing system consisting of two SWNT-PSS/PVA patterned elements (hence four SWNT-PSS/PVA patterned elements were deposited simultaneously on one slide). After completion of the fully integrated sensors, the flexible Kapton substrates were permanently lifted from their rigid backings.

3.2.4 Metal Stack Fabrication

A metal stack which was the first layer to be deposited was designed to withstand the chemical, temperature, and mechanical requirements associated with the processing of the multifunctional thin film material. Depositing the metal layer first provides a base electrode layer prior to the deposition of the various multifunctional materials. This is advantageous because attempting to place the metal layer on top of the multifunctional layer would risk not adhering to the multifunctional material and adverse changes in the properties of the multifunctional material. The metal stack was patterned using optical lithography. Optical lithography is the process of patterning layers of a material using stencil-like masks [5]. In this process, a layer of light-sensitive polymer material (*i.e.,* photoresist) is spin coated onto the planar substrate. This photoresist is exposed to ultraviolet (UV) light through a mask to alter exposed areas such that these areas can be removed by solutions (*i.e.,* developers). Photoresist films often require "soft baking" on a hot plate before exposure and "post-exposure baking" after exposure and before developing the photoresist. Here, SPR 220 – 3.0 photoresist was spun coated at 1,000 rotations per minute (rpm) on the Kapton surface, soft baked, exposed to UV light using a mask that patterns circuit traces and bond pads on the substrate, post-exposure baked and developed in a developer. The Kapton surface was then conditioned with an oxygen plasma etch prior to metal deposition to clean any remaining photoresist and enhance surface adhesion between the metal and the Kapton.

Figure 3-2. Metal stack design durable to process parameters.

The metal stack chosen was chromium, gold, silver, and platinum with layer thicknesses shown in Figure 3-2. The thin chromium layer (5 nm) functions as an adhesive between the polymer substrate and the first substantial metal layer. Platinum (50 nm) was selected as the top layer since it provides a relatively good surface for surface mount soldering and would not be corroded by the chemicals associated with the fabrication of the SWNT thin films. However, platinum is highly stressed when deposited and therefore lacked the temperature and mechanical robustness needed. Therefore, a gold layer (200 nm) was added as a highly flexible intermediate layer that would be robust to thermal and mechanical stresses. A second intermediate layer of silver (200 nm) functioned as a step layer between the flexibility of the gold layer and stresses in the platinum layer. Collectively, the final metal stack provided thermal, chemical, and mechanical robustness along with a top layer that allowed for the soldering of IC circuit components at the final stages of the fabrication process. The metals of the stack were deposited using electron beam evaporation in an Angstrom Engineering Evaporator utilized in the Lurie Nanofabrication Facility. After the desired metal stack was evaporated on the substrate, the sacrificial photoresist was dissolved using acetone leaving a patterned metal layer on the Kapton substrate. The selected layout of patterned CNT thin film sensors and the patterned metal stack is shown in Figure 3-3a. A picture of the patterned metal layer on the Kapton substrate is shown in Figure 3-3b. At this stage, a flexible substrate and electrode base that is highly durable has been achieved that can

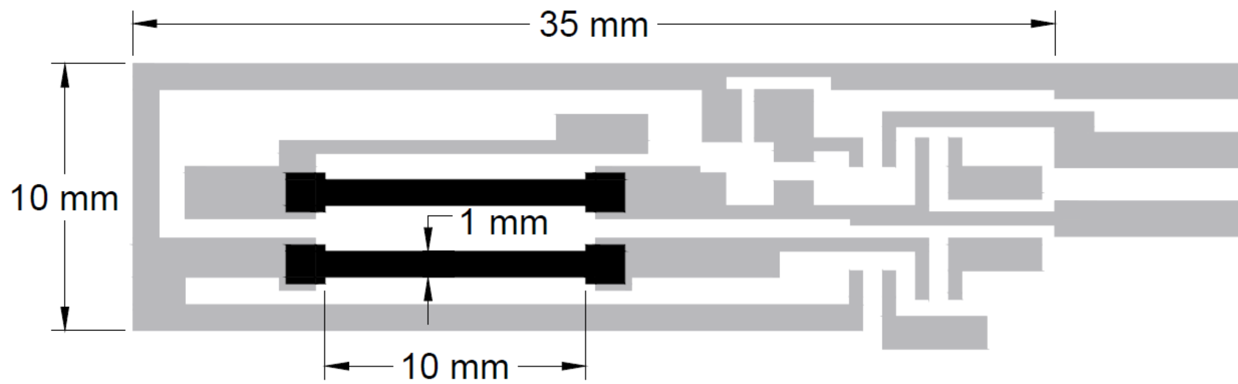

(a)

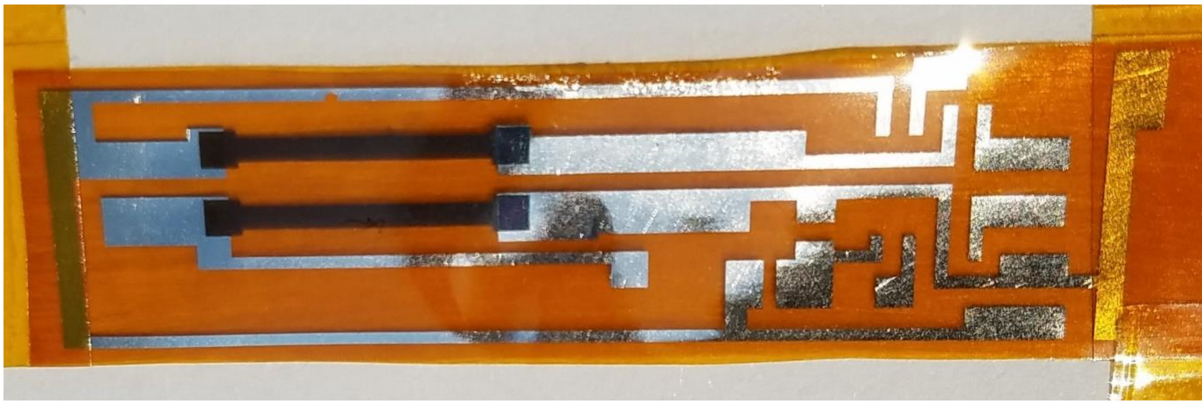

(b)

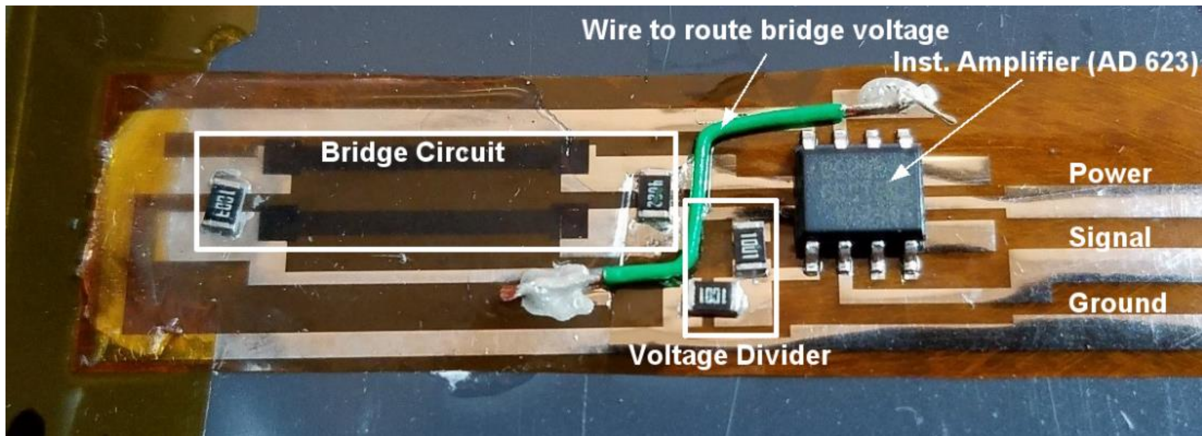

(c)

Figure 3-3. Substrate at various stages during fabrication: (a) layout of patterned thin film and metal stack; (b) patterned SWNT-PSS/PVA thin film (black strips) on top of metal stack and polyimide; (c) complete sensor.

withstand a vast set of harsh processing circumstances for various multifunctional material processes.

3.2.5 Layer-By-Layer Film Fabrication

A vital component of the fully integrated sensing system is the incorporation of a strain sensitive multifunctional thin film material as resistive elements of a half-bridge Wheatstone bridge sensing readout circuit (*i.e.,* R_s in Figure 3-4). A piezoresistive SWNT-PSS/PVA thin film was assembled based on an LbL deposition process [51]. The LbL assembly process is an established deposition method for polyelectrolyte multilayer (PEM) thin films where electrostatic adhesion is exploited between oppositely charged polyelectrolytes to sequentially build a cohesive film. This allows for precise fabrication control, as a substrate is sequentially dipped in two solutions of oppositely charged polyelectrolytes to build up a well-controlled thin film assembly with uniform morphology. In this work, a polycationic solution of 1.0 *wt.* % PVA and polyanionic solution of 1.0 *wt.* % PSS were adopted. SWNTs were dispersed in the PSS to act as a conductive filler. Past work has shown PSS can serve as a non-covalent dispersive agent preventing

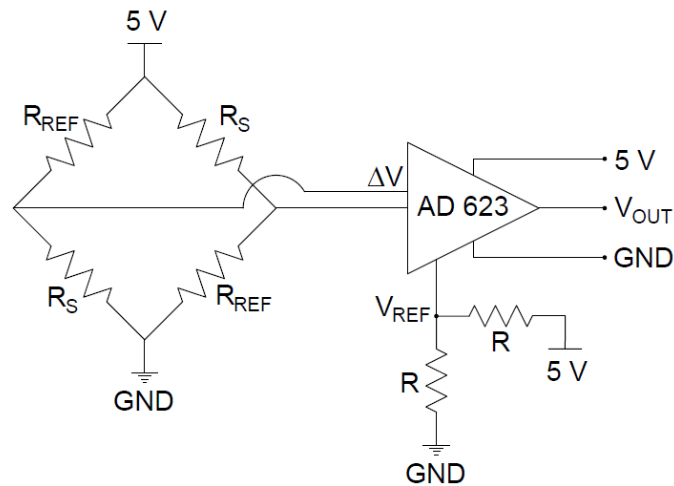

Figure 3-4. Schematic of the Wheatstone bridge circuit of the fully integrated CNT thin film strain sensor (with reference surface mount resistors, R_{ref}, and strain-sensitive thin film resistors, R_s).

agglomeration and precipitation of SWNTs from a solution, which is a common challenge in CNT composite fabrication [51]. The concentration of SWNT in the PSS solution was 1 mg/ml; sterically stabilized dispersion was achieved through multiple stages of ultrasonic agitation. The ultrasonic agitation began by placing 20 mL vials of solution in an ultrasonic bath (135W, 42 kHz, 180 minutes) followed by transferring solution in 80 mL volumes to 100 mL jars for deep tip sonication (3.178 mm tip, 150W, 22 kHz, 30 minutes). The fabrication process was automated using LbL robotic assembly equipment (nanoStrata StratoSequence) using process parameters (e.g., dip, rinse and dry times) identical to previous work reported in [51].

The LbL deposition of the 35 bilayer SWNT-PSS/PVA thin film was conducted on the Kapton substrate. Similar to the metal stack, two multifunctional SWNT-PSS/PVA thin film elements were to be patterned at locations in a Wheatstone bridge circuit. Here, SPR 220 7.0 photoresist was spun at 2,000 rpm for a target thickness of around nine microns to pattern the polymer composite sensor film. After LbL deposition the sacrificial photoresist was removed using a stripper solvent with bath sonication adopted to aid in the tearing of the mechanically robust SWNT-PSS/PVA thin film during liftoff. The SWNT-PSS/PVA thin film was then annealed in a convection oven where the temperature was ramped to 250°C at 5°C/minute and held at 250°C for 20 minutes. The substrate at this point was populated with patterned metal traces and SWNT-PSS/PVA thin films. A picture of the substrate with the SWNT-PSS/PVA thin film patterned is shown in Figure 3-3b.

3.2.6 System Construction

Once the fully integrated sensor had been fully processed (*i.e.,* SWNT-PSS/PVA thin films deposited, patterned, and annealed), the sensing system was completed by adding wires and off-

the-shelf components that could not have survived previous stages of fabrication. In this study, these were surface mount soldered conventional passive (*i.e.,* resistors) and an instrumentation amplifier. Soldering of these discrete electrical elements illustrates the completion of the full integration of circuitry with the multifunctional materials.

In the design of the thin film strain sensing system (Figure 3-4), two major IC components required mounting: an instrumentation amplifier (Analog Devices AD623) and surface mount resistors. The surface mount resistors (denoted as R_{REF} in Figure 3-4) were used to complete the two sides of the Wheatstone bridge with a third resistor used to tune the gain on the instrumentation amplifier. In this specific study, unity gain of the instrumentation amplifier was used. Non-unity gain of the bridge voltage allows for higher sensor sensitivities but if the bridge is not well balanced (due to variations in the bridge resistances), the initial bridge offset will also be amplified. The scale of the response is, in part, set by the excitation voltage on the bridge, which is five volts (5 V) for all sensors tested in this paper. The two surface mount resistors were selected during fabrication to properly balance the bridge based on measurement of the SWNT-PSS/PVA thin film nominal resistance (R_s) as measured by an Agilent 34401A digital multimeter (DMM). These components were soldered directly to the metal stacks as shown in Figure 3-3. One challenge in the design of the fully-integrated strain sensing system is the need to route one of the Wheatstone bridge voltages to the instrumentation amplifier. To make this connection, a flexible metal wire was bonded to the surface of the thin film to close the Wheatstone bridge circuit; the wire was bonded to the metal pads using conductive silver epoxy. The final fully integrated strain sensor encased in silicone is shown in Figure 3-3c.

3.2.7 Process Yield

Fabrication variations and the manual aspects of the fabrication lead initially to a less than perfect yield of around 50%. Major threats to successful fabrication were the uniformity of the SWNT-PSS/PVA films deposited, poor on-film electrical connections, and imperfect IC bonding during the final stage of instrumentation. The yield improved dramatically to well above 50% as the process was perfected and high-risk fabrication steps were more carefully executed. The yield achieved was expected for an academic clean room environment; there is nothing to suggest that industrial fabrication using the standard techniques adopted would not achieve yields approaching 100%.

3.3 Film Characterization

The thin films fabricated were imaged to investigate the quality of CNT dispersion and lithographic patterning of the metal stack and SWNT-PSS/PVA film. Qualitative characterization of the quality of the SWNT-PSS/PVA film at the perimeter of the patterned area was of great interest. The perimeter is where the film is torn during the stripping of the sacrificial photoresist layer. Films were imaged first with an optical microscope for low resolution observation followed by use of a scanning electron microscope (SEM) for more detailed investigation at smaller length scales. Here a Hitachi SU8000 cold field emission SEM available in the Lurie Nanofabrication Facility was used.

Example microscope images of the edges of nanocomposite films can be seen in Figure 3-5. Figure 3-5a shows a 35 bilayer SWNT-PSS/PVA thin film patterned with a 1 mm width on top of the metal stack while Figure 3-5b shows the same film away from the metal stack on top of the polyimide substrate. The two optical microscope images show the general pattern quality with the

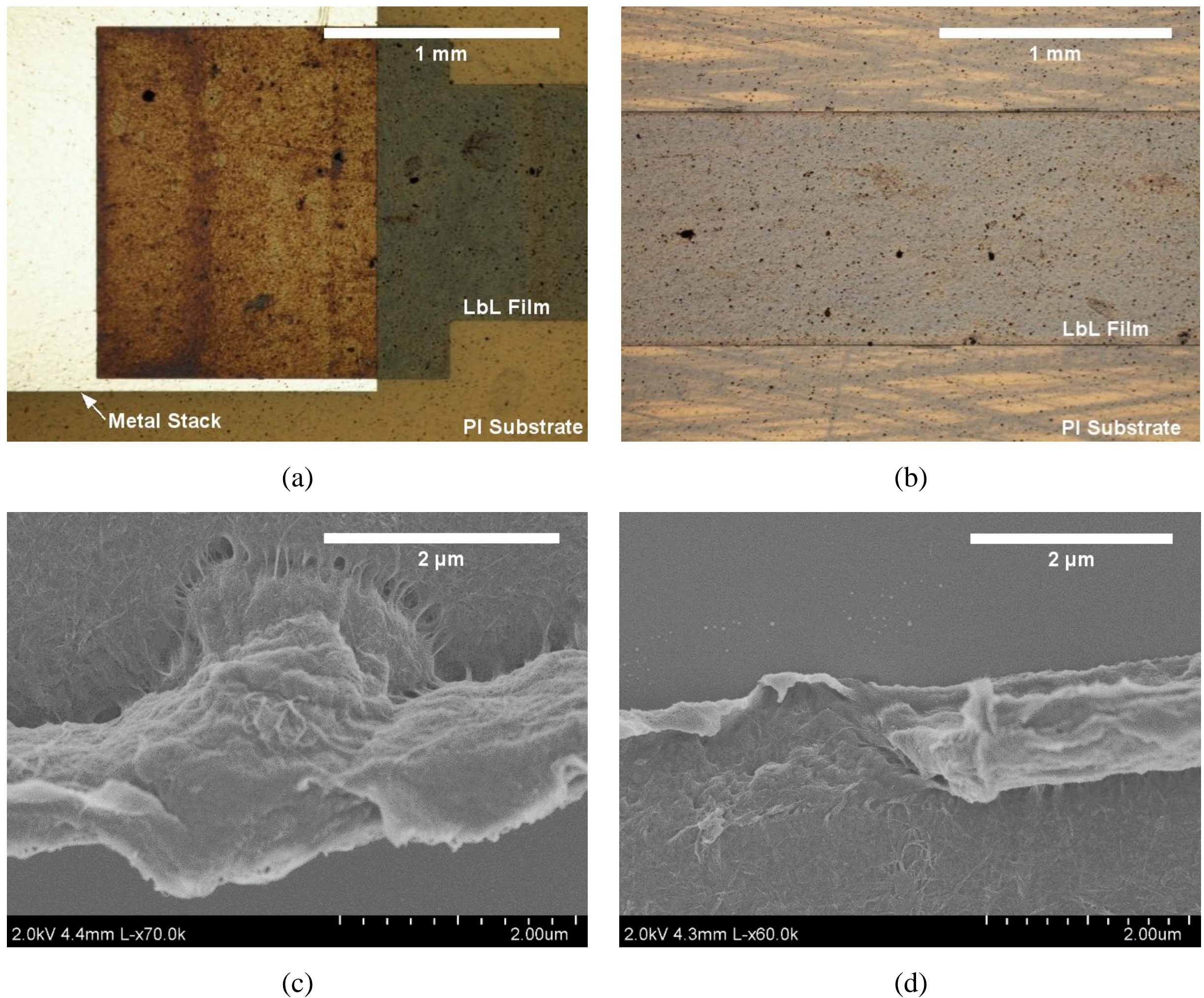

Figure 3-5. (a) Optical microscope view of CNT thin film sensor connection to bond pad on polyimide (PI) substrate; (b) optical microscope view of patterned CNT thin film on PI; (c) and (d) SEM image of CNT patterned film at perimeter where tearing mechanisms are evident.

geometric areas of the thin film clearly defined. Also, the film is well integrated with the metal layer in Figure 3-5a ensuring a good electrical contact is made. In Figure 3-5c and Figure 3-5d, the two SEM images display the limitations of patterning through lithographic methods. In both figures, the tearing mechanism of the polymer composite during liftoff is evident. Clearly, the liftoff process is affected by the presence of SWNT bridging the defined liftoff boundary; during liftoff, these SWNT must be pulled from the matrix leading to a rough finished edge. For example, in Figure 3-5c a 2-micron wide area on the perimeter where the film is lifting from the substrate can be observed. Evident in the center of the area is a spherical mass of film curling up from the

substrate with SWNT ropes bridging between the curled mass and the film on substrate. Away from the torn perimeter, the SEM images reveal a relatively uniform morphology of the SWNT-PSS/PVA film with the SWNT well dispersed in the composite. These features were consistently found in most of the films fabricated. Hence, it was concluded that the lower limit on film planar feature size was near that of conventional lithography methods (which is around two microns). There was also no noticeable deterioration of pattern quality with decreasing feature sizes such as thin film width. Figure 3-6 shows an optical microscopic view of a 35 bilayer SWNT-PSS/PVA patterned as a 10 micron thick sensor element on glass. Near the bond pad in Figure 3-6a, there was some difficulty in achieving the film geometry during lift-off with small areas of film not lifting where desired. However, away from the bond pad area, the liftoff of the film is more complete as shown in Figure 3-6b.

To complement the qualitative aspects of film microscopic imaging, film thickness was measured as a quantitative metric of film uniformity and geometric consistency. Figure 3-7 displays the thickness of each SWNT-PSS/PVA thin films fabricated at 3 different locations using a profilometer. Four SWNT-PSS/PVA thin films (two to each of the two integrated strain sensing

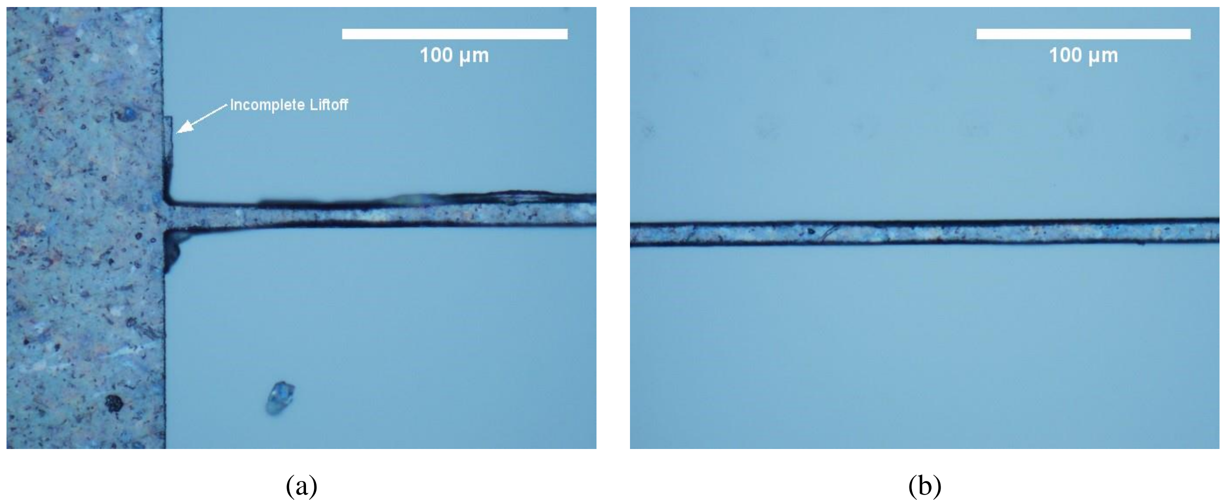

(a) (b)

Figure 3-6. Optical microscope images of 10 micron wide SWNT-PSS/PVA thin film: (a) patterned thin film at the bond pad; (b) away from the bond pad area.

systems) were deposited as 35 bilayer films on polyimide bonded to each glass slide using LbL. Four glass slides were processed in the LbL robotic assembly process at the same time. Hence, Figure 3-7 presents the profilometer data for each SWNT-PSS/PVA strip (termed “strip 1” and “strip 2”) in each fully integrated sensor (termed “bridge 1” and “bridge 2”) per slide (termed “slide number”). The first bridge of the first glass slide was damaged in one location during processing (as confirmed by visual observation) and as such only two values were noted for these sensing strips. The sensors showed relatively consistent thicknesses of around 0.3 microns, although the process does lend itself to some variability. The average thickness is denoted for each strip in Figure 3-7.

The geometry of the patterned SWNT-PSS/PVA element (strip) provides an additional design parameter for influencing resistance values and consistency of those values as was shown in a previous study [84]. It was found in that study that extremely narrow SWNT-PSS/PVA widths lead to higher resistances with values stabilizing as film widths increase. A design width of one millimeter was selected for this study based on the previous study, however narrower widths could

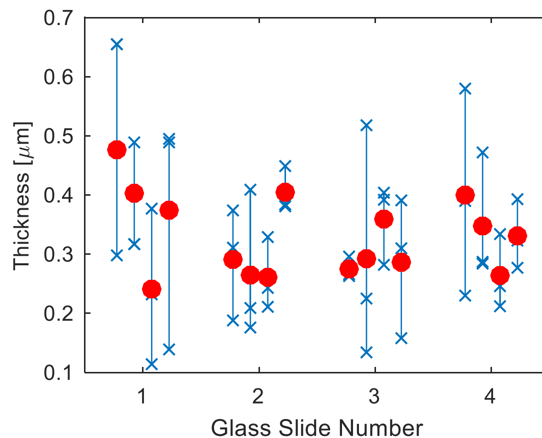

Figure 3-7. Profilometer showing film thickness at three locations on each SWNT-PSS/PVA patterned film (termed “strips”). Measurements are taken at the top, middle, and bottom of each sensor are indicated (x) while the mean is indicated with a circle (note that each strip on slide 1 bridge 1 was limited to two data points due to film damage).

have acceptably yielded a similar resistance value should this be required by a different design scenario. Similarly, the number of SWNT-PSS/PVA bilayers could be adjusted. More bilayers provide mechanical robustness and film resistance consistency. However, as CNT films are made thicker (with more bilayers) the films eventually become very difficult to tear during liftoff due to the presence of the CNT, even when relatively thick photoresists were used. The 35 bilayers selected was an empirically arrived at point where films had stable, desired electrical properties and could be lifted with the photoresists readily available in the facility used for fabrication.

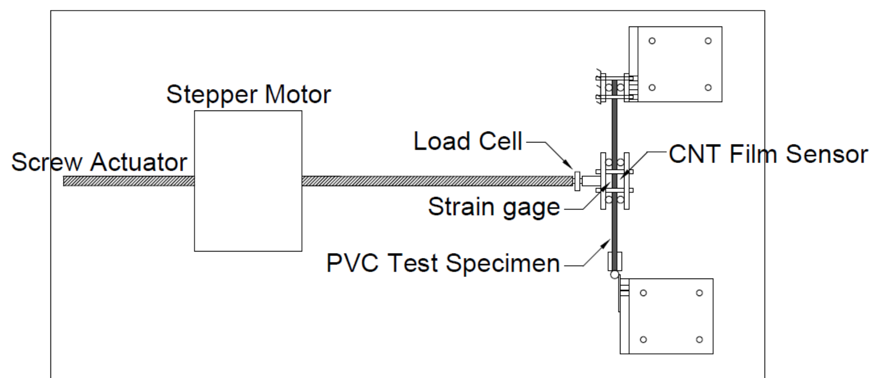

(a)

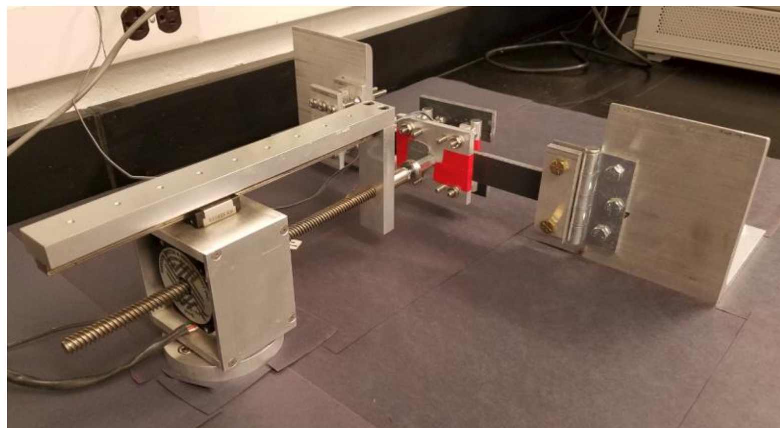

(b)

Figure 3-8. (a) Schematic and (b) photograph of load frame used to test sensors.

3.4 Experimental Validation

The validity of the sensing system is confirmed by testing several fabricated sensors on a laboratory load frame that loads small coupons in four-point bending. The test frame is comprised of a displacement-controlled, turn screw linear actuator made by Haydon Switch & Instrument Inc., a custom 4-point bending sample fixture, and mounting frame containing end connections for the specimen. The turn screw actuator is powered by a National Instruments (NI) MID-7602 integrated stepper motor power drive. One limitation of this system is that open-loop displacement controlled actuators are prone to drift at high displacements as will be seen later as sensors are tested to failure. This was not a concern here as all strains were confirmed with a traditional strain gage independent of the actuator. The test frame is shown in Figure 3-8. A strain gage (part number FLA-2-23-3LT from Tokyo Sokki Kenkyujo Co., Ltd.) was placed opposite each sensor tested on the test specimens to confirm the strain seen in each test. Voltage signals from the strain gages and fully integrated prototype sensors were collected using a National Instruments-8101 controller with PXIe-6124 data acquisition (DAQ) cards. The frame was controlled and data was collected using NI Labview on a controlling computer. Data was collected from sensors without loading prior to testing to allow for noise and drift analysis. Sensors were tested using polyvinyl chloride (PVC) coupons 10.25 in. (26 cm) long with a 1 in. (2.54 cm) by 0.25-inch (0.64 cm) cross sectional area. The fully integrated sensor and the commercial metal foil strain gage were both mounted at the same longitudinal location on the coupon (*i.e.,* at the center of the coupon) but on opposite surfaces. The coupon was cyclically loaded to allow each sensor to see tension and compression of varying levels of magnitude.

Five fully integrated strain sensor prototypes were tested with each prototype subjected to a battery of tests. First, the SWNT-PSS/PVA film resistances were measured using a digital

Sensor Number	Left Bridge Strip R_0 [Ω]	Right Bridge Strip R_0 [Ω]	Sensitivity [V/ε]	Average Linearity	Strain Limit
1	3890	3560	-5.5	0.997	-
2	3330	3610	-4.8	0.980	-
3	3290	3220	-5.1	0.998	-
4	4530	3980	-5.9	0.998	+10,000/ -17,000
5	3820	4220	-5.5	0.998	+10,000 /-17,000

Table 3-1. Initial resistance of CNT films, bridged sensor sensitivity, linearity, and limit strains for the five sensors tested (note that positive strain is tensile strain).

multimeter at a state of zero applied strain. Second the coupon was cyclically displaced through four cycles with peak strains of 500 με applied over 75 seconds. Third, the coupon was again cyclically displaced through four cycles but with peak strains of approximately 3000 με over 70 seconds. Fourth, the coupon was loaded over one cycle to approximately 3000 με but at the second tensile peak, the load is held for 30 seconds before completing the second cycle. The last test was reserved to test the prototype to failure with cycles of increasing amplitude tested until failure of the prototype.

The resistance of each strip of the sensor, as measured using a digital multimeter before loading, was observed for five minutes prior to cyclic loading of the PVC bar. This testing displayed a small drift upon powering up that has been previously reported for similar SWNT-composite thin films [51]. After stabilizing, the nominal resistance was measured and reported in Table 1. The resistance of the strips varied for the same sensor between 2% (Sensor 3) and 14% (Sensor 4). The variation in strip resistances in the same Wheatstone bridge circuit resulted in a small output bias voltage by the sensor. The response of Sensor 2 to the three cyclic load tests is shown in Figure 3-9. The sensor clearly tracked strain linearly with a high sensitivity. In Figure 3-9a, it is evident that a very small drift is still present in the sensor output due to differential drift between the two strips in the same sensor platform. The sensitivity was observed to range between 4.8 V/ε (Sensor 2) and 5.9 V/ε (Sensor 4). As can be seen in Figure 3-9, the response was highly

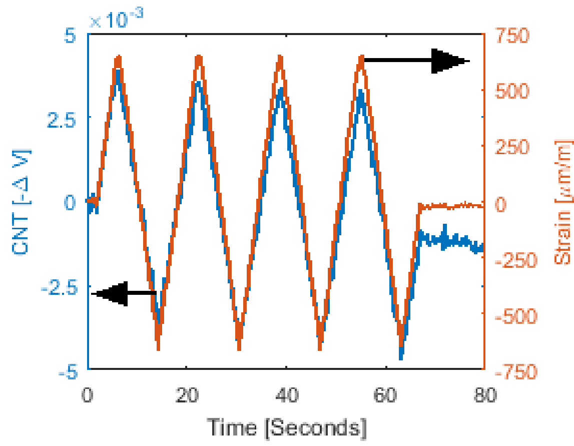

(a)

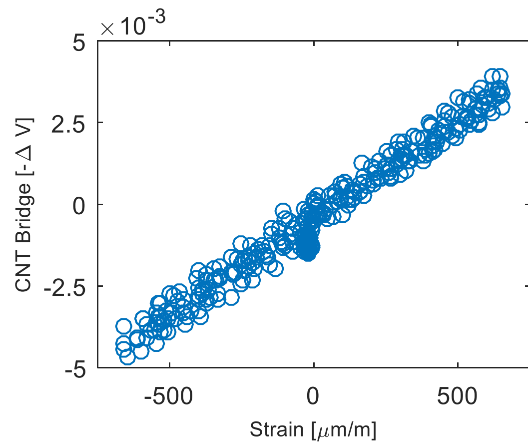

(b)

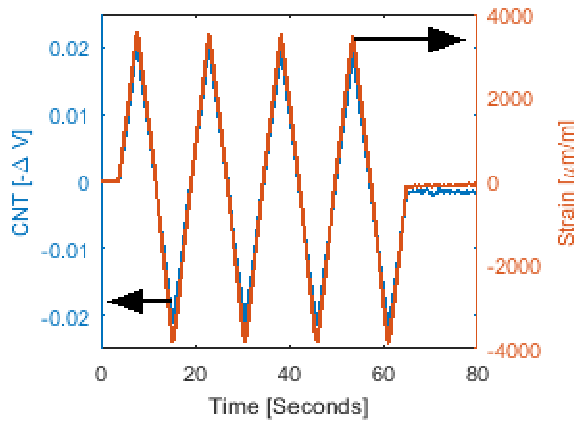

(c)

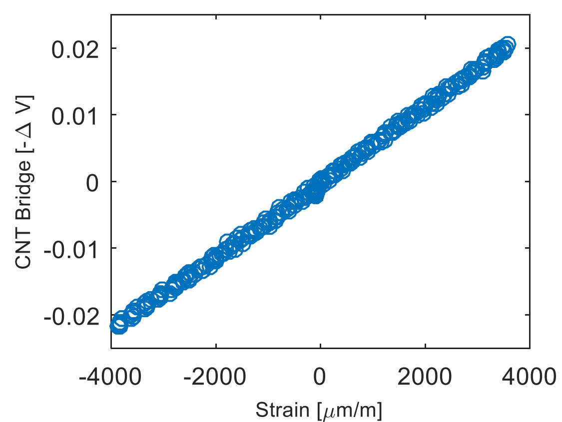

(d)

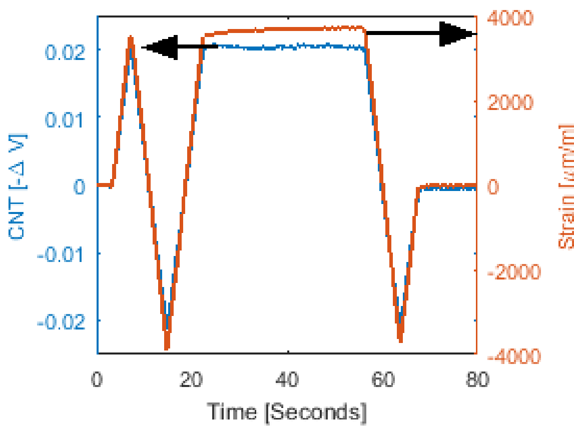

(e)

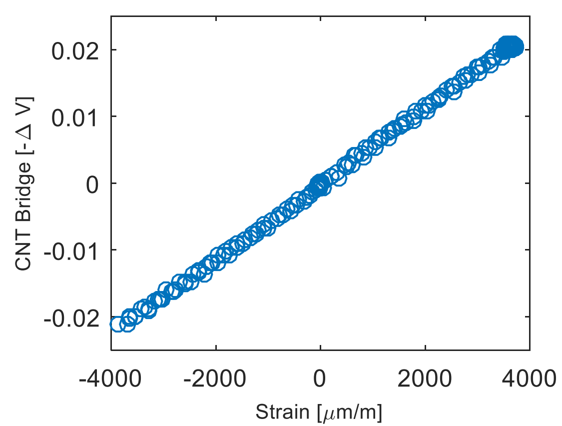

(f)

Figure 3-9. Fully integrated strain sensor: time history of strain and change in output voltage of Sensor 2 for (a) 4 cycles of ± 500 με, (c) ± 3000 με, and (e) two cycles of ± 3000 με with pause at the second tensile peak; corresponding output voltage versus strain for (b) 4 cycles of ± 500 με, (d) ± 3000 με, and (f) two cycles of ± 3000 με with pause at the second tensile peak.

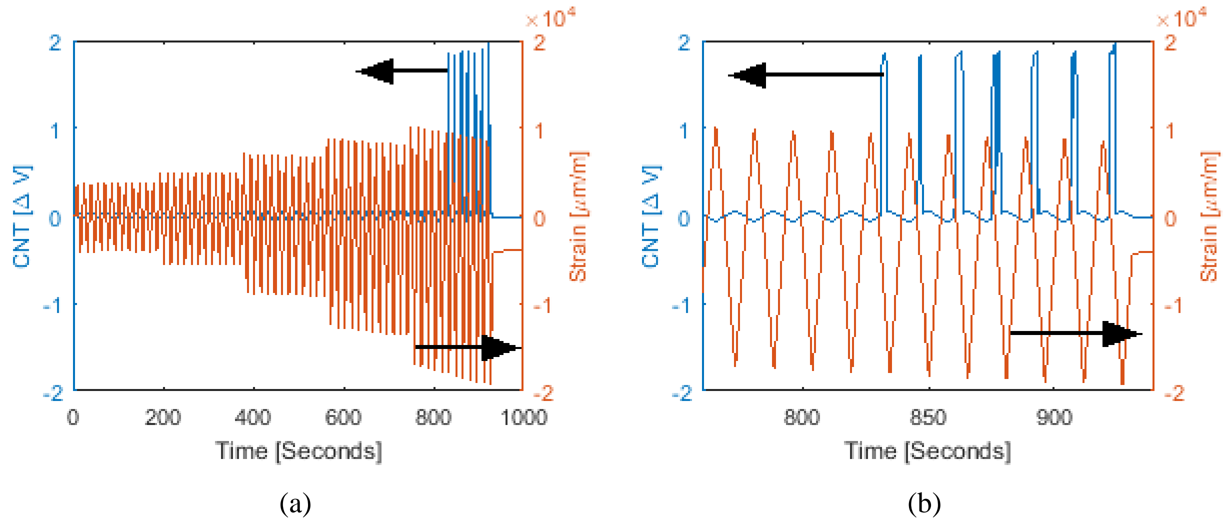

(a) (b)

Figure 3-10. Sensor 4 strain time history of measured strain (by metal foil gage) and fully integrated sensor output voltage: (a) from 0 to 1000 seconds; (b) from 700 to 1000 seconds. .

linear. Linearity, as defined as the R–squared measured of a linear regression, is quantified for the test of applying four cycles of 3000 με. Linearity was greater than 0.98 for all 5 specimens.

In the final round of testing, two of the five fully integrated strain sensors were tested to failure (*i.e.,* Sensor 4 and 5). Failure tests were designed to begin near the previously tested value of 3,000 microstrain which is already past the yield strain of steel. In both tests, it should be noted that the open-loop actuation of the load frame resulted in a drift in the turn screw actuator. This mean drift is most pronounced at high strains resulting in unintentional asymmetry in the applied strain profile of the coupon. The result was much higher compressive strain, as measured by the gage, than tensile strain due to actuator drift throughout the test. The measurements taken remain valid as they are referenced to the gage on the PVC specimen and not the actuator. Figure 3-10 and 11 shows the failure modes of the two fully integrated strain sensor prototypes. In Figure 3-10, Sensor 4 was loaded cyclically with increasing amplitude to 10,000 με in tension and 17,000 με in compression. After repeated loading at a strain level above 16,000 με in compression, an electrical connection was broken on the sensor causing the sensor output to saturate in a certain

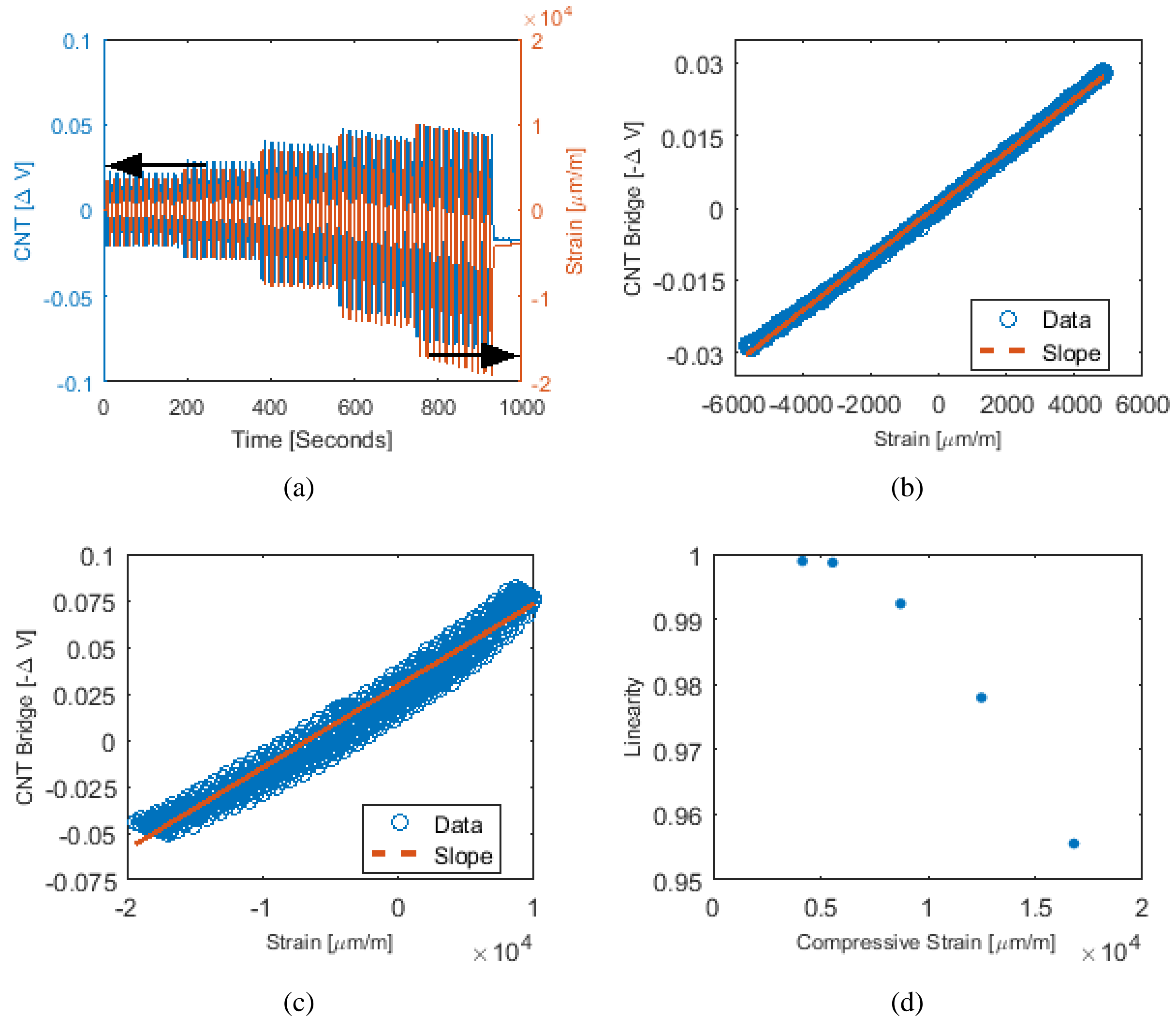

Figure 3-11. Sensor 5 loaded to failure: (a) strain time history of measured strain (by metal foil gage) and fully integrated sensor output voltage; (b) corresponding output voltage versus measured strain for load cycle to 5,000 microstrain; (c) sensor functioning with nonlinearity in final load cycle; (d) linearity of sensor as strain is increased to failure.

strain range. Sensor failures were generally caused by the breakage of the soldered bonds of IC components to the metal stack resulting in the railing of the output signal. Sensor 5 is shown in Figure 3-11; here the sensor withstood the high levels of tensile and compressive strain. The sensor was shown to be highly linear past the strain ranges applicable to SHM applications addressed here until linearity began to decrease at around 8,000 με as shown in Figure 3-11. At strain levels nearing 8,000 με the sensor began to exhibit some hysteresis. It is hypothesized that hysteresis

occurs since the material has begun to deform plastically at these strain levels. A material of similar composition was previously tested by Loh [85] exhibiting a linear-elastic limit of around 10,000 $\mu\varepsilon$. Since the material tested in that study was SWNT-PSS/PVA comprised of 200 bilayers as compared to the 35 bilayers used here, it is expected the 35-bilayer material would experience plastic deformation at strain values lower than those previously observed in the 200 bilayer films. Testing was continued to high failure strains to show the robustness of the fabrication process and sensor design but this paper will leave extensive multifunctional material characterization to the numerous material optimization studies referenced earlier [85].

Additionally, analysis was conducted to quantify the noise present at the output of the fully integrated sensing system. The fully integrated sensors were found to have a root-mean-squared noise level of around 0.2 mV. Using an identical electrical readout circuit, a traditional metal foil strain gage was also tested to assess its root-mean-squared noise level; it was found to have a noise level of 0.08 mV which is 2.5 times smaller. The noise is hypothesized to be primarily due to the noise associated with the SWNT-PSS/PVA composite and could be addressed in a future study more focused on material optimization.

3.5 Monitoring a Steel Beam-Column Under Lateral Loading

Two fully integrated strain sensors were tested on a partial scale steel structure to experiment with the sensors (including how to install them) in a realistic structural health monitoring application. These experiments were executed prior to the optimization of the fully integrated strain sensor process development previously described. These first-generation prototypes were identical to second-generation counterparts except for three major differences. First, the polyimide substrate was spin coated onto the substrate as opposed to being purchased as

a commercial Kapton film. PI-2525 polyimide was spun coated onto a silicon wafer at 2000 rpm resulting in a 12 μm thick film. Second, the SWNT-PSS/PVA 35 bilayer film was annealed on the spin coated polyimide films before release from the rigid substrate. Third, the top layer of the metal stack was 2 microns of copper (deposited on the 5 nm chrome layer) to allow for soldering of the integrated circuit components to the metal layer. Additionally, the electrode layout was more general for the first-generation prototype requiring additional bridge balancing resistors compared to the final second-generation optimized design. The sensors were fabricated at the University of Michigan using the same steps detailed in Figure 3-1 and transported to the Disaster Prevention Research Institute (DPRI) at Kyoto University for attachment to a steel building sub-assembly tested for seismic performance assessment.

The DPRI steel structure assembly consisted of one steel I-beam (H-100x60x6x8) that was 39.4 in. (1 m) long and a square tube steel column with a cross sectional area of 3.94 in. (100 mm) by 3.94 in. (100 mm) and 0.35 in. (9 mm) thick. The column was 39.4 in. (1 m) tall with the beam welded to the column face at its half point. Attached to the beam was a concrete slab designed to

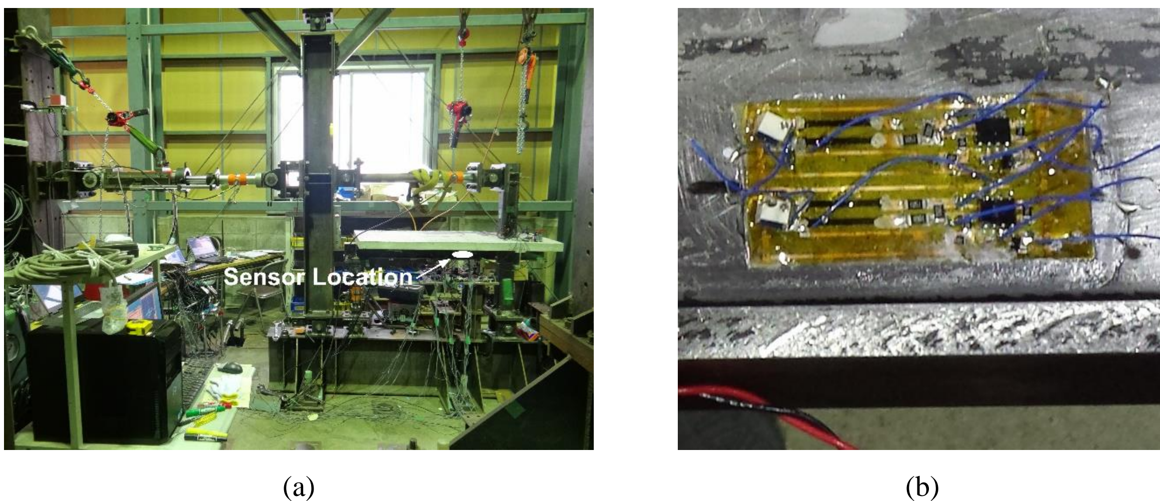

(a) (b)

Figure 3-12. (a) Steel frame test assembly for cyclic load testing; (b) two prototype fully integrated strain sensors were located on the beam web near the bottom flange 13.8 in. (35 cm) from the edge of the column.

be in composite action due to shear studs welded to the beam top surface 1.57 in. (40 mm) apart. The free end of the beam was attached to a pin connection while the top and bottom of the column were also attached to pin connections.

The two sensors were bonded on location at DPRI to the web of the steel beam at a distance of 13.8 in. (35 cm) from the column face. The bonding process required cleaning the structure by sanding the sensor location then wiping the sanded surface with acetone. The sensors were then

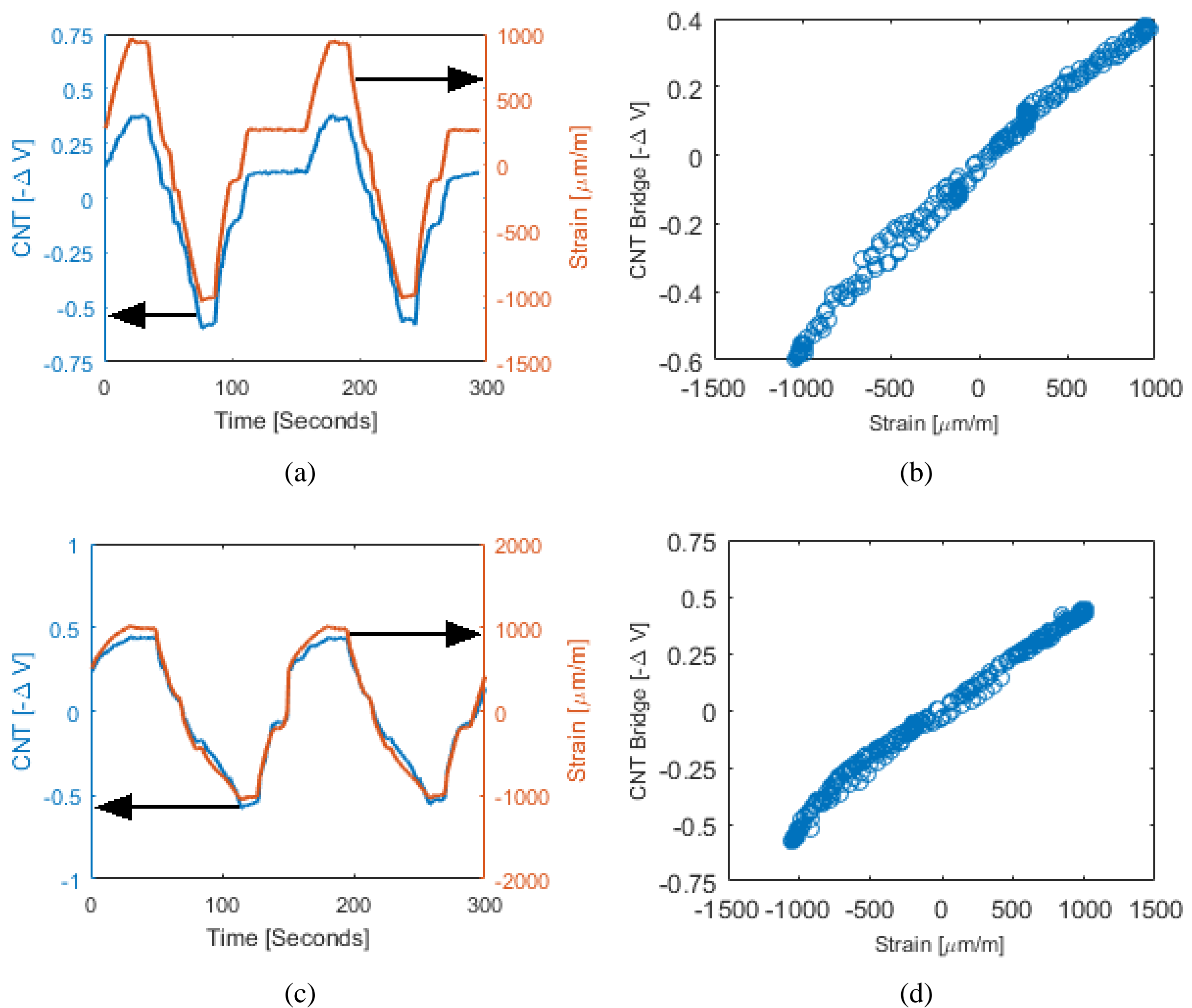

Figure 3-13. Web strain of steel beam-column assembly under cyclic loading: (a) metal foil measured strain and fully integrated strain sensor output time histories and (b) corresponding output voltage versus strain as measured 0.87 in. (22 mm) above the flange at 2% column displacement; (c) metal foi measured strain and fully integrated strain sensor output time histories and (d) corresponding output voltage versus strain as measured at 3% column displacement.

bonded to the structure with CN Epoxy. The sensors were placed 0.47 in (12 mm) and 0.87 in. (22 mm) from the top surface of the bottom beam flange as shown in Figure 3-12. Traditional metal foil strain gages were placed on the opposite side of the web in locations identical to the location of the fully integrated strain sensors. The outputs of the strain gages and fully integrated strain sensors were interfaced to a wireless sensor node (*i.e., Narada* nodes [43–45]) for data collection. The specimen was loaded at the top of the column with a hydraulic actuator in incremental cycles gradually from small displacements to eventual failure at 6% drift at the top of the column. The measured strains at two different loading levels are presented in Figure 3-13. The response of the fully integrated strain sensors tracked the strain measured by the gages located on the opposite face of the web. When the strain sensor voltage output was compared to the measured strain gage reading, a linear response was observed with a slope (sensitivity) of 1.5 V/ε and a linearity greater than 0.9. It is important to note that the sensitivity of the deployment prototype differed from that of the optimally robust prototype (around 5 V/ε) due to the aforementioned changes made in the process steps between the two prototypes. The primary cause for this is that the generality of the first prototype resulted in a need for significant handling and soldering close to the sensing strips in the Wheatstone bridge. The heat associated with soldering likely caused local damage to parts of the polymeric films that increased their bulk resistance and lowered their gage factor. Such issues were easily alleviated in the second-generation design with a slightly different metal layout along with the other processing improvements aimed at preventing high heat exposure of the SWNT-PSS/PVA thin films.

Testing was continued until final failure of the structure which was a fracture failure of the beam-column connection as shown in Figure 3-14d. A major failure event can be seen in Figure 3-14a where the fully integrated strain sensor experienced a sudden peak at 100 seconds and then

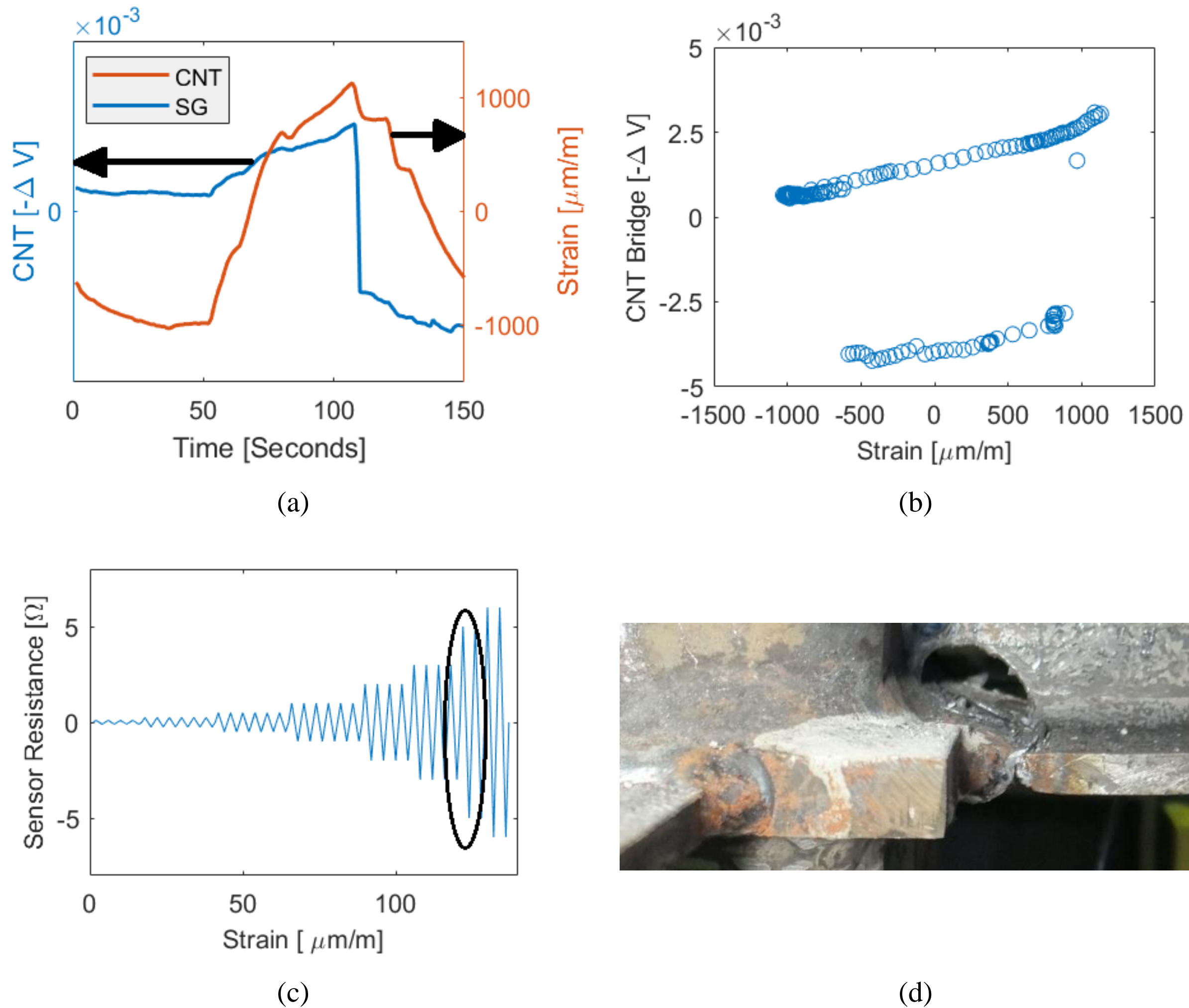

Figure 3-14. Fully integrated sensor observing damage on steel structure: (a) time history of fracture event as measured by prototype fully integrated strain sensor and traditional metal foil gage; (b) strain sensor output versus strain during fracture event; (c) failure point in test loading procedure; (d) image of beam flange fracture observed.

settled to a lower bridge output. A dramatic drop in the measured strain of the strain gage can also be observed at the same time. It is hypothesized that the fracture event shock wave propagating through the steel elements resulted in damage to a soldered connection in the fully integrated strain sensor resulting in a change in the balanced Wheatstone bridge. The sensor remained functional (albeit with a new offset) for the remainder of the test. The linearity and sensitivity of the sensor remained above 0.9 and 1.5 V/ε, respectively. The film and metal layers were investigated after testing and it was confirmed that the SWNT-PSS/PVA had a bulk resistance similar to that at the

test outset while the metal stack remained conductive through-out. Small cracks in the solder beads evident at the IC components suggest brittle failure of these materials due to the shock wave.

3.6 Chapter Summary

While multifunctional materials pose great promise for various SHM applications, there is a need to integrate them into sensing systems in a manner that is cost-effective and scalable. In doing so, their promising capabilities can be realized. In this study, a fully integrated strain sensor is designed using a self-sensing SWNT-PSS/PVA thin film system. A key contribution of the study is a scalable fabrication process that integrates multifunctional thin films patterned in any desired planar geometry with an electrical readout circuit on a flexible substrate that can be used as a large-area sensing skin on structures. The study used a strain sensor design based on LbL-deposited SWNT-PSS/PVA thin films as its illustrative example with a fully integrated strain sensor produced. By integrating electronics with piezoresistive thin film elements, a complete strain sensor is produced which is more convenient than a traditional strain gage which is only a piezoresistive element. Furthermore, the fabrication process is versatile and is capable of using different multifunctional thin film materials to produce other sensor types, even on the same substrate as a piezoresistive element. The proposed process began with a flexible substrate on which a metal stack was patterned. The metal stack was designed to be durable to high temperatures, chemical exposure, and mechanical loading. A LbL fabrication process followed by lithographic lift-off was used to pattern polymer nanocomposite materials on the flexible substrate. In the final fabrication step, surface mount IC components were added to complete the readout circuitry. The completed systems was encased in silicone for ease of handling and to lend additional robustness to the films allowing use in harsh field settings. The result was a fully functional strain sensor with a high sensitivity in excess of 5 V/ε and a linearity near 1. In addition,

cyclic four-point loading tests revealed a robust performance capable of strains in excess of 17,000 $\mu\varepsilon$ before failure of the brittle soldered IC connections to the metal stack. The sensor was also validated using a steel sub-assembly specimen loaded to failure (*i.e.,* fracture of a welded beam-column connection). In this more realistic SHM application, the sensor performed well with a sensitivity of 1.5 V/ε and linearity in excess of 0.9. The sensor did experience damage during the actual fracture event which was suspected to originate from the loosening of an electrical connection in the sensor.

While the proposed fully integrated thin film sensors performed well in laboratory testing, future improvements can be made. First, the fabrication process had a yield slightly greater than 50%; this is expected in an experimental fabrication process and would improve with additional volume and scale. An important aspect of this will be making the multifunctional material process increasingly systematic and controlled for greater control of material properties and yield in the most novel fabrication stages. Small batches of novel multifunctional materials will likely require significant testing and calibration as production ramps to large volumes. The potential variability in early batches is apparent here as the LbL process described could be improved to reduce the variations in film properties including film thicknesses and initial resistance. This is critical in the strain sensor prototyped herein because different SWNT-PSS/PVA strip resistances at zero strain result in offsets in the Wheatstone bridge limiting the amplification potential of the sensor. By ensuring uniform film properties, the bridges would be well balanced prior to amplification. Finally, the robustness of the film could be improved. In this study, the weakest component of the sensor was the soldered IC components with these soldered connections failing under high compressive strain and high shock events (as experienced in the steel sub-assembly tests). Many methods exist for mechanically and electrically bonding surface mount components to metal

traces, however best practices can be nuanced and are dependent on processing and use conditions. The process described here aimed to provide a highly general processing approach that can be easily modified and applied to a vast range of multifunctional materials and use cases. Current work is exploring alternative means of bonding IC components in addition to removing them from the sensor design all together. While opportunities remain, the above work illustrates the complete development of a multifunctional material sensing system from sensor creation through field deployment and provides a processing platform for many similar displays in numerous fields moving forward.

CHAPTER 4.

POLYMER NANOCOMPOSITE RESISTIVE ARRAYS FOR SPATIAL STRAIN SENSING

4.1 Introduction

Spatial strain sensing is a goal of the SHM community as current methods are likely to miss local damages in structures. In current point-sensing methods, such as strain gages, high-fidelity data is measured directly, however data is only obtained for a point or localized strip of structural material. The alternative that is presently used is visual inspection, which can be costly, subjective, and lead to missed local damage [2]. This challenge has motivated the creation of in situ or coated sensing materials that are interrogated with electrical impedance tomography (EIT) for spatial damage detection.

Electrical impedance tomography is a method for estimating the spatial properties of materials using the physics of the material and measurements at the boundaries of the material [88]. To perform EIT in the context of thin film conductivity, current is injected using two boundary nodes and voltage is measured at boundary nodes of the material. This process can be repeated with different current source and sink nodes to provide more information and transform the linear algebra from a system of equations that is underdetermined to one that is overdetermined. Electrical impedance tomography uses finite element methods to discretize the area of the

conductor to allow for approximation of conductivity. EIT then starts with an initial estimation for the spatial conductivity of the material, compares the resulting voltage estimate for this estimation and the known injected current to the measured voltage, and updates the guess iteratively until the process converges to a spatial conductivity with little error between the measured and estimated voltage [18]. EIT was made possible by Calderon's inverse problem [89], which created a framework for solving the ill-posed problem of reconstructing spatial conductivity. This led to efforts to advance EIT and utilize the approach for applications such as geophysics, environmental sciences, and medical imaging [90]–[92].

Significant work has applied EIT approaches to SHM applications utilizing conductive thin film or self-sensing materials. For example, Hou *et al.* used EIT of carbon nanocomposite thin films to identify regions of inhomogeneous conductivity and observe pH sensitivity [11]. Loh *et al.* used EIT with similar thin films to observe strain sensitivity and impact damage to a plate covered by the thin film material [93]. Loyola *et. al.* investigated EIT for distributed damage detection with a spray-applied thin film over glass fiber-reinforced polymer composites [72]. Tallman *et. al.* used EIT tactile imaging and distributed strain sensing in carbon nanofiber/polyurethane nanocomposites [94]. However, drawbacks such as computational demands, the need for a priori knowledge, and the subjectivity of regularization continue to prevent widespread use of EIT. This has been apparent as Tallman and Wang recently put forth a possible solution to the need for a priori knowledge and scaling issues in processing [50] and others have proposed methods based on measuring the change in resistance instead of using EIT as a less computationally intensive means to create spatial mapping and detect damage detection [95], [96]. Potential remains for improving the performance and reducing the computational complexity of EIT.

Array-based resistive sensing methods have been proposed as an alternative approach to distributed sensing. Notably, Glisic *et al.* showed arrays of conventional strain gages [36] and Takahashi *et al.* showed CNT active-matrix backplane TFT arrays on a polyimide backing for sensing pressure [97]. Both of these approaches leave issues of vulnerability to miss damage due to point sensing. There is also a scalability challenge here as the complexity of instrumentation and readout will increase with as the number of sensing elements in these arrays and likely limit the either the resolution or coverage area of such approaches. This has been apparent in numerous recent research efforts to more-effectively scale readout of resistor arrays [98]–[101]. An array-based approach of individually interrogated resistors is not a viable alternative to the distributed sensing challenge EIT seeks to address.

The goal of this study is to pattern distributed thin film resistors and interrogate these resistors with an EIT-like solver for spatial strain sensing with improved computational simplicity. We begin this effort by designing an array of distributed CNT-polymer composite resistive strain sensors. The array of CNT-polymer composite resistors is fabricated on a flexible substrate with metal electrodes using a layer-by-layer film fabrication process and lithographic patterning of the sensing films and metals. An algorithm is developed to allow for readout of the resistive array of sensors, providing a similar structural health monitoring output to that of EIT. This algorithm is based on a more direct approach than is possible with EIT and as such is less computationally intensive and does not require regularization. The algorithm is validated with off-the-shelf resistors then utilized to interrogate the fabricated polymer-nanocomposite sensing array. The technology is tested as a spatial strain sensor on a PVC bar in bending under multiple angles of sensor alignment. The design and results are discussed in the context of EIT and SHM applications.

4.2 Fabrication of Patterned CNT-Polymer Thin Film Array

4.2.1 Materials

Glass slides from Fisher Scientific are used for rigid substrates during LbL processing. Kapton polyimide films (50 micron thickness) are used as purchased from American Duarfilm (FT Kapton 200 HN). Poly (vinyl alcohol) (PVA) (fully hydrolyzed) (part number P1763) and polysodium-4-styrene sulfonate (PSS) (M_w = 1,000,000) (part number 434574) are acquired from Sigma-Aldrich. The carbon nanotubes used here are HiPCO (High Pressure Carbon Monoxide Process) purified SWNT with a diameter of 0.8-1.2 nm and length of 100-1000 nm from Nanointegris. All chemical solutions for the deposition of the SWNT composites are made using 18 MΩ deionized (DI) water. Conductive silver paste is acquired from Ted Pella (part number 16045) and miniature continuous-flex connecting wires are purchased from McMaster Carr (part number 7071K13). SPR 220-3.0 and SPR 220-7.0 photoresists from Rohm and Haas Co. are used as supplied by the Lurie Nanofabrication Facility (LNF) at the University of Michigan. AZ 726 developer from Clariant Corporation and 4 in. diameter silicon wafers (thickness 500 microns) from Silicon Valley Microelectronics are also used as supplied by the LNF. Quartz Wax (0CON-200) from Logitech is used for bonding flexible substrates to rigid backing for processing. Poly vinyl chloride bars used for testing are acquired from McMaster Carr.

4.2.2 Layer-By-Layer Film Fabrication

A layer-by-layer film fabrication process is used in constructing the sensing material. In this process oppositely charged polyelectrolyte materials are coated sequentially to gradually construct a film [51]. The first monolayer here is 1.0 *wt.*% PVA and the second is 1.0 *wt.*% PSS with 1 mg/mL of SWNTs as a conductive filler. These layers form one bilayer and this process is

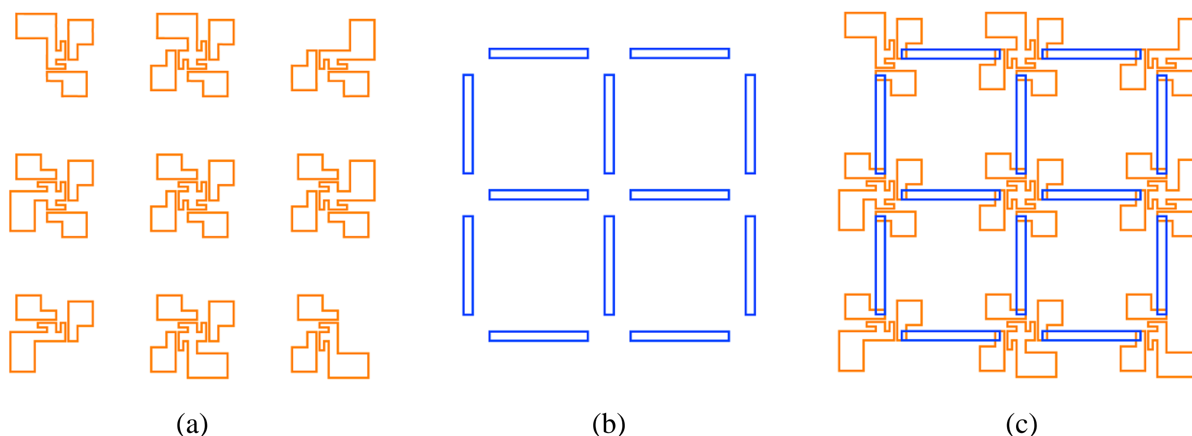

Figure 4-1. Design layout of electrodes and CNT sensing array.

repeated to sequentially construct a thin film material. The SWNTs are dispersed in PSS using ultrasonic agitation. First the solution is placed in 20 mL vials and bath sonicated for 180 minutes (135W, 42 kHz). After these solutions are tip sonicated for 30 minutes (3.178 mm tip, 150W, 22 kHz) in 100 mL jars with a five second on and five second off pulse rate. An automated machine is utilized for the dipping, rinsing, and drying of film deposition. Readers are referred to Chapters 2 and 3 for a more detailed description of this type of processing. All films are annealed at 250 C for 20 minutes after fabrication. Layer-by-layer films of 60 and 70 bilayers are used in this study.

4.2.3 Overview of System Fabrication Process

The resistive arrays are constructed using the process shown below in Figure 4-1 and the planar layout of the arrays utilized can be seen in Figure 4-2. This layout allowed for testing of individual sensors prior to connecting electrodes in the network for system testing. The process begins with a Kapton polyimide substrate. Gold pads for electrodes are patterned on the substrate using optical lithography. Here the electrodes are comprised of a 5 nm adhesion layer of chromium and a 700 nm layer of gold. The electrodes are patterned using SPR 220-3.0 photoresist spun at 3,000 rpms. A thicker layer of photoresist is used to pattern the nanocomposite film. This layer of

photoresist is SPR 220-7.0 spun at 2,000 rpms. The polyimide film is treated with poly-L-lysine prior to layer-by-layer deposition in areas that are not covered with photoresist to improve adhesion of initial layers. The layer-by-layer process is then used to sequentially build the sensing material in a controlled manner. Soaking in acetone and bath sonication are used to liftoff the photoresist and unwanted areas of layer-by-layer patterning. The films are then annealed in a convection oven to complete fabrication of the sensing arrays.

4.2.4 System Instrumentation

The array sensing systems are instrumented by connecting flexible wire to gold pads around the edges of the sensing film. Silver paste is used to provide the electrical connection between the wires and gold pads. These wires are then attached to a circuit board that provides easy access to sensing channels and this board is connected to the power supply and data acquisition systems.

4.3 Inverse Algorithm for Resistive Array

An inverse solver is needed for determining the resistor values in our resistor array in a fashion similar to electrical impedance tomography. In either conventional EIT or our approach, the conductance of a resistive material is described by the Kirchhoff matrix, **K**, for the material. The simplified geometry created here using an array of resistive distributed sensors allows for a more direct construction of **K** compared to EIT. In this section, an algorithm for determining the resistor values in our network is derived and explained.

For a resistor network with N nodes numbered $i = 1, 2, \ldots, N$, r_{ij} is the resistance of the resistor connecting nodes i and j resulting in the associated conductance

$$c_{ij} = r_{ij}^{-1} = c_{ji} \tag{4.1}$$

The net electrical potential at the i-th node can be termed V_i and the net current flowing into the network at the i-th node I_i. Kirchhoff's current law can be stated

$$\sum_{i=1}^{N} I_i = 0 \tag{4.2}$$

Alternatively, Kirchoff's current law can be written

$$\sum_{i=1, j \neq i}^{N} c_{ij}(V_i - V_j) = I_i \tag{4.3}$$

In matrix form this reads

$$\boldsymbol{K}\left[\frac{\boldsymbol{\Phi}}{\boldsymbol{V}}\right] = \left[\frac{\boldsymbol{0}}{\boldsymbol{I}}\right] \tag{4.4}$$

where $\mathbf{\Phi}$ represents the electrical potential at the inner nodes, while $\mathbf{V}$ represents the electrical potential at the boundary nodes. The Kirchhoff matrix can be written

$$\boldsymbol{K} = \begin{pmatrix} c_1 & -c_{i2} & \cdots & -c_{1N} \\ -c_{21} & c_2 & \cdots & -c_{2N} \\ \vdots & \vdots & \ddots & \vdots \\ -c_{N1} & -c_{N2} & \cdots & c_N \end{pmatrix} \tag{4.5}$$

where

$$c_i \equiv \sum_{j=1, j \neq i}^{N} c_{ij} \tag{4.6}$$

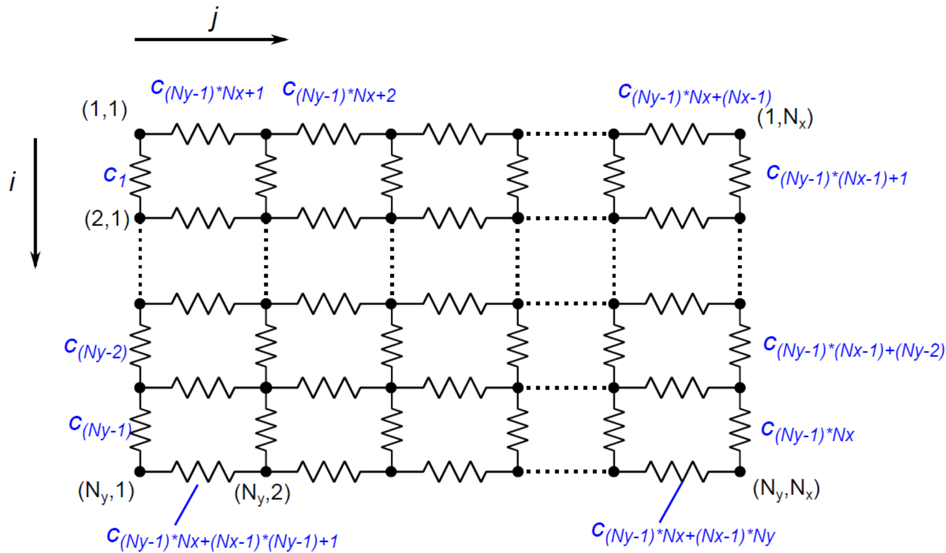

Figure 4-2. Rectangular resistor network schematic.

4.3.1 Kirchhoff Equations for Resistor Network

The process begins with the forming of Kirchhoff's equations in matrix form for the resistor network. A schematic of the network with nodes and resistors labeled is shown in Figure 4-3. Figure 4-4 shows an isolated node as one is considered conceptually for assembly of the Kirchhoff matrix. The matrix is assembled row by row using the node numbering and equations 4.7-4.10 and 4.11 respectively. This process is repeated for each row until the entire matrix has been constructed.

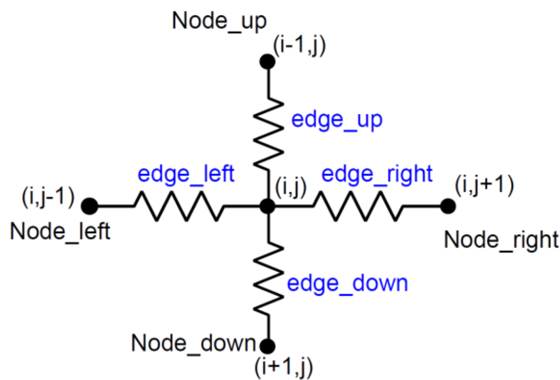

Figure 4-3. Nodal details for assembling Kirchhoff matrix.

$$\boldsymbol{K}(Node_{ij}, Node_{up}) = \text{-}c_{edge_up} \tag{4.7}$$

$$\boldsymbol{K}(Node_{ij}, Node_{down}) = \text{-}c_{edge_down} \tag{4.8}$$

$$\boldsymbol{K}(Node_{ij}, Node_{left}) = \text{-}c_{edge_left} \tag{4.9}$$

$$\boldsymbol{K}(Node_{ij}, Node_{right}) = \text{-}c_{edge_right} \tag{4.10}$$

$$\boldsymbol{K}\left(Node_{ij}, Node_{ij}\right) = c_{edge_{up}} + c_{edge_{down}} + c_{edge_{left}} + c_{edge_{right}} \tag{4.11}$$

4.3.2 Reordering of Node Numbers

Once the Kirchhoff matrix, **K**, has been constructed its rows are reordered to create, **K***, where the initial rows containing A and B correspond to boundary nodes in the system and later rows correspond to interior nodes.

$$\boldsymbol{K}^{*} = \begin{pmatrix} A & B \\ B^{T} & D \end{pmatrix} \tag{4.12}$$

4.3.3 Schur Complement of ***K****

Additionally, we will now take the Shur complement of **K***, **Γ**, for use in later steps. **V** and **I** are voltage and current at the boundary nodes respectively. To ensure a unique solution the summation of the current and voltage at all boundary nodes must equal zero.

$$\boldsymbol{\Gamma} = \mathbf{A} - \mathbf{B} * \mathbf{D}^{-1} * \mathbf{B}^{\mathrm{T}} \tag{4.13}$$

$$\boldsymbol{\Gamma}\boldsymbol{V} = \boldsymbol{I} \tag{4.14}$$

4.3.4 Moore-Penrose Pseudoinverse of $\boldsymbol{\Gamma}$

To solve for the conductivities in the array based on boundary measurements, we must find an equation where an operator with the conductivity as an input and excitation current as an input produce a voltage output estimate. That equation is shown below where **U**(s, I) is the operator.

$$\boldsymbol{U}(s, I) = \boldsymbol{R}(s)I = V \tag{4.15}$$

Ideally, **R**(s) would be found as the inverse of **Γ**, however **Γ** is singular so this is not possible. Instead, we can find **R** numerically as the Moore-Penrose pseudoinverse of **Γ**, which we will call $\boldsymbol{\Gamma}^+$.

$$\boldsymbol{R}(s) = (\boldsymbol{\Gamma}^T\boldsymbol{\Gamma})^{-1}\boldsymbol{\Gamma}^T = \boldsymbol{\Gamma}^+ \tag{4.16}$$

4.3.5 The Jacobian Matrix

To iteratively solve for conductance we will need to find

$$\left.\frac{\partial \boldsymbol{U}}{\partial s}\right|_{s=s_o} = \boldsymbol{J} \tag{4.17}$$

which is termed the Jacobian matrix. Since **U** is a function of **R**(s) and we cannot find solve for **R**(s) analytically, we will need to use the following property to rewrite the formula for the Jacobian

$$\begin{aligned} \boldsymbol{J} = \left.\frac{\partial \boldsymbol{U}}{\partial s_n}\right|_{s=s_o,I=I_o} &= \left.\frac{\partial \boldsymbol{\Gamma}^+ I}{\partial s_n}\right|_{s=s_o,I=I_o} \\ = \left.(-\boldsymbol{\Gamma}^+\frac{\partial \boldsymbol{\Gamma}}{\partial s_n}\boldsymbol{\Gamma}^+\boldsymbol{I})\right|_{s=s_o,I=I_o} &= \left.(-\boldsymbol{\Gamma}^+\frac{\partial \boldsymbol{\Gamma}}{\partial s_n}\boldsymbol{V})\right|_{s=s_o,I=I_o} \end{aligned} \tag{4.18}$$

4.3.6 Determine the Partial Derivative of $\boldsymbol{\Gamma}$

With this formulation, we now only need the analytical solution to $\partial\Gamma/\partial s_n$ and can instead compute the numerical solution to $\boldsymbol{\Gamma}^+$. To compute the partial derivatives of **Γ** we will use the following equation:

$$\frac{\partial \boldsymbol{\Gamma}}{\partial s_n} = \frac{\partial A}{\partial s_n} - \frac{\partial (BD^{-1})}{\partial s_n} B^T - BD^{-1} \frac{\partial (B^T)}{\partial s_n}$$

$$= \frac{\partial A}{\partial s_n} - \left[\frac{\partial A}{\partial s_n} D^{-1} - BD^{-1} \frac{\partial (D)}{\partial s_n} D^{-1} \right] B^T - BD^{-1} \left(\frac{\partial B}{\partial s_n} \right)^T \tag{4.19}$$

$$= \frac{\partial A}{\partial s_n} - \frac{\partial A}{\partial s_n} D^{-1} B^T + BD^{-1} \frac{\partial (D)}{\partial s_n} D^{-1} B^T - BD^{-1} \left(\frac{\partial B}{\partial s_n} \right)^T$$

With the final equation above for the partial derivative of $\boldsymbol{\Gamma}$ we have a form that we can evaluate. The partial derivatives of A, B, and D are found analytically and assessed for $s = s_o$. B^{-1} and D^{-1} are assessed numerically for $s = s_o$. The partial derivative of $\boldsymbol{\Gamma}^+$ for each component of s can then be computed with the equation below.

$$\left. \frac{\partial \boldsymbol{\Gamma}^+}{\partial s_n} \right|_{s=s_o} = \left. \left(-\boldsymbol{\Gamma}^+ \frac{\partial \boldsymbol{\Gamma}}{\partial s_n} \boldsymbol{\Gamma}^+ \right) \right|_{s=s_o} \tag{4.20}$$

Note that this step is very computationally intensive, currently limiting our implementation to square arrays with less than seven elements on each side.

4.3.7 Linear Approximation and the Jacobian

We now have everything needed to assess the partial derivative of $\boldsymbol{\Gamma}^+$ and find the Jacobian. With the Jacobian, we can solve the system with the inverse solution using the direct method

$$\delta s = \boldsymbol{J}^+ \delta V = (\mathbf{J}^T \mathbf{J})^{-1} \mathbf{J}^T \delta V \tag{4.21}$$

and the inverse solution using the iterative method

$$s_{i+1} = s_{i+1} + \alpha \delta s_i \tag{4.22}$$

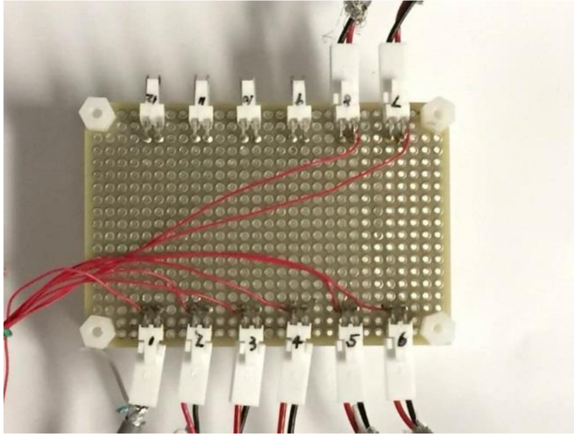

(a)

(b)

Figure 4-4. Custom circuit board and terminal block utilized for data acquisition.

where α is the step size chosen for each iteration.

$$\delta s_i = \boldsymbol{J}_i^{+}\delta V = (\mathbf{J}^T\mathbf{J})^{-1}(\mathbf{J}^T(V - U(s_i))) \quad (4.23)$$

Note that in this approach regularization is not needed as it is in FEM based EIT.

4.4 Experimental Testing

4.4.1 Data Acquisition for Resistive Array

Current is supplied between two boundary nodes and voltage is measured across boundary nodes to collect data from the resistive array. Current is supplied with a Keithley 6221 current source. Voltage is measured using a NI TB-2706 terminal block on a NI PXIe-1082 PXI chassis that is controlled with LabVIEW software. A custom circuit board is connected to the power supply and NI system and flexible wiring is run from this board to the thin film nodes. The circuit board and voltage data acquisition system utilized can be seen in Figure 4-5.

4.4.2 Validation of Resistive Array Algorithm for Thin Film System

The algorithm for determining resistance values for the resistive array is validated using off-the-shelf, through-hole resistors in a three-by-three network of 24 total resistors. This process began by fabricating an array of resistors on a circuit board as shown below in Figure 4-6b and with the numbering of resistors shown in Figure 4-6a. Measurements of all resistors are taken prior to array assembly and the true resistances are compared to the findings of the algorithm. The network is then altered by replacing a resistor with one of significantly higher conductance as shown in Figure 4-6c. The resolution of the algorithm is quantified using on the experimental conditions that will be used in testing the array of thin film resistive sensors.

Initial validation with resistors is followed by validation with resistive polymer nanocomposite thin film materials in a two-by-two network of 12 total sensors. The electrical connections within the network were designed with gaps so that initially the true resistance of each sensor could be measured using a digital multimeter. These gaps between electrodes were bridged with silver paste to complete the electrical connections within the resistive array for algorithm and system testing. The wired film ready for testing of individual resistors can be seen in Figure 4-7a

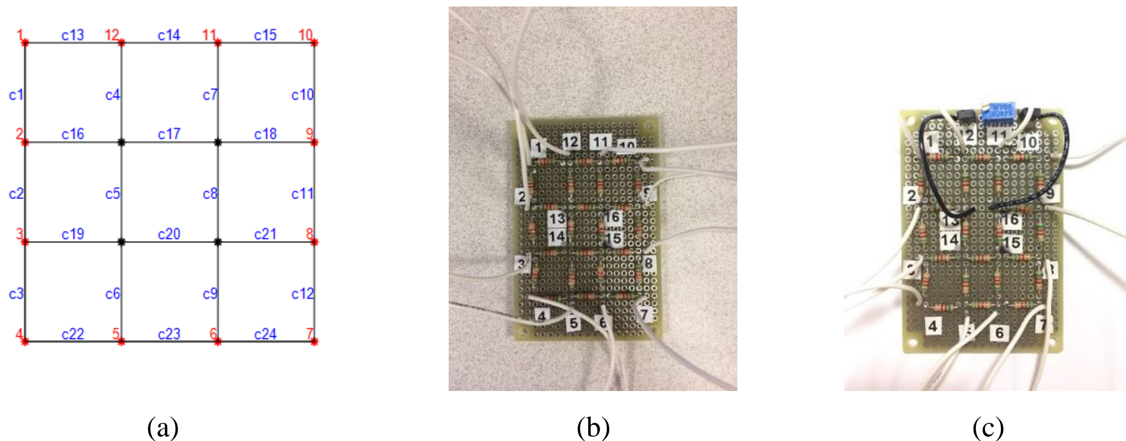

(a) (b) (c)

Figure 4-5. Resistor network tested for algorithm validation.

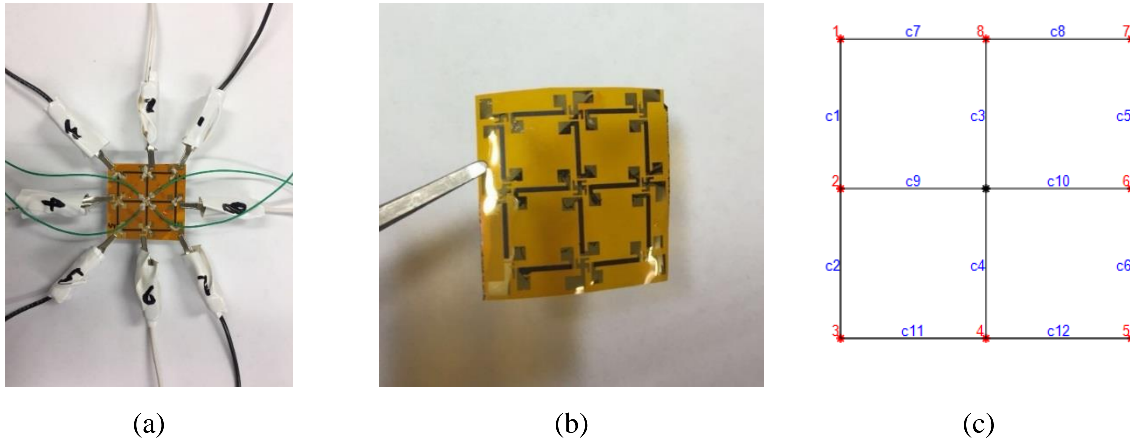

(a) (b) (c)

Figure 4-6. Photos of (a) fabricated sensing grid with wires connected for measuring resistance prior to bridging electrodes, (b) standalone sensing skin prior to testing, and (c) schematic of numbering of sensors and nodes.

and the standalone film prior to instrumentation can be seen in Figure 4-7b. The numbering system used for the thin film sensors can be seen in Figure 4-7c. Findings from the system measurements and algorithm are observed prior to mechanically testing the thin film system.

4.4.3 Illustration of Resistive Array in SHM Application

The resistive thin film array and corresponding algorithm are tested under stain to illustrate their potential for uses in structural health monitoring. Thin film sensors are bonded to PVC bars as shown in Figure 4-8. The PVC bars are then loaded in four-point bending to apply uniform

(a) (b)

Figure 4-7. Film sensors bonded to PVC bars at the angles of (a) 0° and (b) 45° for mechanical testing.

strain across the array. The effectiveness of network elements in strain sensing is illustrated using two different orientations of the sensor array relative the direction of strain. First, a sensing array is bonded so that half of the sensors are aligned with the PVC bar, and thus the primary strain direction, and half are aligned perpendicularly. Perpendicular sensors in the network are subjected to little strain as shown in Figure 4-8a. Next, a sensing array is bonded at an angle of 45° to the PVC bar so that all sensors see similar strain throughout loading as shown in Figure 4-8b. The DAQ approach and algorithm described previously are utilized to collect data and estimate the resistance of array elements at each load step.

4.5 Results and Discussion

4.5.1 Validation of Resistive Array EIT Algorithm

The results from utilizing the algorithm to determine the resistor values in the validation network are shown below in Figure 4-9 and Table 1. Table 1 shows that resistance estimates were nearly all within 2% error regardless of injection pattern utilized during data acquisition and processing for a resistor network where all resistances were around 5 kOhms. Figure 4-9 shows the true and estimated conductance of each element in the resistor network graphically. This figure

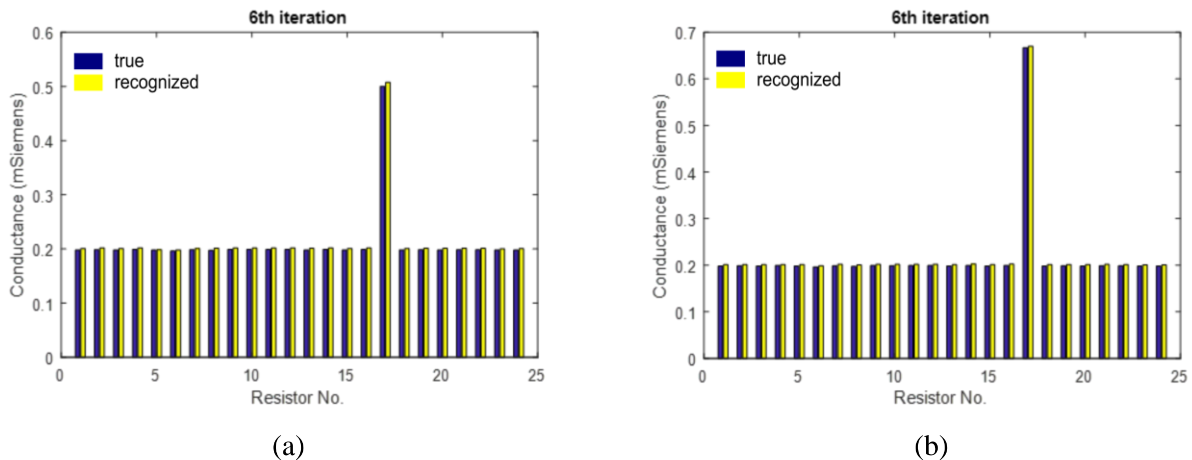

(a) (b)

Figure 4-8. True values and algorithm estimates of conductance values in two resistor networks.

Table 1: Recognized conductances in the resistor network subjected to various injection patterns of current.

component	resistance	conductance	adjacent		across		diagonal	
	r (KΩ)	s (mΩ^{-1})	s	error	s	error	s	error
c1	5.0500	0.1980	0.2006	1.3%	0.2009	1.5%	0.2009	1.5%
c2	5.0340	0.1986	0.2022	1.8%	0.2016	1.5%	0.2013	1.3%
c3	5.0505	0.1980	0.2013	1.6%	0.2009	1.4%	0.2009	1.4%
c4	5.0192	0.1992	0.2018	1.3%	0.2023	1.5%	0.2018	1.3%
c5	5.0535	0.1979	0.2004	1.3%	0.2006	1.4%	0.2014	1.8%
c6	5.0979	0.1962	0.1993	1.6%	0.1990	1.4%	0.1987	1.3%
c7	5.0350	0.1986	0.2013	1.4%	0.2012	1.3%	0.2011	1.2%
c8	5.0692	0.1973	0.2002	1.5%	0.1994	1.1%	0.2009	1.9%
c9	5.0224	0.1991	0.2018	1.4%	0.2018	1.3%	0.2015	1.2%
c10	5.0288	0.1989	0.2016	1.4%	0.2018	1.5%	0.2018	1.5%
c11	5.0236	0.1991	0.2017	1.3%	0.2022	1.6%	0.2018	1.4%
c12	5.0208	0.1992	0.2019	1.4%	0.2022	1.5%	0.2021	1.5%
c13	5.0468	0.1981	0.2008	1.4%	0.2012	1.6%	0.2010	1.5%
c14	5.0207	0.1992	0.2019	1.3%	0.2019	1.3%	0.2019	1.4%
c15	5.0461	0.1982	0.2009	1.4%	0.2009	1.4%	0.2010	1.4%
c16	5.0222	0.1991	0.2021	1.5%	0.2025	1.7%	0.2017	1.3%
c17	5.0386	0.1985	0.2014	1.5%	0.2030	2.3%	0.2021	1.8%
c18	5.0472	0.1981	0.2006	1.2%	0.2011	1.5%	0.2007	1.3%
c19	5.0357	0.1986	0.2012	1.3%	0.2011	1.3%	0.2013	1.3%
c20	5.0509	0.1980	0.2007	1.4%	0.2022	2.1%	0.2009	1.4%
c21	5.0345	0.1986	0.2013	1.4%	0.2012	1.3%	0.2013	1.3%
c22	5.0422	0.1983	0.2008	1.2%	0.2014	1.5%	0.2012	1.5%
c23	5.0536	0.1979	0.2004	1.3%	0.2006	1.4%	0.2007	1.4%
c24	5.0517	0.1980	0.2006	1.3%	0.2008	1.4%	0.2008	1.5%

Table 4-1 Recognized conductance in the resistor network subjected to various current injection patterns.

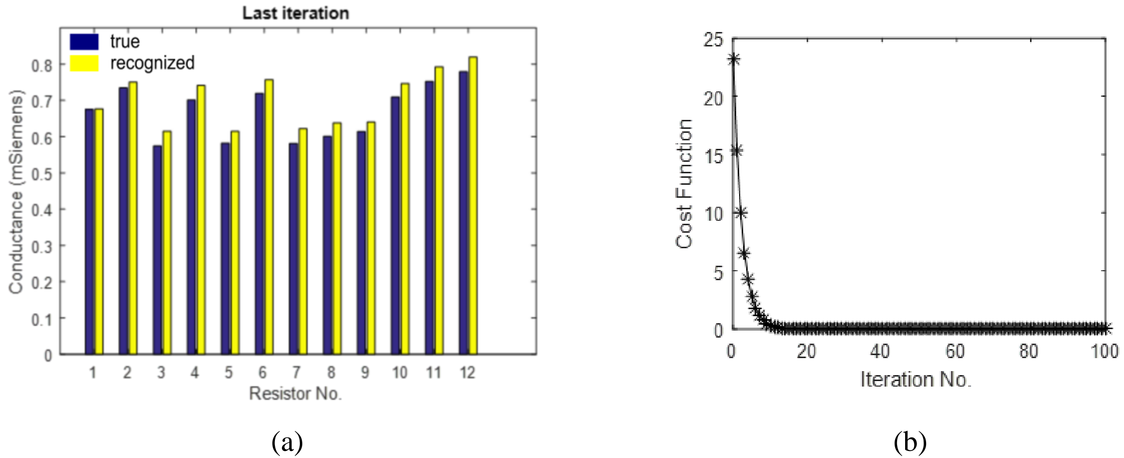

(a) (b)

Figure 4-9. True values and algorithm estimates of 60 bilayer nanocomposite sensor array.

displays the robustness of the algorithm to sharp changes in resistance as the conductance of one element was changed to 0.67 mSiemens and the algorithm was able to estimate this resistance with similar errors to those shown previously. The two-by-two sensor network took around 30 seconds for 30 iterations on a while the three-by-three resistor network took a few minutes for 30 iterations on a desktop computer. This illustrated that the inverse algorithm for determining resistances in arrays functioned effectively as designed as cleared the path for use with thin film sensing elements.

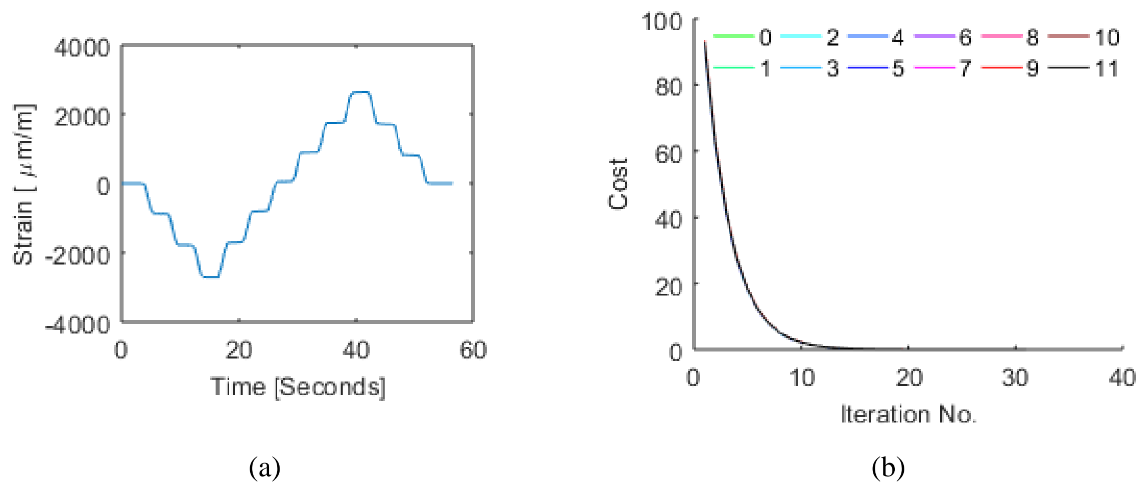

(a) (b)

Figure 4-10. Testing loading procedure (a) and cost function on each loading step (in legend) (b) for sensor at 0° to strain direction.

4.5.2 Illustration of Resistive Array in SHM Application

The array with sensors aligned at 0° to the direction of applied strain were tested first. Figure 4-10 compares the resistances of the network as measured by a digital multimeter prior to connecting elements with values estimated by the algorithm after all elements of the network were connected. The cost function of the algorithm in determining these resistances as the solver iterated can be seen in Figure 4-10b. Figure 4-11 shows the loading procedure along with the consistent behavior of the cost function of the solver after all loading steps (overlapping in figure). The conductance of each of the sensors aligned in the direction of strain can be seen in Figure 4-12 where it is apparent that all sensors are tracking strain. The conductance of each of the sensors aligned in the direction perpendicular to the strain direction are shown in Figure 4-13. These sensors are not trending with strain, which matches expectations and confirms the functionality of the strain sensing array. The gage factors of these sensors defined as the change in resistance over initial resistance normalized by strain is around 2.5, although some variation is present between different sensors. It is worth noting here that the final step of this loading process was discarded due to significant network changes and error thought to result from a change in the data acquisition setup. This illustrated an additional strength of the algorithm as the inconsistent data from the test was indicated with a much higher cost function than all other array estimations conducted prior to observation of the results. This indicates the potential to automatically identify bad data to avoid misinterpretation of irregular data sets.

The array of sensors angled at 45° to the loading direction were tested with the loading procedure in Figure 4-14a resulting in the cost functions shown in Figure 4-14b. Cost functions were consistent throughout testing. The resulting sensor conductivities at various loading points for sensors 1-6 are shown in Figure 4-15 and 7-12 are shown in Figure 4-16. Here, all twelve

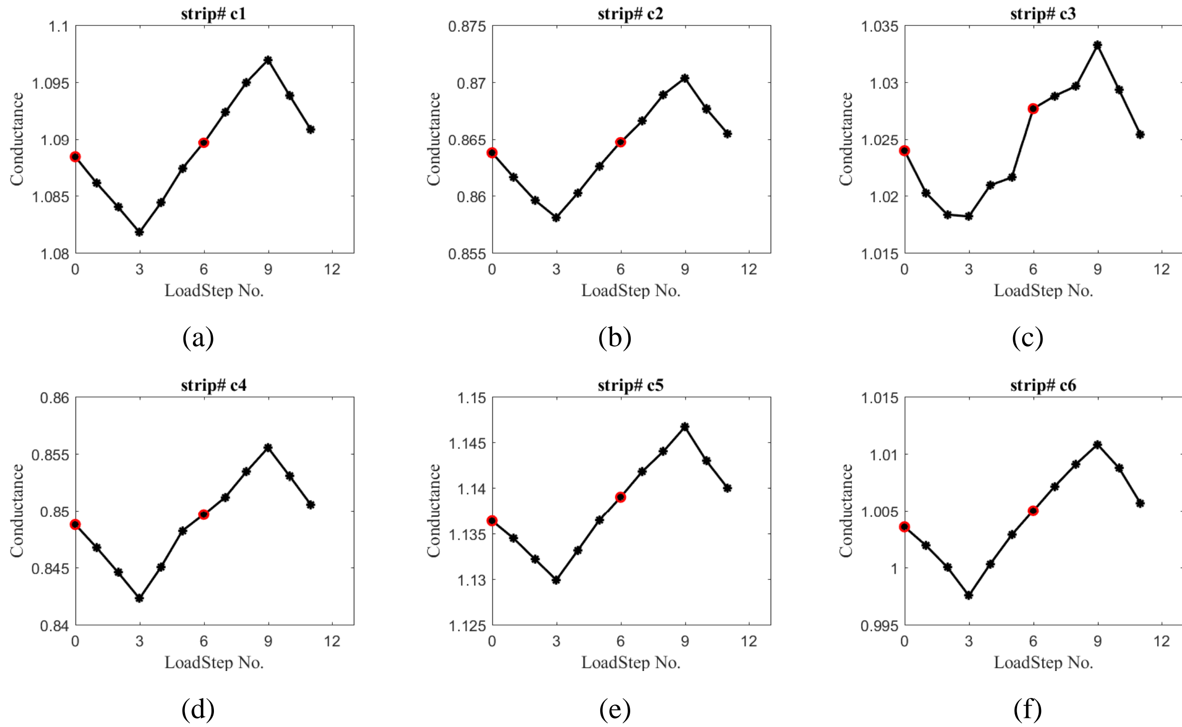

Figure 4-11. Conductance response of array sensors aligned on the x-axis along strain direction during 0° test.

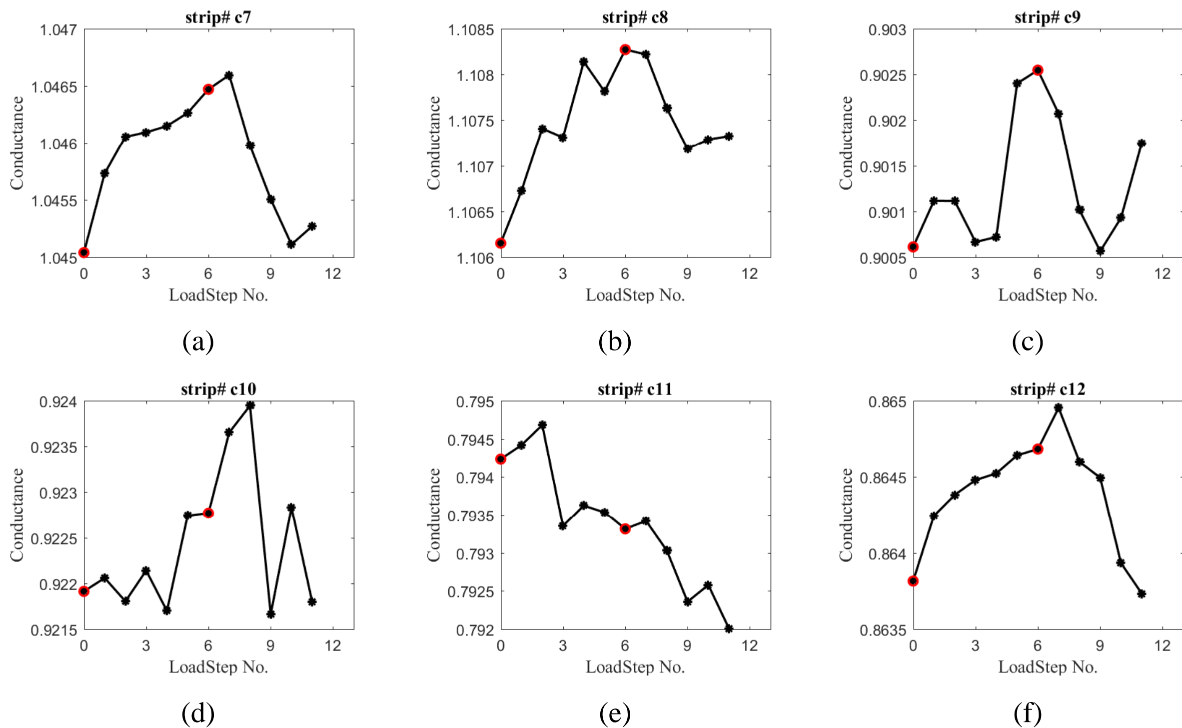

Figure 4-12. Conductance response of array sensors aligned on rotated the y-axis during 0° test.

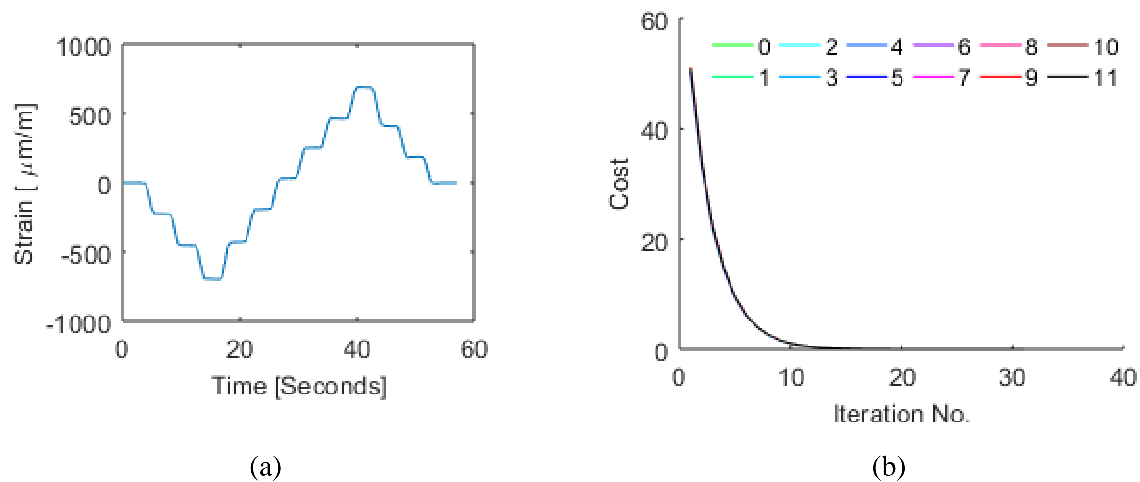

(a) (b)

Figure 4-13. Testing loading procedure (a) and cost function on each loading step (in legend) (b) for sensor at 45° to strain direction.

sensors trended with strain as expected as all were now aligned similarly relative to the loading axis. In this test, a most sensors drifted relative to their initial resistance at zero strain. The cause for this was unknown and will be investigated in future work.

The experimentation conducted fully validates the proposed approach to spatial strain sensing including the proposed materials and algorithm. The materials utilized are effective for the design of conformable, distributed sensors in various geometries, presenting the opportunities for use in many SHM settings as well as other applications. The algorithm was shown to require relatively little computational effort and no regularization as intended. The most important current limitation to this approach is scaling, as the processing needed to obtain the numerical inverse while solving for network conductivities becomes prohibitively large when this approach is scaled up to significantly larger networks. Additionally, drift behaviors in the experimental results tested here could cause problems in applications and likely require additional system design or material research prior to use in practice.

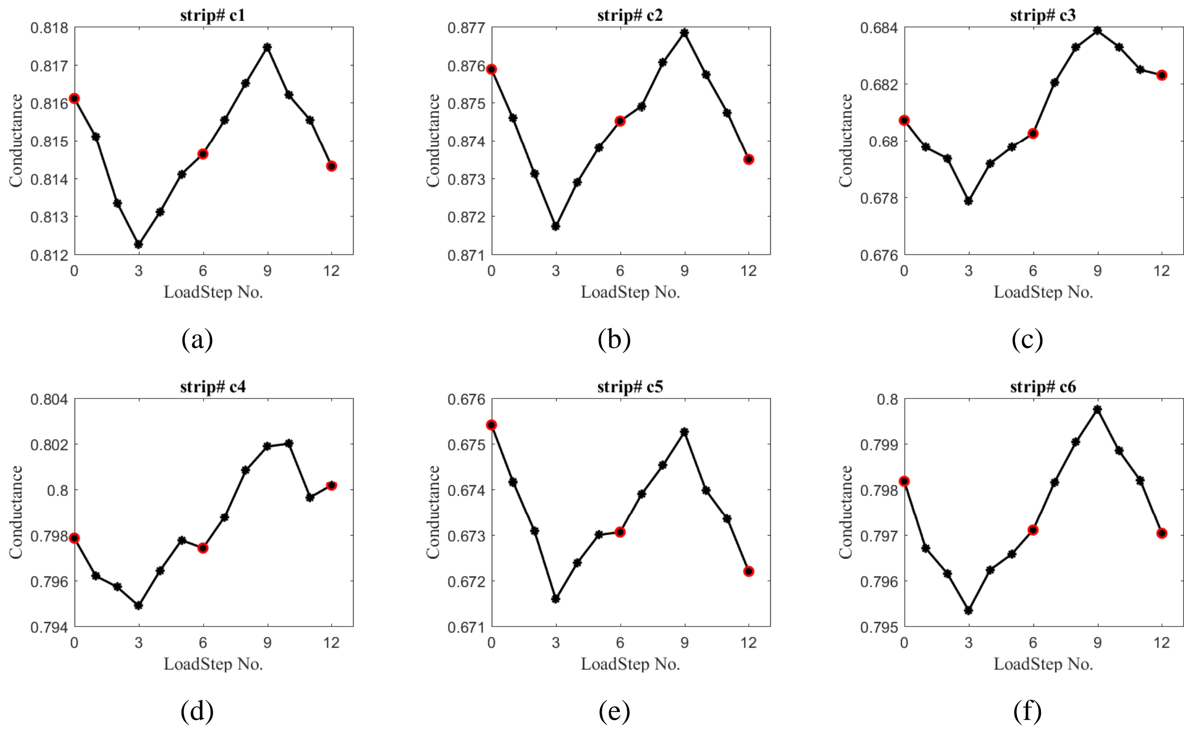

Figure 4-14. Conductance response of sensors aligned on rotated x-axis during 45° test.

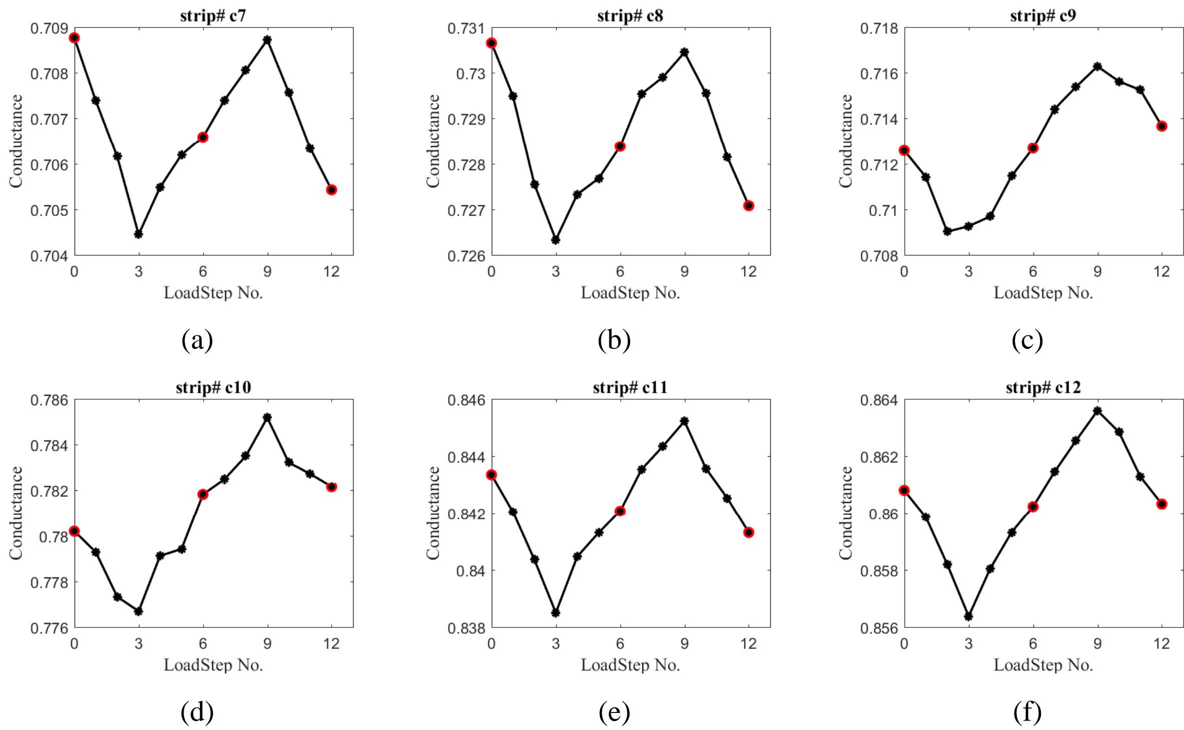

Figure 4-15. Conductance response of sensors aligned on rotated y-axis during 45° test.

4.6 Chapter Summary

Better methods are needed for determining the values of resistive sensors from the boundaries of an electrically connected network. Here, an alternative approach to EIT is proposed. In this approach, fabrication capabilities and a custom algorithm are used to create a network of spatial strain sensors with performance benefits relative to EIT. This approach begins with a fabrication process for creating an array of polymer nanocomposite resistive sensing elements with layer-by-layer thin film fabrication and optical lithography processes. Next, an algorithm is proposed and implemented for determining the conductivities of resistors in these arrays. The efficacy of the algorithm is validated using off-the-shelf resistors. This validation illustrated both the basic functionality of the approach as well as important benefits including the absence of regularization and ability to observe sharp conductivity changes, which can cause subjectivity or failure to converge in EIT.

The algorithm and film are utilized for an example SHM application by bonding films to PVC bars and testing these bars in bending. A film with six resistive elements aligned in the direction of strain is shown to have these track strain effectively while six elements aligned perpendicularly to not experience strain did not show similar trends. The gage factor of these sensors tested was around 2.5. In contrast, a second film was aligned at a 45° angle to the strain direction so that all elements were subjected to the same strain values. All elements were observed to trend with strain as expected under this alignment, although at these lower strain values drifting of many sensors showed a potential issue for applications.

The spatial strain sensing approach proposed here provides an exciting alternative to current methods. The most urgent consideration for future work is scalability, which can be

investigated through alternative methods for finding the critical matrix inverse of the algorithm or potentially utilizing patterning of the physical system to simplify the processing needed with other solvers. Additionally, work is warranted on the material side for understanding the drift of these and similar films and then eliminating that drift through either material design and fabrication of post-processing of data acquired from such materials.

CHAPTER 5.

FUSED RFID STRAIN SENSOR FOR STRUCTURAL HEALTH MONITORING

5.1 Introduction

Osseointegrated prosthetics are those in which a titanium rod is implanted into the remaining bone at a lost limb of an amputee. This procedure is under use with increasing frequency as it has benefits for amputees such as additional sensory feedback and control with an osseointegrated prosthetic relative to one strapped to the missing limb [102], [103]. However, complications can occur as an osseonitegrated implants heals and is utilized such as inadequate bone growth in healing, tissue infection, and bone fractures. Improved quantitative information in the hands of doctors and other health care practitioners could greatly enhance capabilities for early detection and treatment of osseointegrated complications. A potential route for monitoring osseointegrated implants is the use of *in vivo* sensing through wireless sensing technologies as Burny *et al.* put forth more than fifteen years ago in a comprehensive work on smart othepedic implants at the time [37]. More recently, Korduba *et al.* provided an overview on the state of RFID-based sensing in orthopedic implants as feasible but necessitating careful design in the robustness of sensors and communication methods utilized [38]. Others have approached the challenge through a number of specific proposed technologies [62]–[64]. However, the use of such *in vivo* sensing remains limited as improved design of robust systems with viable readout is needed.

Sensing for osseointegrated prosthetics is a specific application within the broader field of structural health monitoring (SHM). SHM is more commonly considered in the context of critical large-scale infrastructure, however many sensing concepts and design challenges in larger-scale structural sensing overlap with design needs for monitoring of osseointegrated prosthetics [54]. Flexible and conformable sensors are a class of SHM technologies that are useful in many environments potentially including osseointegrated prosthetics. One reason for this is conformable sensors are installable in a vast range of environments since they can adhere to rough and irregular surfaces. Conformable thin film sensors provide robustness in environments with mechanical loading as they deform with the materials on which they are install in a malleable manner and are not prone to brittle failures of rigid systems and components.

The limited space and accesses to sensing materials encountered in *in vivo* sensing are also challenges in other SHM settings. These use environments likely require passive, wireless sensor technologies for instrumentation and monitoring. This is obvious in biologically implantable sensors, which cannot be accessed with wires and must be interrogated wirelessly from outside of the body. Another example is in an interior structural component that needs to be encased in a wall or protective coating. In any such scenario, wireless sensor interrogation and passive sensor functionality are great design benefits. Researchers have developed sensors aimed at achieving this goal. Thin film sensors can be passive sensors, alleviating the complexity and limitations of providing power to the sensing device. For example, many of the previous efforts cited in monitoring orthopedic implants for functionality or healing were wireless [38], [62]–[64]. Others have investigated various methods for wireless strain sensing and crack detection in more conventional structural health monitoring settings [65], [104]–[108]. The interest displayed here

in passive, wireless, TF sensing capabilities is well-warranted; however, work remains to develop systems that can be installed, interrogated, and maintained in realistic application environments.

The need for simple and actionable wireless sensors has led to the use of sensing systems with an element designed to fail that will herein be identified as a fuse. In such systems, one aspect of the sensors fails to indicate a damage state in the structure or material on which the sensor sits. One such study by Wood and Neikirk illustrated wireless sensing with two RFID circuits, one of which was a reference and the other a sensor [109]. Similarly, Zhang and Bai proposed a "breakage-triggered" sensor where an acrylic bar was used as a brittle fuse breaking an RFID circuit [110]. However, these studies utilized large and bulky sensing and transmission materials that are not applicable to many SHM environments. Instead, a system based entirely on conformable, thin film materials would provide the versatility, durability, and limited profile for use in far more sensing environments.

The goal of this study is to develop a biocompatible, wireless, passive, fused threshold strain sensor that illustrates the viability of a thin film approach to such technologies and the potential for utilizing metal thin films as a mechanical-electrical design component. The design and construction of this wireless strain threshold sensing system displays the functionality and versatility of such an approach. This is achieved by first designing thin film inductors and capacitors with desired mechanical and electrical properties. Metal thin films are designed to act as a fuse failing at certain strain thresholds. These could provide the critical sensing insight in many SHM systems. The designed components are then integrated into a robust and elegant system design, which is tested to show system functionality. The results are discussed in the context of thin film sensing technologies and applications.

5.2 Design and Fabrication

This study illustrates a robust and broadly useful sensor that can be utilized in many application environments. With this motivation we take a thin film approach to sensor fabrication for robustness and utilization in strain sensing applications. More specifically here, we develop an implantable sensor for use in osseointegrated prosthetics. However, we expand our design considerations and the benefits of our approach to various structural health monitoring applications. These goals require a wireless sensor that is implantable, robust, can conform to rough or irregular surfaces, and can be readout at relatively low RFID frequencies. With this objective, we first design inductor and capacitor components for communication and strain sensing, respectively. We then design metal "fuses" for strain threshold detection as we feel this approach greatly simplifies readout and provides critical, actionable information in many strain sensing scenarios. Finally, we integrate the various components in a system design for the creation of our final strain sensor.

5.2.1 Thin Film LCR Components

Thin film inductor and capacitor components are designed as bioimplantable components of an RLC system. The capacitor utilized here is as a square parallel plate capacitor. The capacitor is designed with a polyimide substrate, gold metal layers, and a polyimide dielectric layer. These materials are biocompatible and robust to harsh thermal environments, chemical environments, and mechanical loading. The capacitor is designed using the side lengths of the square geometry and thickness of the polyimide dielectric layer of the capacitor. The capacitance for a parallel plate capacitor can be seen below in equation 5.1. The thickness of the dielectric layer of the capacitor changes as strain is applied in the plane of the parallel plates due to Poisson's effect as seen below

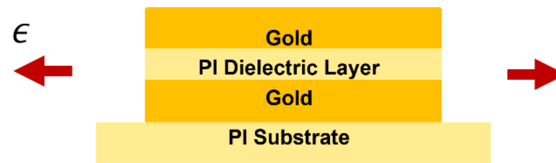

Figure 5-1. Illustration of capacitor strain sensitivity.

in Figure 5-1 and equation 5.2. This allows the capacitor here to be utilized as a strain sensor in our final system design.

$$C = \frac{A\varepsilon}{d} \tag{5.1}$$

$$\Delta d = f(\vartheta) \rightarrow \Delta d = f(strain) \tag{5.2}$$

A schematic of the capacitor fabrication process can be seen below in Figure 5-2. Capacitor fabrication begins with a polyimide flexible substrate (American Duarfilm part number: FT Kapton 200 HN). The substrates are bonded to a rigid silicon wafer to allow for handling during processing using quartz wax (Logitech part number: 0CON-200). Once substrates are bonded, a layer of gold is patterned as the bottom plate and electrode of the capacitor using optical lithography. Optical lithography is the well-established process of spinning a polymer sacrificial layer, exposing areas of the polymer layer to light through a stencil-like mask, and developing the photoresist layer or removing the areas of the layer that have been exposed to light with solution. In this study, optical lithography processes were completed in the Lurie Nanofabrication Facility at the University of Michigan. After the initial metal layer was deposited, a polyimide dielectric

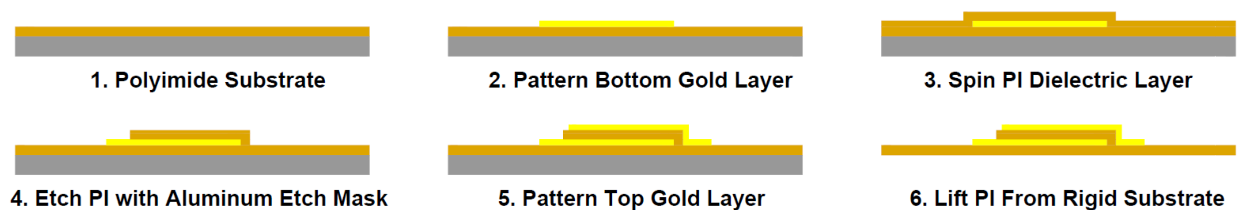

Figure 5-2. Fabrication process flow of capacitor.

layer was spun on the substrate. Here, HD Microsystems PI 2525 polyimide is used for the dielectric layer. The polyimide for the initial capacitors is spun at 5,000 rpms and the polyimide layer is soft baked until firm at 90° Celsius. The polyimide is then fully cured in a vacuum oven by ramping from room temperature to 350° Celsius and holding for one hour before cooling gradually back to room temperature. Polyimide curing is completed in a nitrogen gas environment. The polyimide was then etched to pattern the dielectric layers and remove the polyimide covering electrodes connected to the bottom plates of capacitors. This was completed with reactive ion etching in a Plasmatherm 790 in the Lurie Nanofabrication Facility. The polyimide etch was patterned using Kapton tape. Finally, the top electrode of the capacitors was deposited as a gold layer completing the capacitor fabrication process. Here, a chrome adhesion layer of around 5 nm and a gold layer of 700 nm were utilized in all metal layers. Following the fabrication process, the capacitors were lifted from the rigid backing substrate for bonding to structural testing materials.

The inductor is designed for optimized interrogation capabilities without strain sensitivity. This required maximizing the inductance and minimizing the resistance of the inductor or maximizing the quality factor. Geometry played an important role in doing this. A single-layer, square coil antenna was selected to avoid strain sensitivity and maximize geometry utilized. The

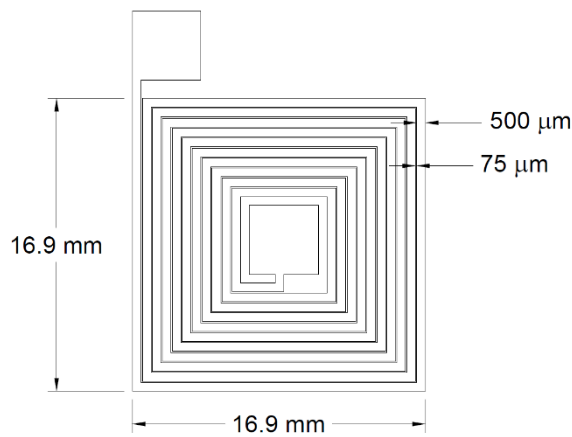

Figure 5-3. Planar design of square coil inductor.

number of turns, spacing between electrodes, and electrode widths were optimized to maximize quality factor. However, the thickness of the thin film inductor was found to be critical in achieving a high quality factor even with optimized planar geometry. The planar design of the final coil utilized can be seen below in Figure 5-3.

$$Q = \frac{\omega L}{r} \tag{1}$$

The fabrication flow for the inductor can be seen in Figure 5-4. Methods such as electroplating were explored to achieve a thick metal layer, however these had a quality factor that was too low to produce LC circuits with sharp resonant frequency peaks as desired in the final system design. Additionally, as the limits on electroplating are approached it can be difficult to achieve a uniform layer and stress issues can arise. Instead, polyimide with a thick layer of copper cladding on both sides of the film was procured from DuPont (Pyralux – AP9111R) as shown in step one of the fabrication process. This material had 35 microns of copper sandwiched between 25.4 microns of polyimide. A layer of photoresist is patterned as an etch stop and the copper is etched into the planar shape of the inductor. The copper on the backside of the film is also etched off during this step of the process. The photoresist is stripped from the inductor copper following this fabrication step. A thick copper film was fabricated with this approach for a high inductor quality factor. The inductor was then encased in polyimide using a process like that described previously for the

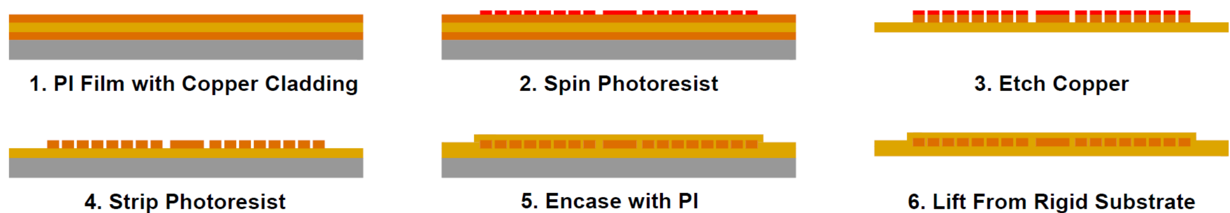

Figure 5-4. Fabrication process flow for the copper thin film inductor.

dielectric layer of the capacitor. The only difference here is that a thicker polyimide layer was needed to coat the inductor than was used as a dielectric layer for the capacitor. To achieve this thickness, two layers of HD Microsystems PI 2525 polyimide are spun over the inductor. The existing inductor and polyimide layers are cleaned prior to spinning the initial polyimide encasing layer using an Argon plasma etch. Each layer of polyimide is spun at 2,000 rpms for a target thickness of 13 microns each. Each layer is soft baked until firm at 90°C and the final film is cured fully in the manner previously described. Following this, the inductor is lifted from the rigid substrate for testing.

5.2.2 Fused Sensors for Strain Sensing

The sensing approach illustrated here is one in which a fuse, which changes electrically due to mechanical failure, illustrates a critical threshold state in the monitored material. This approach is selected as it can readily provide valuable structural information to stakeholders with a sensor that is easy to interrogate and a signal that is easy to interpret. We seek to utilize metal films for the fused element to give the sensors the durability for handling and installation, while allowing for design of fuse failure. Additionally, metal fuses are easily incorporated in electrical thin film designs as there are likely already metal electrodes in the system. An ideal fuse would have a low initial resistance prior to mechanical loading. This resistance would remain low under strain until a strain threshold, then dramatically increase at that strain threshold. Additionally, a good design would exhibit this behavior consistently. Titanium is selected as a fuse material as it

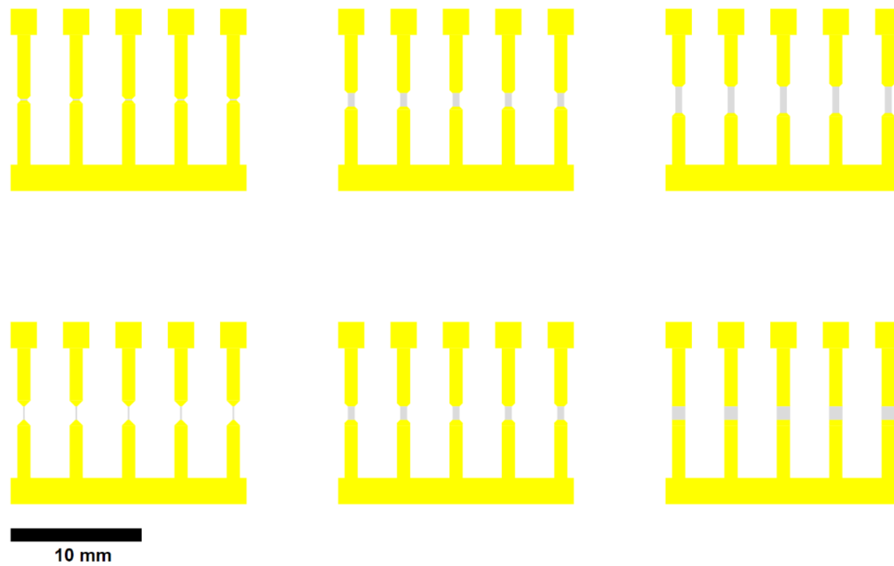

Figure 5-5. Fuses tested for use in empirical design.

is a metal layer with low resistance, can be used as an adhesion layer underneath an otherwise robust electrode, and is less ductile than many other metals. We investigate the impact of film thickness, width, length, and deposition method as four potential design variables in the creation of metal fuses. The planar layout of an array of fuse shapes tested can be seen in Figure 5-5.

The fabrication process for the metal fuses can be seen in Figure 5-6. The fuses are fabricated as a lithographically patterned metal electrode with the caveat that the adhesion layer in the metal disposition process is isolated over a controlled area using a metal etch to act as the fuse point. This is achieved by starting with a polyimide substrate then patterning a metal layer on that substrate with optical lithography. However, during metal deposition we alter the titanium film that would normally be a thin adhesion layer for use as a fuse. The titanium film is made unusually

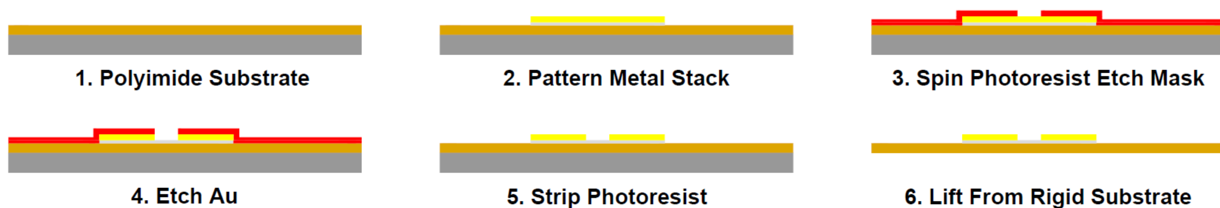

Figure 5-6. Fuse fabrication process flow.

thick to lower the resistance of the titanium layer alone. Once the gold film is patterned with this titanium layer, a photoresist mask is spun for an etch stop so that gold can be etched from only the fuse portion of the metal electrode. The gold is then etched to isolate the titanium layer. The process is concluded by removing the photoresist and lifting the film from its rigid substrate.

5.2.3 Wireless Strain Threshold Sensing System

The above components are utilized to create a wireless strain sensing system. This system is designed as two circuits that have an inductor and capacitor such that a read inductor can be used to interrogate the resonant peaks of the two thin film circuits. One of these peaks is used as a reference peak that is always present to show that the sensor and readout is functional. This peak can additionally be utilized for strain sensing by monitoring the changes in the resonant frequency of the circuit due to changes in the capacitance of the strain sensitive capacitor. A fuse that is designed to fail once a threshold strain is reached is integrated into the other inductor-capacitor

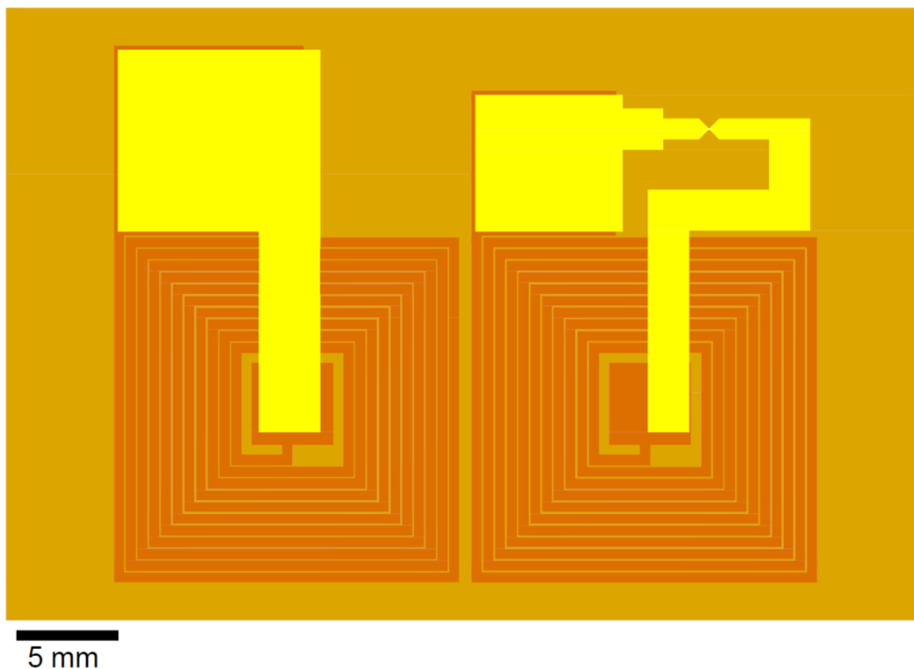

Figure 5-7. System layout for wireless threshold strain sensor.

circuit to allow for structural damage sensing. While this sensor embodies broad concepts for wireless thin film sensing, it is also laid out in consideration of a specific use for osseointegrated prosthetics. One challenge in the healing process after surgical implant of an osseointegrated titanium rod is a lack of information on the rate of bond growth as bone heals around an implant. A sensor similar to the proposed design could be affixed around the healing bone after surgery. The sensor would then be loaded in tensile strain as the bone grows until the fuse breaks at a pre-specified hoop strain. This hoop strain would be designed to correspond to bone growth necessary prior to loading the implant. This provides an important quantitative metric that would replace the current practice of conservatively guessing about adequate bone growth without quantitative information. The planar layout of this sensing system can be seen in Figure 5-7.

The fabrication process flow integrates the previously discussed components and associated processes and can be seen below in Figure 5-8. The process begins with polyimide film with copper cladding on both sides of the film as shown in step one. Next, the copper is etched to create an inductor and bottom layer for a capacitor on one side of the film as was explained previously in inductor fabrication. A polyimide layer is spun to encase the inductor and act as a dielectric. The polyimide layer is then etched using reactive ion etching to create a thinner dielectric layer for the capacitors and provide a via to connect the center of the inductor to the top parallel plate of the capacitor. This etch is masked using Kapton tape to isolate the capacitor areas

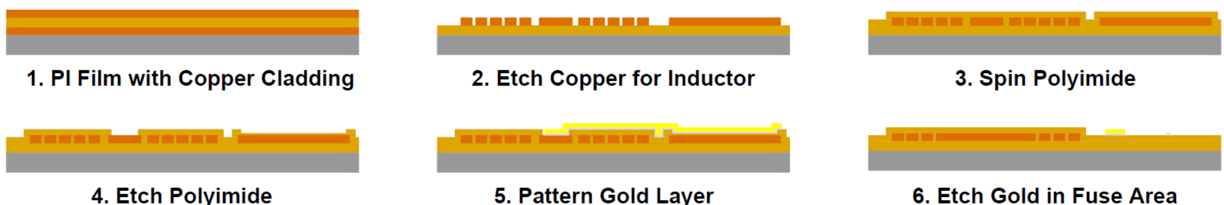

Figure 5-8. System fabrication flow. Note that step six shows a different cross section than other steps to illustrate fuse fabrication.

and center of the inductor as etched areas. The top layer of the capacitor along with an electrode connecting the top layer to the center of the inductor is patterned over the previous layers using optical lithography. Throughout this process two thin film LC circuits have been fabricated as shown in Figure 5-7 although only one LC circuit is visible in Figure 5-8. Finally, the LC circuit that contains the fuse point is modified to create the fuse. This is done by etching gold in that area with a photoresist mask to define the etched area. The photoresist is then stripped to complete fabrication. Although not necessary for the tests here, another encasing polyimide layer should be deposited over the final metal layer for robustness and biocompatibility should the sensor be used in its true application environment.

5.3 Experimental Testing

5.3.1 Thin Film LCR Components

The designed inductor and capacitor components are tested using an Agilent 4294A impedance analyzer. Component characteristics are observed using phase and impedance frequency sweeps and equivalent circuit curve fitting. Inductor and capacitor components were then bonded to a PVC bar for mechanical testing. Components are bonded to the bar by first roughing the backside of the polyimide with sand paper, cleaning each surface, and bonding with Cyanoacrylate (CN) adhesive obtained from Tokyo Sokki Kenkyuju Co., Ltd. A strain gage is bonded to the opposite side of the bar in the same position as the component. The PVC Bars are then loaded in bending.

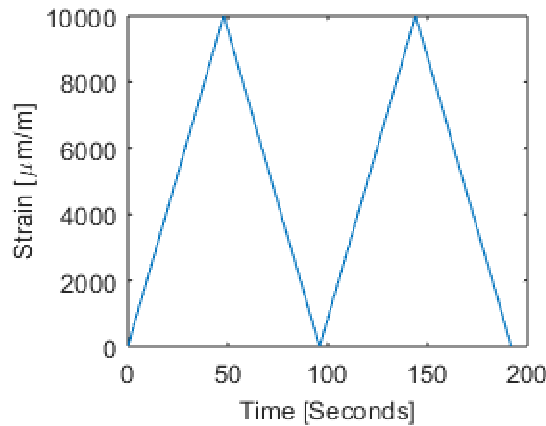

Figure 5-9. Loading procedure for testing fused sensors under increasing strain in tension.

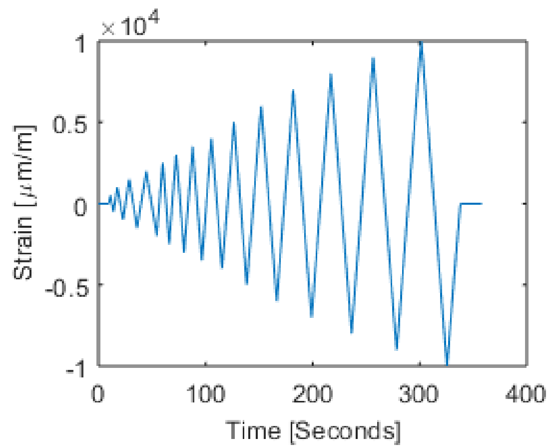

Figure 5-10. Loading procedure for testing fused sensors under cyclic loading of increasing strain magnitudes.

5.3.2 Fused Sensors for Strain Sensing

The thin film metal tearing fuse sensors are tested are tested electrically using an Agilent 34461A digital multimeter. The thin film metal components are bonded to PVC bars and tested mechanically using the same setup specified in the previous section. Two loading procedures are used in testing the thin-film metal fuse sensors. The first, shown in Figure 5-9, is a load pattern with increasing strain levels in only tension to replicate the conditions that might be seen by an osseointegrated prosthetic sensor in hoop strain as described in Section 5.2.3. The second loading procedure is designed to more closely mimic conditions seen in traditional structural health

monitoring environments. This loading procedure loaded in tension and compression cyclically with increasing amplitude as can be seen in Figure 5-10. Initially, individual sensors are tested using a digital multimeter to continually collect resistance data from the sensors along with strain data from the strain gauge. Following this testing, sets of five sensors are tested simultaneously by loading to specified strain values and then probing the five resistances of the sensors. This allows for a detailed characterization of sensor resistance response to strain. It also allows for insight into the consistency of the failure behavior of the fuses.

5.3.3 *Wireless Strain Threshold Sensing System*

The wireless strain sensing system is interrogated using a read inductor connected to the impedance analyzer as shown below in Figure 5-11. The phase response of the read inductor is collected allowing for the observation of phase dips at the resonant frequencies of the thin film LC circuits when the sensor is near the read inductor. Once this initial functionality is confirmed, the thin films are loaded mechanically with the loading procedure shown in Figure 5-12. The gradually

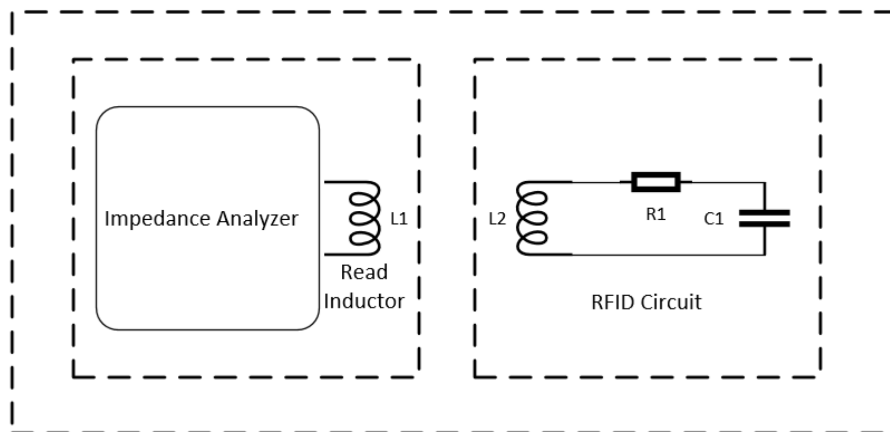

Figure 5-11. Illustration of wireless sensor readout.

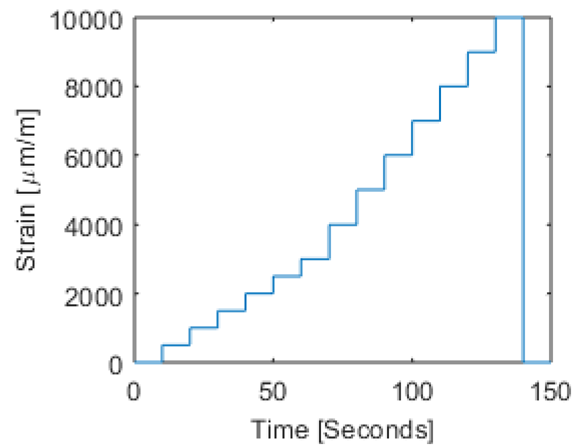

Figure 5-12. Loading procedure for LC sensing system.

increasing amplitude of the applied strain in tension is selected to mimic hoop stress as bone growth occurs in an osseointegrated implant. The phase dip corresponding to the fused LC circuit is expected to broaden and disappear as the fuse fails under strain.

5.4 Results and Discussion

5.4.1 Thin Film LCR Components

Three capacitors were fabricated with the side lengths and capacitances shown in Figure 5-13. The strain response of the capacitors due to changing thickness of the dielectric layer from Poisson's effect can be seen in Figure 5-14. This illustrates effective strain sensing to be utilized

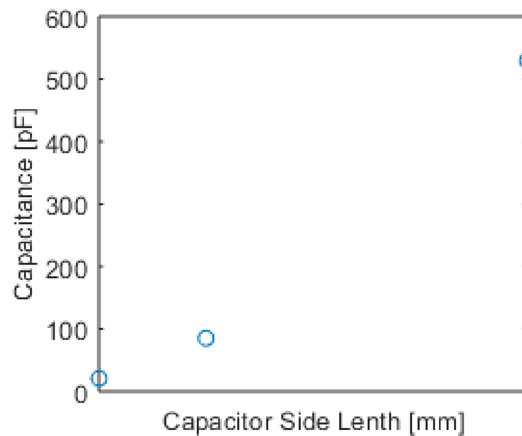

Figure 5-13. Capacitor values for parallel plates of varying side length.

in the final sensing system by monitoring the resonant peak of the reference circuit as a strain indicator. A fabricated copper inductor can be seen below in Figure 5-15a. The impedance-phase curve of the inductor is shown in Figure 5-15b to illustrate the necessary electrical characteristics. The final design is chosen for balance between inductor quality factor and footprint of the inductor, which was minimized. This inductor had a resistance of 800 mΩ, inductance of 1.64 μH, and quality factor of around 2 at 1 MHz. The inductor had a footprint of roughly 17 mm^2.

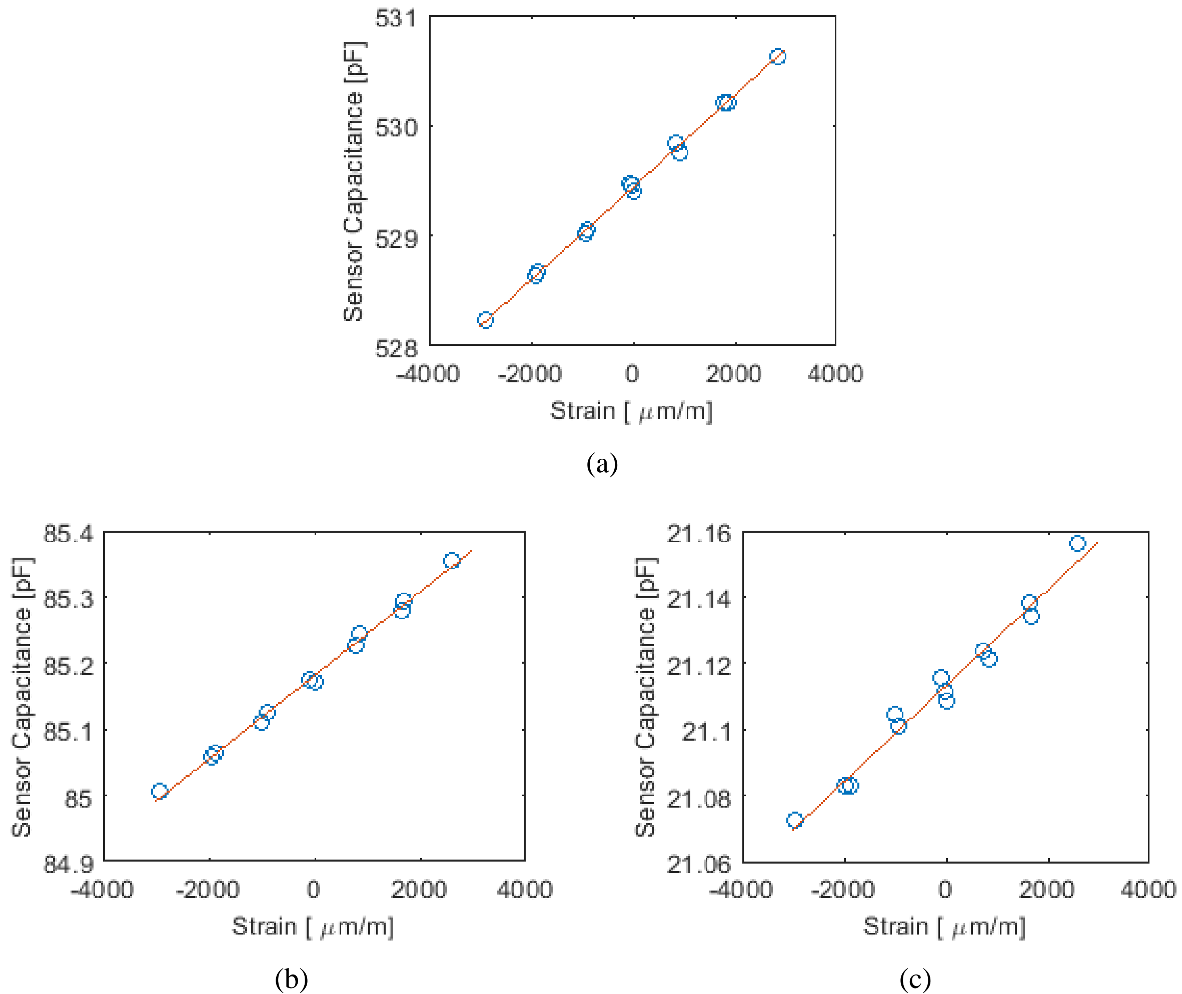

Figure 5-14. Mechanical testing of capacitors with side lengths of (a) 10 mm, (b) 4 mm, and (c) 2 mm.

(a)

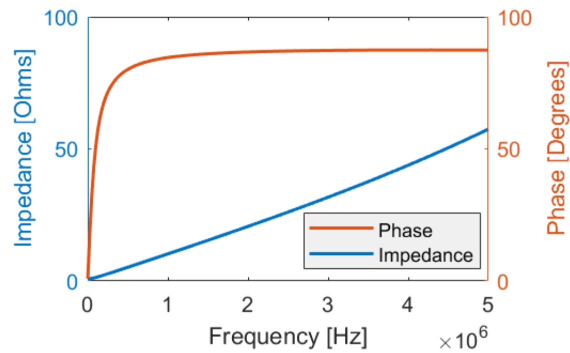

(b)

Figure 5-15. Copper thin film inductor (a) photo after fabrication and (b) phase and impedance curves for inductor characterization.

5.4.2 Fused Sensors for Strain Sensing

The fused sensors were strained to observe electrical failure behavior of the metal fuses underlying physical phenomena for design. The fused sensors were first tested in cycles of increasing tensile then compressive strain. Two different electron beam evaporators were used to deposit the films; an Angstrom Engineering (AE) EvoVac Evaporator and an Enerjet Evaporator. The AE evaporator has been characterized to deposit a titanium layer with compressive residual stress from evaporation, while the Enerjet deposits a titanium layer with tensile residual stress. Each film is tested twice with the loading procedure shown previously in Figure 5-10. The results of two fuse sensors fabricated with the AE evaporator are seen in Figure 5-16 and the results from the Enerjet Evaporator are shown in Figure 5-17.

In the first test, shown in Figures 5-16a, 5-16c, 5-17a, and 5-17c, the fuses from both evaporators showed similar electrical responses to mechanical loading that can be interpreted in the context of common metal failure progressions. First, in the low-strain regions below roughly 2,000 microstrain the sensors show little change in resistance due to strain. This is thought to be

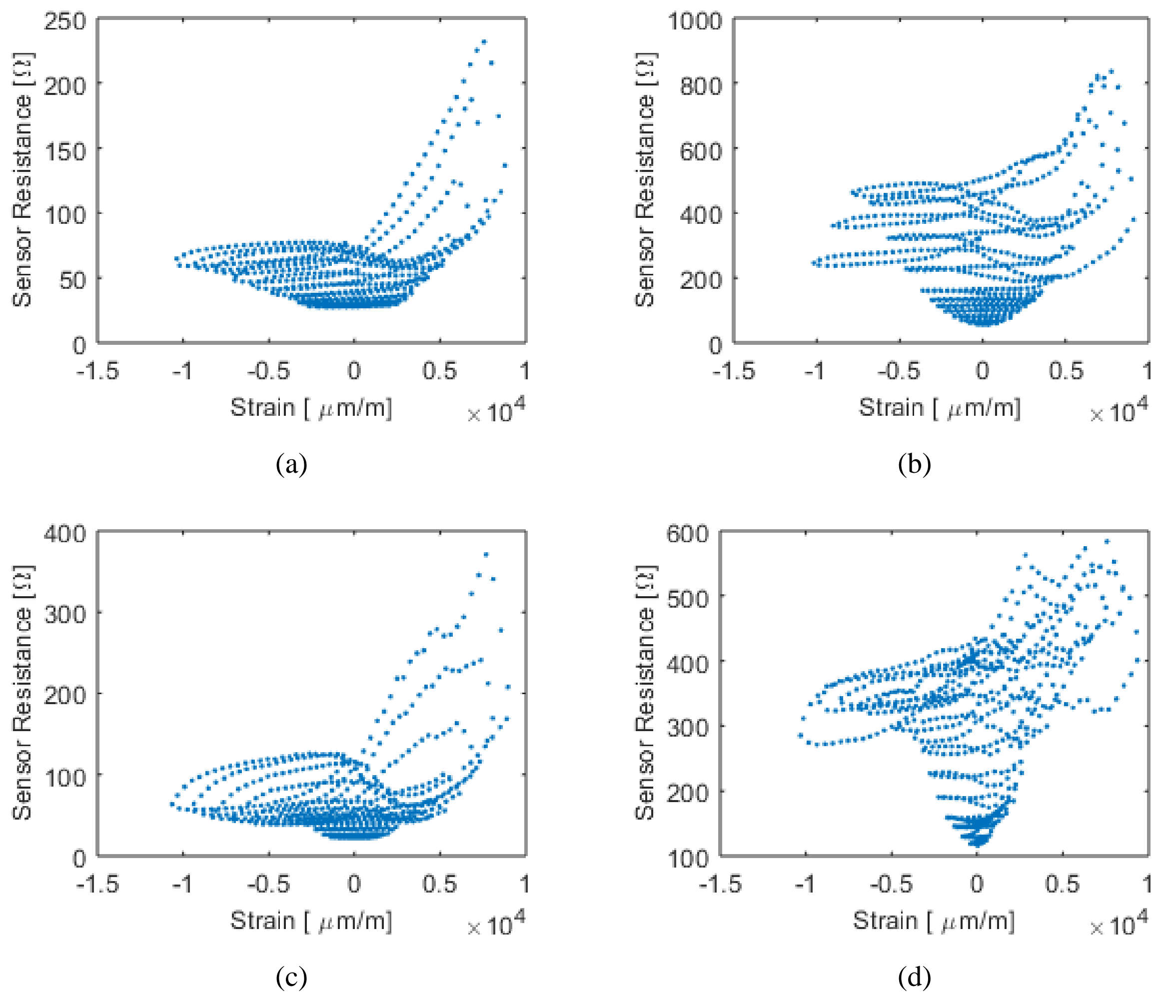

Figure 5-16. Tensile and compressive testing of fused sensors fabricated with an AE Evaporator sensor 1 (a) test 1 and (b) test 2 and sensor 2 (c) test 1 and (d) test 2.

the case since the titanium remained in the linear elastic region here, causing little change in the metal. Following this, the fuses started to behave in a hysteretic manner with a permanent increase in resistance occurring at high strains. This is thought to initiate as the metal passes the yield point begins to deform plastically. At strains higher than roughly 5,000 microstrain this behavior became far more dramatic as large resistance increases were observed. These resistances would return to lower values as strain was released but not back to initial values.

In the second test, shown in Figures 5-16b, 5-16d, 5-17b, and 5-17d, the fuses began with higher resistances from the first test. Resistance increased more dramatically and at lower strains

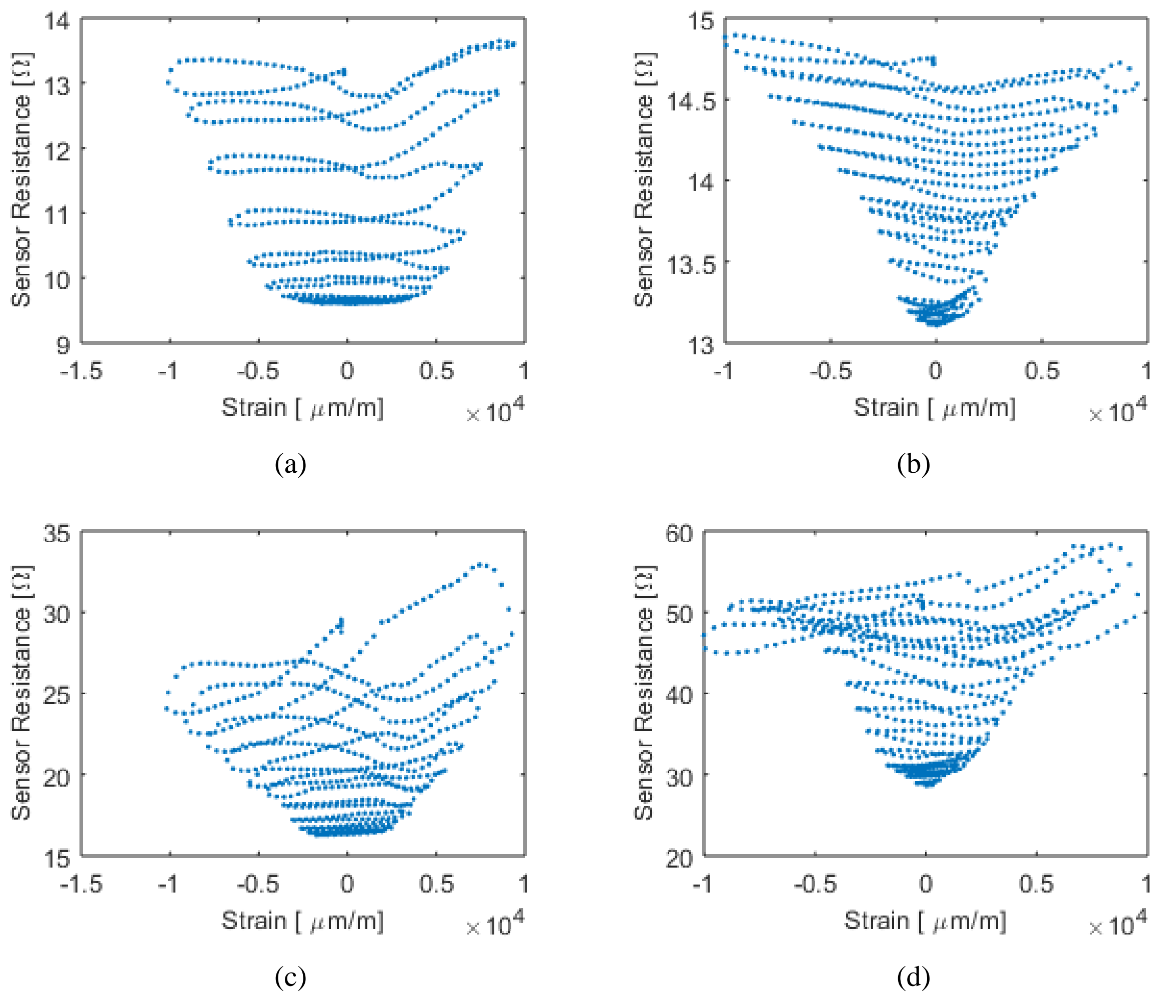

Figure 5-17. Tensile and compressive testing of fused sensors fabricated with an Enerjet Evaporator sensor 1 (a) test 1 and (b) test 2 and sensor 2 (c) test 1 and (d) test 2.

than in the first test. This illustrates fatigue behavior in addition to the behavior observed previously. One difference between the two evaporators was the balance between the resistive response due to strains in the tensile and compressive regions. The Enerjet evaporator showed a similar degree of resistive change while many of the Angstrom Engineering Evaporator testes showed a larger resistance increase in tension. This difference could be a result of stresses from deposition or differences in material composition between the two depositions.

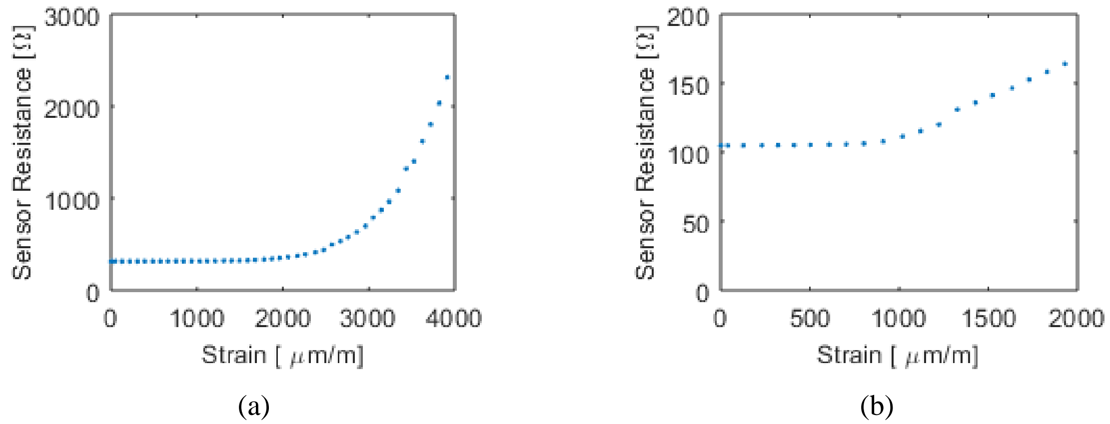

Figure 5-18. Example responses to strain over first load cycle for fuse of (a) width of 0.5 mm, length of 1 mm, and thickness of 100 nm and (b) width of 0.5 mm, length of 1 mm, and thickness of 200 nm.

Next, fused sensors of varying geometries were fabricated in the Angstrom Engineering evaporator and tested under two cycles of increasing tensile strain. This illustrates a use case like the hoop-strain *in vivo* sensor described earlier in Section 5.2.3. Three fuse widths, lengths, and

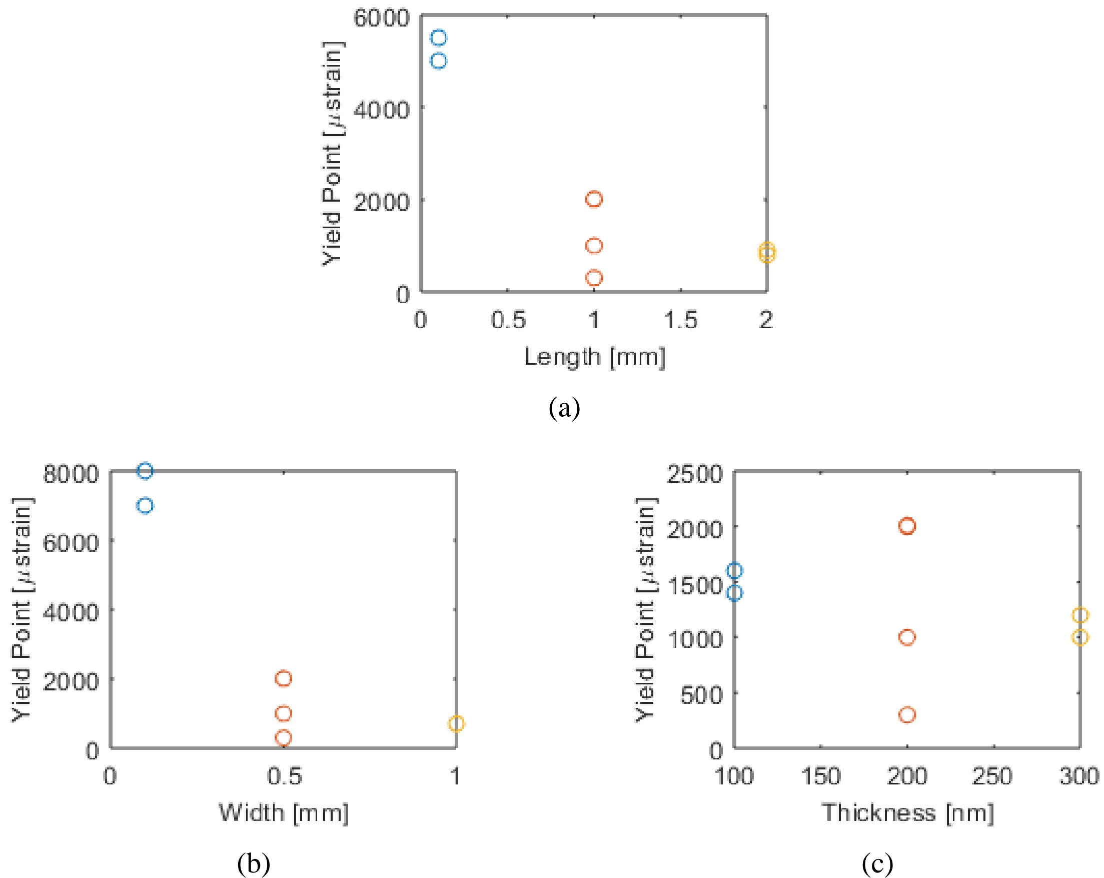

Figure 5-19. Yield points of sensors tested.

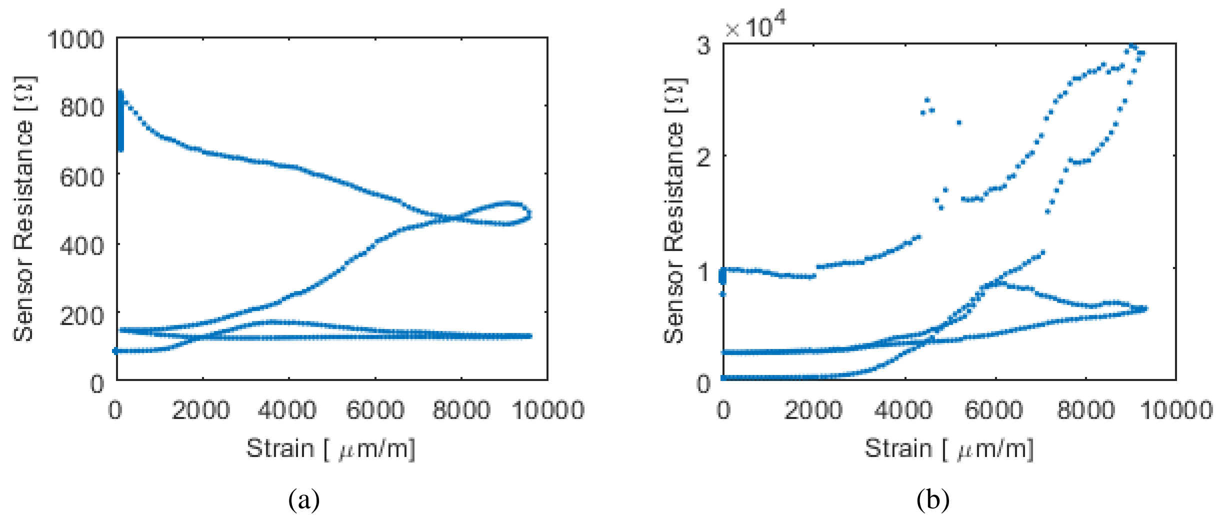

Figure 5-20. Two cycle loading test showing behavior of fuses at high and repeated strains.

thicknesses were tested. The results from this testing are shown below in Figures 5-18, 5-19, and 5-20. Figure 5-18 shows two typical responses to the initial strain loading, although there was some variation between tests. The fuses would begin with no response to strain after which resistance would begin to increase suddenly. This is thought to occur as fuses left the linear-elastic region as mentioned in the previous paragraph.

Figure 5-19 shows where these yield points occurred for each sensor tested. All fuses had a length of 1 mm, width of 0.5 mm, and thickness of 200 nm unless otherwise varied and labeled on the x-axes. Four sensors were tested with the base set of dimensions and two were tested with each varying parameter. The fuse yield point was observed to decrease with length, decrease as width increased, and decrease slightly with thickness. This provides the basis for empirical fuse design. In Figure 5-20 two typical complete tests are shown with two load and unload cycles. The primary takeaway here is that resistance does not return to initial values when unloaded and repeated loading at high strains will cause resistance to continue to increase with subsequent cycles.

The data set utilized for Figures 5-18, 5-19, and 5-20 provided many insights for fuse design. Narrowing fuse width caused a slight increase in the resistive response but also caused a higher initial resistance. Widening width had little effect and behaved like the base dimensions tested. Increasing length caused higher resistances due to strain, however it also increased initial resistance as expected geometrically. Decreasing length caused a more dramatic increase in resistance. Finally, both thinner and thicker titanium layers were more prone to large resistance increases than the base case of 200 nm. This could be due to a lack of overall material in the 100 nm film and stresses from deposition in the 300 nm film with the 200 nm film as a more robust middle ground. It is possible that different ranges of geometry, especially smaller thickness and width, could be interesting for engineering additional control. For now, the results are utilized for design of a fuse, pending validation of consistency.

Next, groups of fused sensors were tested in tension to provide insight into the consistency of the results observed in the previous individual sensors. The results of this can be seen below in Figure 5-21, where the same geometries and loading procedures were used as in the previous Figure 5-19. Here, however five resistors with each sensor geometry were tested taking data at each 1,000 microstrain increment and the increase in resistance relative to initial resistance of each sensor was documented. The x-axis in these charts shows the initial resistance of the fuse and the y-axis shows the strain at which the fuse resistance hit 2x, 10x, and 20x this initial resistance. Each threshold is shown as a circle and those sensors showing less than three circles only hit that number of strain increments (i.e. resistance stayed too low to reach the next threshold). This testing again showed that the narrowest and shortest fuses showed the greatest increase relative to their initial resistance. Interestingly it also validated the finding that 100 nm and 300 nm titanium thicknesses were both likely to see large resistance increases while the 200 nm thick films were relatively

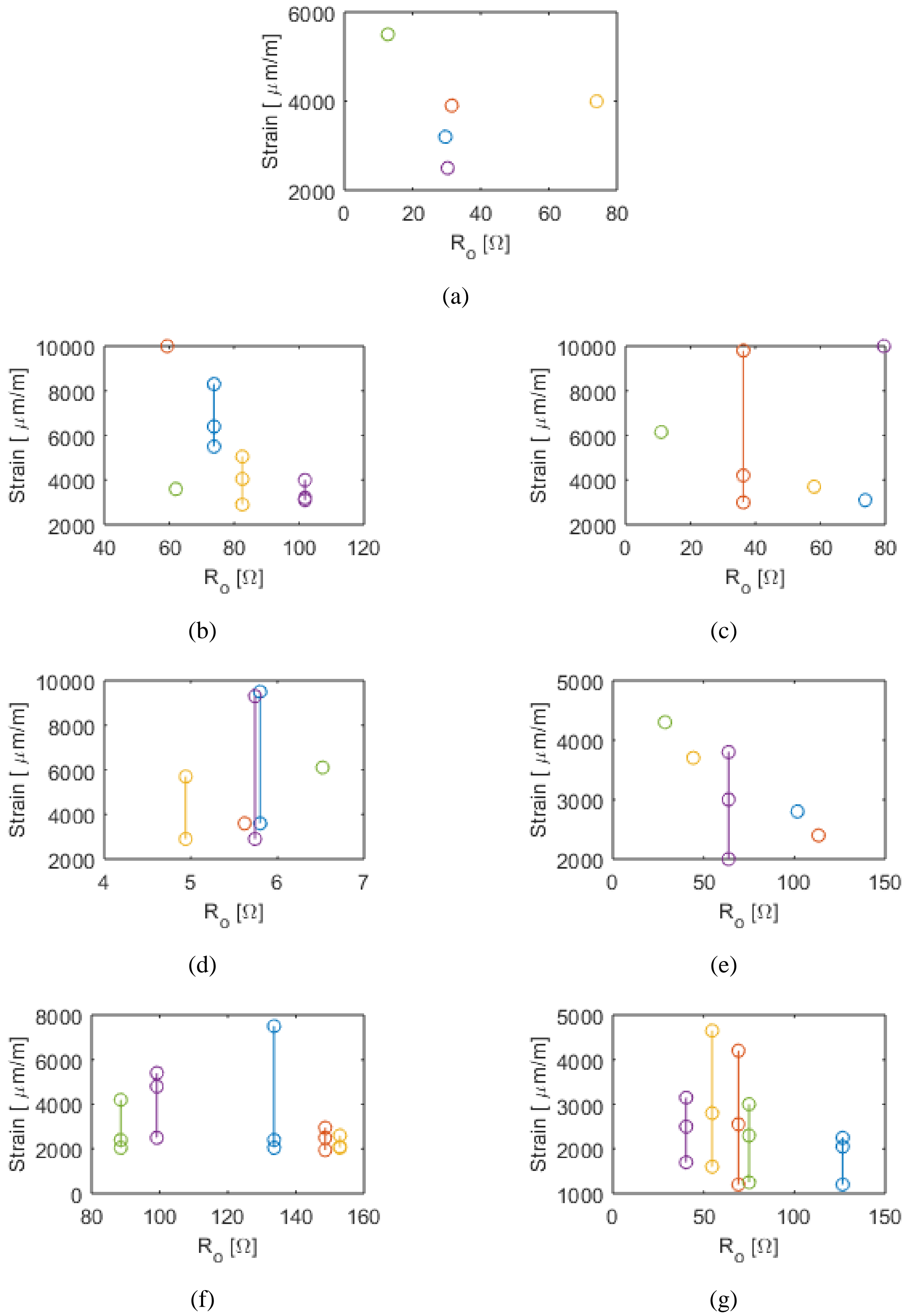

Figure 5-21. Plot showing strain at which 2x, 10x, and 20x initial resistance (x-axis) is reached. Default design values (w=500 nm, L=1 mm, th=200 nm) are plotted in (a), width is altered to 100 nm in (b) and 1 mm in (c). Length is altered to 100 nm in (d) and 2 mm in (e). Thickness is altered to 100 nm in (f) and 300nm in (g).

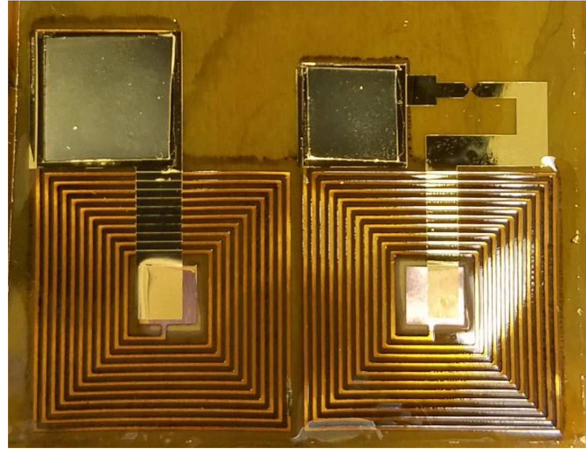

Figure 5-22. Picture of sensing system.

robust. The design parameters were found to have effects of varying degrees that are instructive for initial use here and warrant much future investigation into such potential mechanical-electrical designs in thin film systems. For our purposes here a fuse design of 0.5 mm length, 0.5 mm width, and a 300 nm thickness was selected for low initial resistance and desirable failure characteristics. The films do not show an ideal complete failure (infinite resistance) at a specific strain value. However, the detailed failure characterization and subsequent consistency validation provide a characterization of fuse behavior and allow their use as an indicator of a strain threshold. Additionally, the initial tensile and compressive testing illustrate how such sensors could be designed for conventional SHM setting where excessing positive or negative strains are possible. The fatigue durability of a given fuse could potentially also be designed based on process and geometry for the needs of various sensing applications.

5.4.3 Wireless Strain Threshold Sensing System

The fabricated final LC sensing system can be seen in Figure 5-22. Microscope images of the sensor, including the fuse, can be seen in Figure 5-23. The exposed titanium for the fuse can be seen in Figure 5-23a and Figure 5-23b. The layers of the capacitor are shown in 5-23c and the

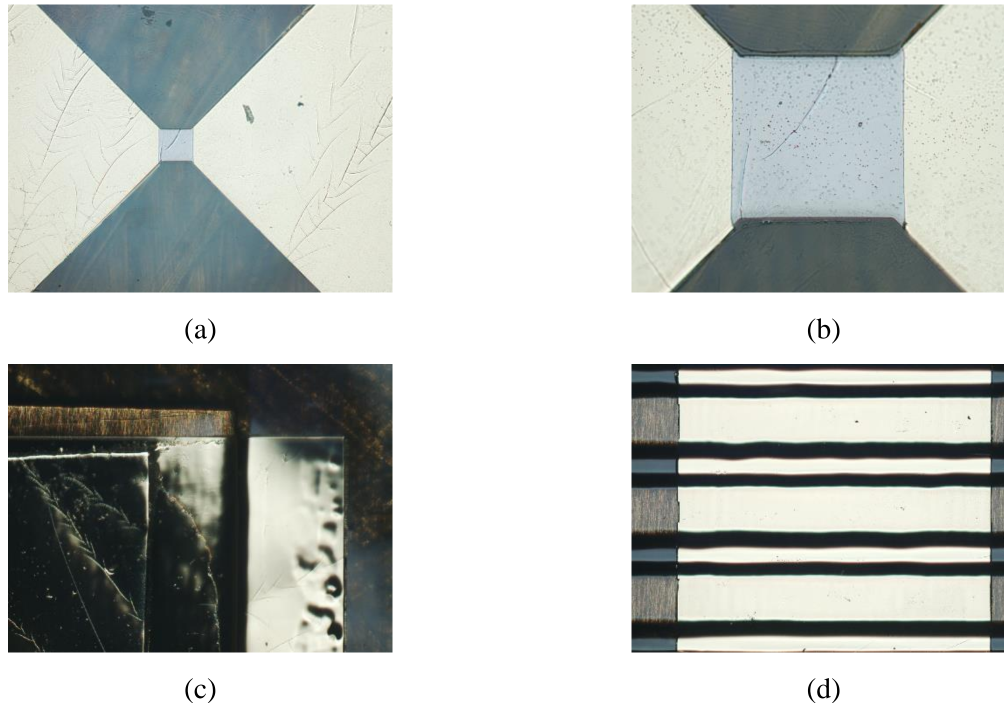

Figure 5-23. Microscope images of fuse point with width of 0.5 mm and length of 0.5 mm (a) and (b), corner of capacitor (c), and inductor (d).

inductive coil underneath an electrode between the capacitor and inductor is shown in Figure 5-23d.

Raw data showing the behavior of the read inductor with and without a sensor nearby is shown in Figure 5-24. As the read inductor is moved near the sensor, two frequency dips corresponding to the resonant frequencies of the two inductor-capacitor circuits are visible as shown. Once this initial functionality is confirmed the sensor is loaded gradually to approximately 10,000 microstrain in tension as shown in Figure 5-25. In this and following figures a reference signal from the read inductor without a nearby sensor was subtracted from read inductor data with a sensor nearby and shifted to start at a 90° phase. This removed error from the DAQ system and provided a clearer representation of results. At each loading step the two peaks are observed by sweeping the frequency of the impedance analyzer over a wide range then each peak is observed with more precision by sweeping over a narrower frequency range around the peak. The first peak

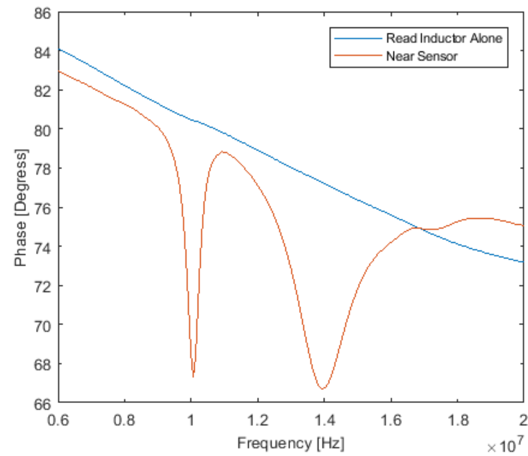

Figure 5-24. (a) Phase of read inductor with and without a sensing system in the proximity of the read inductor.

from the sensor is shown in Figure 5-25a and the second peak is shown in Figure 5-25b. In test one with this sensor, fuse failure can be observed at approximately 5,500 microstrain as the fuse sensing peak broadens at this strain point before disappearing at 6,700 microstrain and beyond.

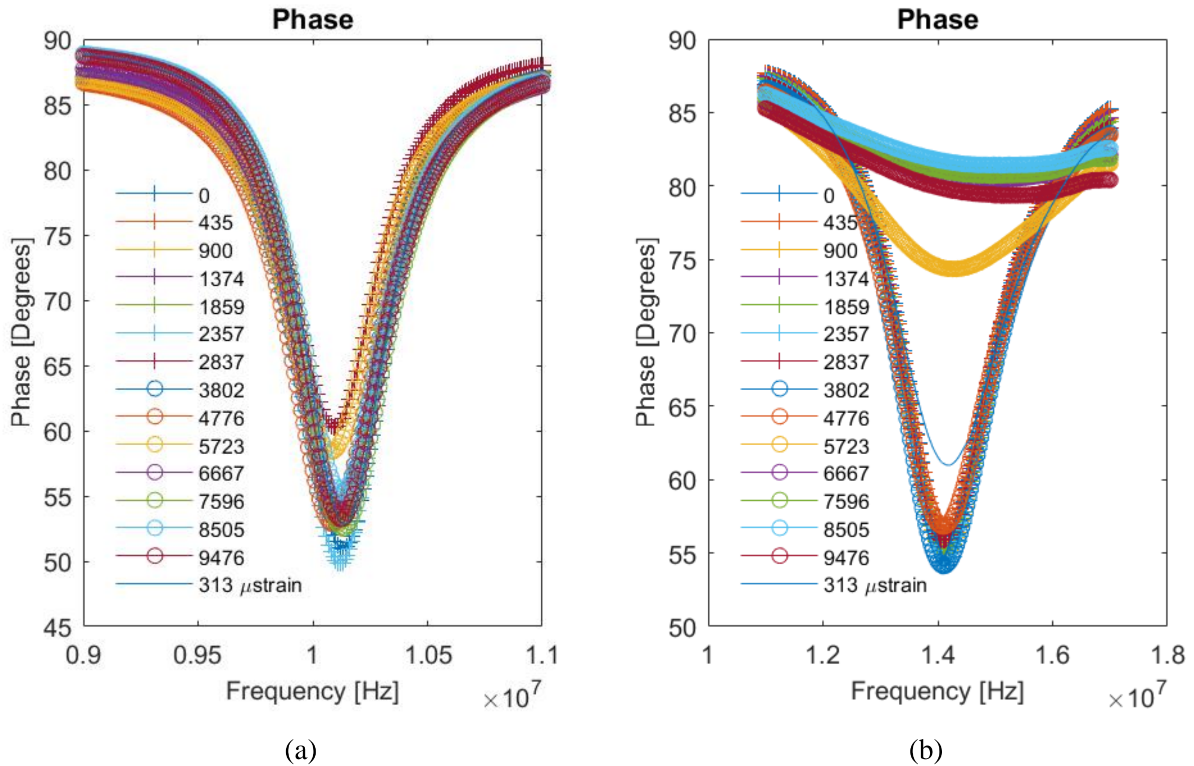

Figure 5-25. Phase response of the (a) reference peak and (b) fuse peak responding to tensile strain during initial loading.

The peak reappears with broader bandwidth than before loading after the initial test. This matches the behavior expected from the resistance testing of the individual fuses. A second loading progression matching the first was applied. This resulted in a more rapid disappearance of the fuse peak as shown in Figure 5-26. Two other sensing systems of reference and fuse LC circuits were tested showing fuse failure at similar strains and rates. This illustrates a viable means for this fused sensing approach with implications for a broad range of sensing applications.

In addition to threshold strain sensing with the fused element, the reference peak in the sensor is utilized for more precise strain sensing. This is achieved by observing the frequency peak of the reference LC circuit as it shifts due to the change in capacitance in the capacitor from strain. This shift in capacitance with strain can be observed from the frequency peaks as shown in Figure

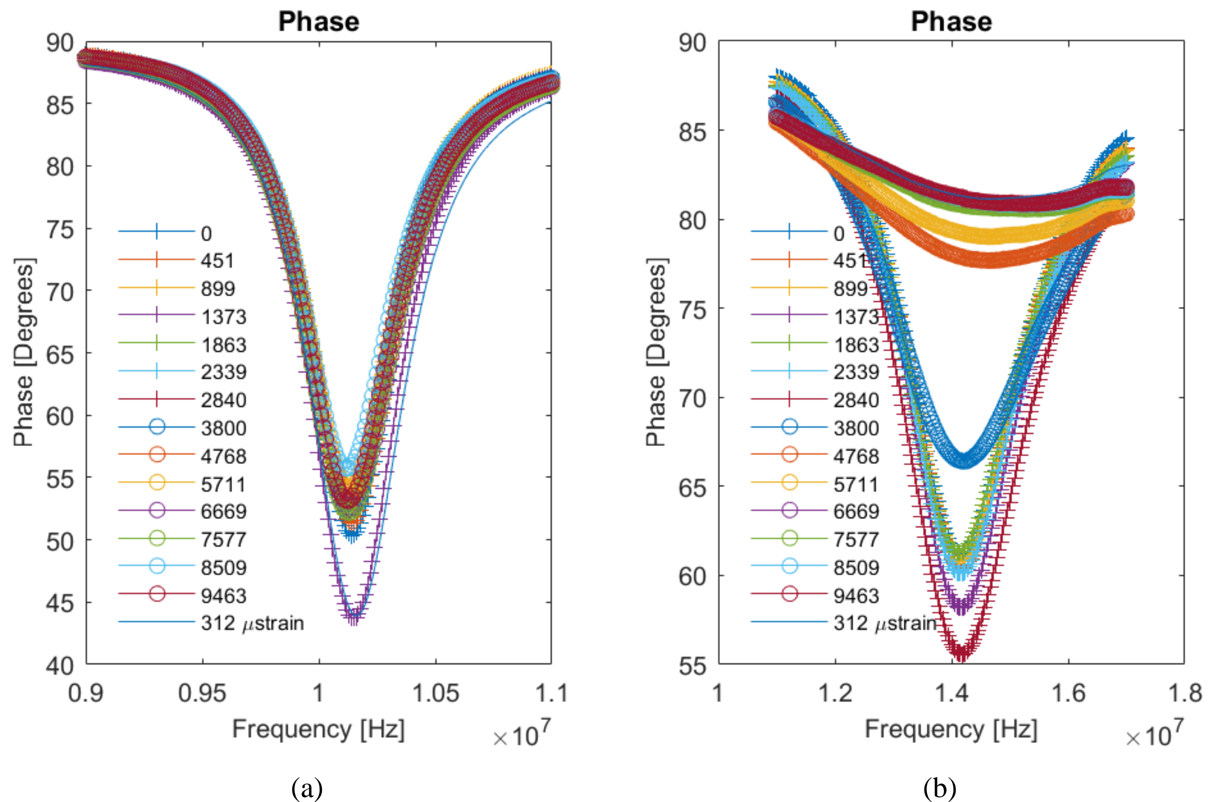

Figure 5-26. Phase response of the (a) reference peak and (b) fuse peak responding to tensile strain under a second progression of tensile loading.

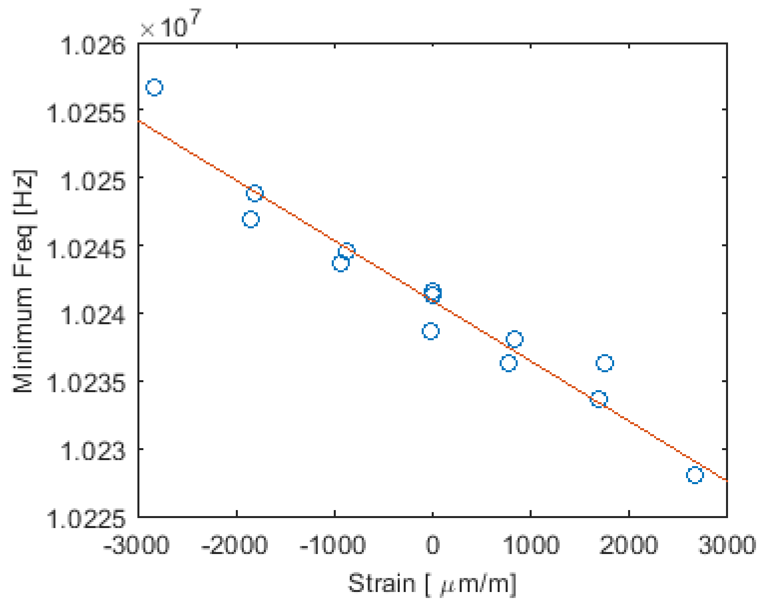

Figure 5-27. Frequency peak vs strain of the reference LC circuit.

5-27. A sensitivity can be calculated as the change in frequency between two points normalized by the average absolute frequency of the points over the strain at the two points selected in a metric similar to a gage factor in strain gages. This test shows a strain sensing with a sensitivity of approximately 0.5 with and a root-mean-squared error of 1,224 Hz from the line of best fit. This results in a noise floor of around 250 microstrain. This noise floor is a result of the test setup available to the researchers for this study. The noise floor of the sensor itself is likely considerably lower as sensing is based on the capacitive element shown previously, the largest of which had a noise floor of around 50 microns. This is still not necessarily the limit of the sensing system as the capacitor noise floor was also likely due to the testing equipment. This illustrates a strain sensor for continuous measurement and functionality in addition to the fused threshold sensing achieved previously.

The progression of peak strains could also be estimated using the bandwidth of the fused sensing inductor-capacitor circuit. The resistance of the circuit, which is primarily determined by the fuse, dictates the bandwidth, which can be observed from the read inductor. The decrease in

resistance during unloading in these fuses would complicate such an approach. However, with well-calibrated awareness of the fuse failure progression a bandwidth approach could provide a clear estimate that a specific maximum strain had been observed by the structure.

5.5 Chapter Summary

Many applications would benefit greatly from wireless thin film sensing systems, however work remains to create a system of the form and robustness required for structural sensing. In this study, a fused approach to wireless threshold strain sensing is presented along with the necessary thin film technologies and processes for implementing such an approach. This begins with the design and fabrication of thin film circuit primitives to be conformable, robust, and biocompatible for use in many applications. Then, a new approach to mechanical-electrical design utilizing the nonlinear strain-resistance response of metals films to create strain threshold fuses is presented. A potential method for the design of such fuses is detailed that includes film geometry and fabrication processing as potential design variables. These fuses are tested for resistance response to strain and the results and potential for various applications in structural health monitoring are discussed. Finally, the design components are integrated to create a wireless threshold strain senor based on a fused sensing approach. This sensor is then tested wirelessly using an impedance analyzer and read inductor to illustrate the presence of a reference and fused sensor peak when the read inductor is near the sensor. The sensor is tested by gradual loading in tension allowing for the observation of the failure behavior of the fuse. This validates both the proposed sensing architecture and the approach of utilizing advanced metal mechanical-electrical design in such sensing systems. In addition to the functionality of the fuse, the reference circuit in the strain sensor is utilized for continuous strain measurement.

While this work illustrates exciting concepts and capabilities, it also raises additional questions for future investigation. The metal fuse suggested here illustrated the potential approach to such a design, but the investigation of different materials, processes, or geometries might allow for greater performance control and more precise information. Similarly, there is potential to consider design not only in the context of a singular exceedance of peak strain but instead to detect material fatigue by utilizing the durability and fatigue life of thin film design materials. Additionally, this work illustrates wireless readout, however additional investigation of readout range and robustness of readout to embedding in various materials would be valuable.

CHAPTER 6.

CONCLUSION

6.1 Summary and Thesis Contributions

The fundamental objective of this dissertation is to advance direct damage detection in structural health monitoring by addressing fundamental challenges associated with existing sensor system design. This focus is necessitated as a vast set of enabling materials, electronics, and communication technologies are now emerging, that can revolutionize approaches to sensor and sensor system designs. The urgency of pursuing these new methods are underscored by the fact that point-sensing and inferred damage detection methods in existence for many decades still remain the norm in assessing the state of our critical infrastructure. To this end, an overarching theory of thin film fabrication is proposed in this thesis with implications for a vast range of flexible and conformable thin film strain sensors and applications in SHM. The thesis goes beyond simply advancing fabrication methods by illustrating three specific implementations of strain sensing systems to address specific structural health monitoring challenges. This specificity is necessary as thin film sensing system designs can vary widely depending on the specific structural system monitored. However, carefully crafted application studies address key challenges to thin film SHM approaches and, as such, allow for key contributions well beyond the specific system designed or challenge addressed. Thus, an overarching fabrication theory, specific fabrication practices, and novel material utilization and sensing approaches are presented to advance direct

monitoring and damage detection for infrastructure and non-infrastructure (e.g. medical implant) systems. The following sections summarize the key intellectual contributions of the thesis.

6.1.1 Fabrication of RLC Primitives and Methods for Integration in Thin Film Sensors

In Chapter 2, a set of thin film design and fabrication capabilities was presented as a base set of tools for the sensor designs presented in the remainder of the thesis. Processing presented here included sections on metals, polyimide, polymer-thin film composites, and the integration of dissimilar materials into a single thin film system. Thin film inductor, capacitor, and resistor circuit primitives were fabricated from these materials as illustrations of the proposed processes and to provide a broad set of basic building blocks for thin film analog sensing electronics. A resistive strain sensor on a flexible substrate was fabricated showing design of bulk resistance through geometric control and control of strain sensitivity through material selection. This illustrated basic electrical and fabrication building blocks for realizing strain sensing designs and concepts for similar future research efforts that followed. The key intellectual contribution was the advancement of fabrication methods that allowed such a broad array of materials, each with unique fabrication methods and conditions, to be combined harmoniously into a single sensing system. Another contribution is the use of geometric control to essentially control device type and its functional features. Key to this contribution has been the tailoring of SWNT-PSS/PVA films to accurately tear with minimal defect during lithographic processing.

6.1.2 Fully Integrated Carbon Nanotube Composite Thin Film Strain Sensors on Flexible Substrates for Structural Health Monitoring

Multifunctional thin film materials show great promise for a vast range of applications, including SHM. However, advances are needed in integrating such materials into functional

sensing systems at the cost and performance standards required for sensing applications. In Chapter 3, the broad class of multifunctional materials were enabled through fabrication processes and methodologies that are widely applicable in MEMS and IC industries. This is achieved through the design of a strain sensing system constructed with a layer-by-layer deposited SWNT-PSS/PVA film as the primary piezoresistive sensing material. Electronics were integrated with the piezoresistive thin films to create a fully integrated strain sensing system enabling the design of various sensor and circuit configurations in a form with the size and durability required for many SHM applications. The fabrication process is useful well-beyond the specific instance provided herein as it can be utilized for various multifunctional sensing films and even multiple interconnected films on a single substrate. The process began with a metal stack designed to be durable to thermal, chemical, and mechanical loads as would be encountered either in later fabrication steps or in the final use environment of the film. Lithographic lift-off was utilized to pattern LbL thin films on a flexible polyimide substrate. The fabrication process concluded with surface mount IC components to complete readout circuitry. Additional robustness was also provided by encasing the top layer of the sensor in silicone for use in a field-like setting.

The designed process produced a fully functional strain sensor that was tested in a laboratory environment and then utilized in testing on a structural assembly accurately representing a realistic SHM setting. Sensor characterization was first conducted on PVC coupons in cycle four-point bending to observe the performance of the fully integrated sensor. These tests showed a strain sensitivity greater than 5 V/ε and linearity near 1. As importantly for the purposes of this study, the fabrication produced a very robust film assembly capable of strains beyond 17,000 με before failure of the sensing system. The sensors were observed to fail at soldered connections between the metal stack and IC components. This matched expectations as these

brittle connections are expected to provide the initial strain vulnerability. A second set of tests were conducted on a steel beam-column sub-assembly that was loaded laterally with increasing amplitude until failure. This test showed a sensor sensitivity of around 1.5 V/ε with a linearity above 0.9. During the later stages of testing, a fracture occurred at the connection of the steel beam and column that resulted in vibrations that damaged the thin film sensor. Overall, the realistic SHM test illustrated the sensor readiness for service as a robust strain sensor. The study provided a scalable process for integrating multifunctional materials with conventional ICs in a large-area sensing skin for structures. This is a major contribution as this is the first study in the SHM field (to the author's knowledge) of integrating rigid IC chips onto a thin film to enhance the sensitivity of the sensor readings. This advances the sensor to a higher level of technology readiness that exceeds previous thin film sensors proposed in literature.

6.1.3 Scaling Nanocomposites to Sense Strain Over Large-Areas

In Chapter 4, the challenge of spatial damage detection was address through a novel approach proposed as an alternative to current methods utilizing electrical impedance tomography (EIT) of monolithic uniform nanocomposite films. EIT has shown great promise for direct detection of spatial damage on structures, however the method has drawbacks including significant computational requirements and the possibility of failing to converge that can create uncertainty in the inverse solution. This alternative proposed was based on the fabrication of a patterned grid of polymer nanocomposite strain sensitive resistors and an inverse algorithm for determining resistive values from the edges of the network. The sensor was fabricated on a flexible polyimide substrate using optical lithography and an LbL fabrication process to deposit SWNT-PSS/PVA films. The algorithm was then validated with an array of off-the-shelf resistors. Next, it was tested with a thin film sensing network prior to loading. The algorithm was first shown to effectively

estimate resistor values within around 2% error for a four-by-four grid of uniform of discrete through-hole resistors. One of the resistors in this initial example was then replaced with a significantly lower resistance, which the algorithm was able to detect without issue. This illustrated a robustness to sharp changes of resistance values with the approach, an issue that can be a significant challenge with EIT. The algorithm was next shown to effectively estimate the values of a two-by-two resistive nanocomposite (SWNT-PSS/PVA) array with similar fidelity to that shown for off-the-shelf resistors.

Two SWNT-PSS/PVA grid array thin film skins were utilized for strain sensing on a beam in bending. The first was oriented with six sensors aligned with axial strain and six experiencing zero strain along the elements longitudinal axis. This sensor skin was highly effective in strain tracking on all elements oriented along the primary strain direction without similar trends in the other sensors tested. Next, a second array sensor was tested with an orientation at 45° to the primary strain direction so that all sensing elements would experience similar strains. In this test all elements trended with strain in a similar manner as expected again displaying the effectiveness of the algorithm and entire network tested. In the second test where less strain was present, significant drift was observed in the sensors. While this is a known characteristic of SWNT-PSS/PVA films similar to those utilized herein, it could present challenges for high-precision applications. The overall results showed an effective method that was much more direct than EIT computationally, providing the benefits expected. Additionally, the algorithm was robust to sharp resistance changes which can be problematic in EIT. The primary limitation of this approach currently is scalability. None the less, the Chapter contributed a novel approach to spatial strain mapping using a large area sheet with patterned strain-sensitive (piezoelectric) elements.

6.1.4 Wireless Inductive Strain Sensor

In Chapter 5, an analog wireless strain sensing system is designed and tested to utilize a "fused" approach to strain threshold detection with thin film materials. This chapter focused on applications where embedded sensing and wireless readout are required in contrast to the direct and distributed sensing targeted in the previous chapters. The motivating example was the embodiment of thin film strain sensors in osseointegrated prosthesis systems. The chapter began with the fabrication of thin film inductors and capacitors to make a wireless inductive readout interface for a capacitor-based strain sensor. Next, a fuse was designed as a "failure point" for the thin film system triggered when a specified strain threshold was experienced. The fuse was designed as a titanium metal thin film as this material could both provide an effective fuse and simultaneously function as an adhesion layer between a flexible substrate and gold conductor layer. Finally, a complete system with two inductor-capacitor (LC) circuits as the fused sensor and reference were fabricated on a polyimide sheet. This was achieved using a copper-clad polyimide material as the base layer and for inductor fabrication. Polyimide and gold were then utilized for the dielectric and top metal layer.

The resistance of the fused sensors was tested under strain to observe their viability as a fuse material. Width, length, thickness, and fabrication tool were varied to observe associated differences in resistance response to strain. A characteristic failure progression for these fuses was created along with the hypotheses as to fundamental material phenomena underlying the various behavior stages. The consistency of observed phenomena was confirmed through additional testing. From this body of work a final fuse design was chosen empirically for use in the proposed sensing system. This presented a novel design concept in the utilization of metal mechanical properties beyond the linear-elastic range for electrical response in systems.

The sensing system was fabricated and tested to illustrate the fused sensing approach. Three systems were tested and showed similar behavior with the fused peak disappearing in the manner designed, while the reference peak remained throughout testing. A second test with the same loading procedure showed similar behavior of the fuse in the systems to those observed in isolation. The resonant peak of the reference LC circuit was also utilized as a strain sensor by observing shifts in the peak frequency under strain due to the strain sensitivity of the capacitor. This illustrated a means for wireless damaged detection that is easily readable by wireless methods and sufficiently robust to a wide range of harsh application environments. Additionally, it illustrated a viable route to sensing with fused elements for various measurands in a form that can be adjusted for many failure materials and fuse designs. The wireless interface included in a thin film package is a major intellectual contribution of the work. In fact, it could have been used to read out the measurements from the other sensor prototypes presented in this thesis.

6.2 Future Work

The systems and concepts put forth in this work open the door for future studies in many areas. The work with SWNT-polymer composites illustrated a path forward but also a number of challenges for working with such materials. One such challenges is the electrical drift that can be observed in some such films over long periods of electrical stimulation under direct current (DC). A thorough characterization of this drift and deeper understanding of the underlying physical phenomena would be useful to either model or eliminate it. The potential for such materials in thin film systems also presents future possibilities. Advanced sensing system functionality such as on-film logic for basic processing and patterns designed to differentiate between structural damage modes would be exciting advances in thin film SHM. The proposed array-based alternative to EIT is also more a starting point instead of a destination for research progress in large area skins for

spatial mapping of strain. Addressing scaling challenges in such an approach by modifying the proposed algorithm or utilizing patterned arrays with an alternative algorithm could significantly build on the potential shown here. The geometric simplification of this approach also invites the consideration of utilizing other physics for the inverse solver. For example, utilizing complex impedance and investigating impacts on computational complexity and solution stability.

The research on thin film sensing systems with inductors, capacitors, and resistors as building blocks also invites additional investigation. The fused sensing approach using thin film materials in useful for a variety of arenas where threshold detection could initiate an alarm for additional investigation. This might be in the form of cheap and easily interrogated sensors for strain thresholds in SHM or something such as corrosion or gas detection in another setting where the fuse is triggered by either phenomenon. The use for structural applications requires greater investigation into the materials that might form fuses, their underlying response to the proposed stimulant, and how to handle and install such materials in the film system. In addition to creating a fuse that breaks at the initial onset of a threshold strain, utilizing the fatigue life of a thin film might be another interesting way to develop a similar system that assesses fatigue in structures in addition to isolated loading incidents.

REFERENCES

[1] American Society of Civil Engineers (ASCE), "2017 Infrastructure Report Card," Reston, VA, 2017.

[2] M. Moore, B. Phares, B. Graybeal, D. Rolander, and G. Washer, "Reliability of Visual Inspection for Highway Bridges," *J. Eng. Mech.*, vol. II, no. FHWA-RD-01-020, p. 486, 2001.

[3] J. W. He, M Y; Hutchinson *et al.*, "A Summary Review of Vibration-Based Damage Identification Methods," *J. Appl. Mech.*, vol. 111, no. 2, pp. 270–78, 1998.

[4] Chang Liu, *Foundations of MEMS*. Upper Saddle River, NJ: Person Prentice Hall, 2012.

[5] C. Liu, *Foundations of MEMS*. Person Prentice Hall, 2006.

[6] R. R. Schaller, "Moore's law: past, present and future," *Spectrum, IEEE*, vol. 34, no. 6, pp. 52–59, 1997.

[7] G. J. Pottie and W. J. Kaiser, "Wireless integrated network sensors," *Commun. ACM*, vol. 43, no. 5, pp. 51–58, 2000.

[8] J. Wu, G. K. Feeder, and L. R. Carley, "A low-noise low-offset capacitive sensing amplifier for a 50-ug/sqrt(hz) monolithic CMOS MEMS accelerometer," *IEEE J. Solid-State Circuits*, vol. 39, no. 5, pp. 722–730, 2004.

[9] R. G. Azevedo *et al.*, "A SiC MEMS resonant strain sensor for harsh environment applications," *IEEE Sens. J.*, vol. 7, no. 4, pp. 568–576, 2007.

[10] D. W. Monk and R. O. Gale, "The digital micromirror device for projection display," *Microelectron. Eng.*, vol. 27, no. 1–4, pp. 489–493, 1995.

[11] T.-C. Hou, K. J. Loh, and J. P. Lynch, "Spatial conductivity mapping of carbon nanotube composite thin films by electrical impedance tomography for sensing applications," *Nanotechnology*, vol. 18, no. 31, p. 315501, 2007.

[12] Y. K. Mishra *et al.*, "Direct growth of freestanding ZnO tetrapod networks for multifunctional applications in photocatalysis, UV photodetection, and gas sensing," *ACS Appl. Mater. Interfaces*, vol. 7, no. 26, pp. 14303–14316, 2015.

[13] L. Persano *et al.*, "High performance piezoelectric devices based on aligned arrays of nanofibers of poly(vinylidenefluoride-co-trifluoroethylene).," *Nat. Commun.*, vol. 4, p. 1633, 2013.

[14] Y. Wang, B. Li, L. Zhang, P. Li, L. Wang, and J. Zhang, "Multifunctional magnetic mesoporous silica nanocomposites with improved sensing performance and effective removal ability toward Hg(II)," *Langmuir*, vol. 28, no. 2, pp. 1657–1662, 2012.

[15] K. Salonitis, J. Pandremenos, J. Paralikas, and G. Chryssolouris, "Multifunctional materials: engineering applications and processing challenges," *Int. J. Adv. Manuf. Technol.*, vol. 49, no. 5–8, pp. 803–826, 2010.

[16] G. R. Whittell and I. Manners, "Metallopolymers: new multifunctional materials," *Adv.*

Mater., vol. 19, no. 21, pp. 3439–3468, 2007.

[17] K. Wille and K. J. Loh, "Nanoengineering ultra-high-performance concrete with multiwalled carbon nanotubes," *Transp. Res. Rec. J. Transp. Res. Board*, vol. 2142, no. December 2010, pp. 119–126, 2010.

[18] T.-C. Hou and J. P. Lynch, "Electrical impedance tomographic methods for sensing strain fields and crack damage in cementitious structures," *J. Intell. Mater. Syst. Struct.*, vol. 20, no. 11, pp. 1363–1379, 2008.

[19] M. Hallaji, A. Seppänen, and M. Pour-Ghaz, "Electrical impedance tomography-based sensing skin for quantitative imaging of damage in concrete," *Smart Mater. Struct.*, vol. 23, no. 8, p. 85001, 2014.

[20] A. B. Dalton *et al.*, "Super-tough carbon-nanotube fibres," *Nature*, vol. 423, no. 6941, pp. 703–703, 2003.

[21] K. J. Loh, T.-C. Hou, J. P. Lynch, and N. A. Kotov, "Spatial structural sensing by carbon nanotube-based skins," in *Proceedings of SPIE*, 2008, vol. 6932, pp. 693207–693212.

[22] C. Li, E. T. Thostenson, and T.-W. Chou, "Sensors and actuators based on carbon nanotubes and their composites: a review," *Compos. Sci. Technol.*, vol. 68, pp. 1227–1249, 2008.

[23] M. Amjadi, K. U. Kyung, I. Park, and M. Sitti, "Stretchable, skin-mountable, and wearable strain sensors and their potential applications: a review," *Adv. Funct. Mater.*, vol. 26, pp. 1678–1698, 2016.

[24] T. Yokota *et al.*, "Sheet-type flexible organic active matrix amplifier system using Pseudo-

CMOS circuits with floating-gate structure," *IEEE Trans. Electron Devices*, vol. 59, no. 12, pp. 3434–3441, 2012.

[25] J. A. Rogers, T. Someya, and Y. Huang, "Materials and mechanics for stretchable electronics," *Science.*, vol. 327, no. 5973, pp. 1603–1607, 2010.

[26] A. Nathan *et al.*, "Flexible electronics: The next ubiquitous platform," *Proc. IEEE*, vol. 100, no. SPL CONTENT, pp. 1486–1517, 2012.

[27] K. Myny, "The development of flexible integrated circuits based on thin-film transistors," *Nat. Electron.*, vol. 1, no. 1, pp. 30–39, 2018.

[28] Q. Cao *et al.*, "Medium-scale carbon nanotube thin-film integrated circuits on flexible plastic substrates," *Nature*, vol. 454, pp. 495–500, 2008.

[29] C. M. Andres and N. A. Kotov, "Inkjet deposition of layer-by-layer assembled films," *J. Am. Chem. Soc.*, vol. 132, no. 41, pp. 14496–14502, 2010.

[30] L. Persano, A. Camposeo, and D. Pisignano, "Integrated bottom-up and top-down soft lithographies and microfabrication approaches to multifunctional polymers," *J. Mater. Chem. C*, vol. 1, no. 46, pp. 7663–7680, 2013.

[31] S. H. Hur, D. Y. Khang, C. Kocabas, and J. A. Rogers, "Nanotransfer printing by use of noncovalent surface forces: applications to thin-film transistors that use single-walled carbon nanotube networks and semiconducting polymers," *Appl. Phys. Lett.*, vol. 85, no. 23, pp. 5730–5732, 2004.

[32] C. L. Chen, C. F. Yang, X. Xiong, A. Busnaina, and M. R. Dokmeci, "Patterning high

density SWNT networks on flexible Parylene-C substrate," in *TRANSDUCERS 2009 - 15th International Conference on Solid-State Sensors, Actuators and Microsystems*, 2009, pp. 1329–1332.

[33] Y. Bai, S. Ho, and N. A. Kotov, "Direct-write maskless lithography of LBL nanocomposite films and its prospects for MEMS technologies," *Nanoscale*, vol. 4, no. 15, pp. 4393–8, 2012.

[34] V. Subramanian *et al.*, "High-speed printing of transistors: from inks to devices," *Proc. IEEE*, vol. 103, no. 4, pp. 567–582, 2015.

[35] M. Segev-Bar and H. Haick, "Flexible sensors based on nanoparticles," *ACS Nano*, vol. 7, no. 10, pp. 8366–8378, 2013.

[36] B. Glisic, Y. Yao, S. T. E. Tung, S. Wagner, J. C. Sturm, and N. Verma, "Strain sensing sheets for structural health monitoring based on large-area electronics and integrated circuits," *Proc. IEEE*, vol. 104, no. 8, pp. 1513–1528, 2016.

[37] F. Burny *et al.*, "Concept, design and fabrication of smart orthopedic implants," *Med. Eng. Phys.*, vol. 22, no. 7, pp. 469–479, 2000.

[38] L. A. Korduba, M. B. M. Grabowsky, R. L. Uhl, M. M. Hella, and E. H. Ledet, "Radio rrequency identification as a testbed for integration of low frequency radio frequency sensors into orthopedic implants," *J. Med. Device.*, vol. 7, no. 1, p. 11008, 2013.

[39] S. Iijima, "Helical microtubules of graphitic carbon," *Nature*, vol. 354, no. 6348, pp. 56–58, 1991.

[40] J.-P. Salvetat *et al.*, “Mechanical properties of carbon nanotubes,” *Appl. Phys. A Mater. Sci. Process.*, vol. 69, pp. 255–260, 1999.

[41] T. T. Ebbesen, T. W., Lezec H. J., Hiura H., Bennett J. W., Ghaemi H. F, “Electrical conductivity of individual carbon nanotubes,” *Nature*, vol. 382. pp. 54–56, 1996.

[42] J. Bernholc, D. Brenner, M. B. Nardelli, V. Meunier, and C. Roland, “Mechanical and electrical properties of carbon nanotubes,” *Annu. Rev. Mater. Res*, vol. 32, pp. 347–75, 2002.

[43] C. Pang, C. Lee, and K. Y. Suh, “Recent advances in flexible sensors for wearable and implantable devices,” *J. Appl. Polym. Sci.*, vol. 130, no. 3, pp. 1429–1441, 2013.

[44] R. F. Gibson, “A review of recent research on mechanics of multifunctional composite materials and structures,” *Compos. Struct.*, vol. 92, no. 12, pp. 2793–2810, 2010.

[45] E. Artukovic, M. Kaempgen, D. S. Hecht, S. Roth, and G. Grüner, “Transparent and flexible carbon nanotube transistors,” *Nano Lett.*, vol. 5, no. 4, pp. 757–760, 2005.

[46] M. Foygel, R. D. Morris, D. Anez, S. French, and V. L. Sobolev, “Theoretical and computational studies of carbon nanotube composites and suspensions: electrical and thermal conductivity,” *Phys. Rev. B - Condens. Matter Mater. Phys.*, vol. 71, pp. 110421-1–8, 2005.

[47] W. Obitayo and T. Liu, “A review: carbon nanotube-based piezoresistive strain sensors,” *Journal of Sensors*. pp. 1–15, 2012.

[48] Q. Cao and J. A. Rogers, “Ultrathin films of single-walled carbon nanotubes for electronics

and sensors: a review of fundamental and applied aspects," *Adv. Mater.*, vol. 21, no. 1, pp. 29–53, 2009.

[49] S. Khan, L. Lorenzelli, and R. S. Dahiya, "Technologies for printing sensors and electronics over large flexible substrates: a review," *IEEE Sens. J.*, vol. 15, no. 6, pp. 3164–3185, 2015.

[50] T. N. Tallman and K. W. Wang, "Damage and strain identification in multifunctional materials via electrical impedance tomography with constrained sine wave solutions," *Struct. Heal. Monit.*, vol. 15, no. 2, pp. 235–244, 2016.

[51] K. J. Loh, J. P. Lynch, B. S. Shim, and N. A. Kotov, "Tailoring piezoresistive sensitivity of multilayer carbon nanotube composite strain sensors," *J. Intell. Mater. Syst. Struct.*, vol. 19, no. 7, pp. 747–764, 2007.

[52] E. T. Thostenson and T. W. Chou, "Carbon nanotube networks: sensing of distributed strain and damage for life prediction and self healing," *Adv. Mater.*, vol. 18, no. 2837–2841, 2006.

[53] P. Dharap, Z. Li, S. Nagarajaiah, and E. V Barrera, "Nanotube film based on single-wall carbon nanotubes for strain sensing," *Nanotechnology*, vol. 15, no. 3, pp. 379–382, 2004.

[54] J. P. Lynch, C. R. Farrar, and J. E. Michaels, "Structural health monitoring: technological advances to practical implementations," *Proc. IEEE*, vol. 104, no. 8, pp. 1508–1512, 2016.

[55] J. P. Lynch, A. Partridge, K. H. Law, T. W. Kenny, A. S. Kiremidjian, and E. Carryer, "Design of piezoresistive MEMS-based accelerometer for integration with wireless sensing unit for structural monitoring," *J. Aerosp. Eng.*, vol. 16, no. 3, pp. 108–114, 2003.

[56] B. Glisic and D. Inaudi, "Development of method for in-service crack detection based on

distributed fiber optic sensors," *Struct. Heal. Monit.*, vol. 11, no. 2, pp. 161–171, 2012.

[57] J. Ihn and F. Chang, "Detection and monitoring of hidden fatigue crack growth using a built-in piezoelectric sensor / actuator network : I . diagnostics," *Smart Mater. Struct.*, vol. 609, pp. 609–620, 2004.

[58] Y. Wang, J. P. Lynch, and K. H. Law, "A wireless structural health monitoring system with multithreaded sensing devices: design and validation," *Struct. Infrastruct. Eng.*, vol. 3, no. 2, pp. 103–120, 2007.

[59] J. M. W. Brownjohn, "Structural health monitoring of civil infrastructure," *Phil. Trans. R. Soc. A*, vol. 365, no. 1851, pp. 589–622, 2007.

[60] C. R. Farrar and K. Worden, *Structural health monitoring: a machine learning perspective.* Chichester, West Sussex, UK: John Wiley & Sons, 2013.

[61] O. Ditlevsen and H. O. Madsen, *Structural Reliability Methods*. Chichester, UK: John Wiley & Sons, 2007.

[62] D. W. Greve, I. J. Oppenheim, and A. F. Chen, "An instrumented intramedullary implant to monitor strain in fracture healing," *IEEE Int. Ultrason. Symp. IUS*, pp. 1220–1223, 2012.

[63] F. Umbrecht *et al.*, "Wireless implantable passive strain sensor: design, fabrication and characterization," *J. Micromechanics Microengineering*, vol. 20, no. 8, p. 85005, 2010.

[64] R. Melik *et al.*, "Nested Metamaterials for Wireless Strain Sensing," *IEEE J. Sel. Top. Quantum Electron.*, vol. 16, no. 2, pp. 450–458, 2010.

[65] Y. Jia, K. Sun, F. J. Agosto, M. T. Quiñones, M. Toledo, and Q. Nones, "Design and

characterization of a passive wireless strain sensor," *Meas. Sci. Technol.*, vol. 17, no. 11, pp. 2869–2876, 2006.

[66] K. Ariga, J. P. Hill, and Q. Ji, "Layer-by-layer assembly as a versatile bottom-up nanofabrication technique for exploratory research and realistic application," *Phys. Chem. Chem. Phys.*, vol. 9, no. 19, p. 2319, 2007.

[67] B. S. Shim, Z. Tang, M. P. Morabito, A. Agarawal, H. Hong, and N. A. Kotov, "Integration of conductivity, transparency, and mechanical strength into highly homogeneous LbL composites of SWNT for optoelectronics and solar energy harvesting," *Chem. Mater.*, vol. 19, pp. 5467–5474, 2007.

[68] B. S. Shim, Z. Tang, M. P. Morabito, A. Agarwal, H. Hong, and N. A. Kotov, "Integration of conductivity, transparency, and mechanical strength into highly homogeneous layer-by-layer composites of single-walled carbon nanotubes for optoelectronics," *Chem. Mater.*, vol. 19, no. 23, pp. 5467–5474, 2007.

[69] J. N. Coleman, U. Khan, W. J. Blau, and Y. K. Gun'ko, "Small but strong: a review of the mechanical properties of carbon nanotube-polymer composites," *Carbon N. Y.*, vol. 44, no. 9, pp. 1624–1652, 2006.

[70] K. J. Loh, J. Kim, J. P. Lynch, N. W. S. Kam, and N. A. Kotov, "Multifunctional layer-by-layer carbon nanotube–polyelectrolyte thin films for strain and corrosion sensing," *Smart Mater. Struct.*, vol. 16, no. 2, pp. 429–438, 2007.

[71] D. Ryu, F. N. Meyers, and K. J. Loh, "Inkjet-printed, flexible, and photoactive thin film strain sensors," *J. Intell. Mater. Syst. Struct.*, vol. 26, no. 13, pp. 1699–1710, 2015.

[72] B. R. Loyola *et al.*, “Detection of spatially distributed damage in fiber-reinforced polymer composites,” *Struct. Heal. Monit.*, vol. 12, no. 3, pp. 225–239, 2013.

[73] Chris A. Mack, *Fundamental Principles of Optical Lithography: The Science of Microfabrication*. London: John Wiley & Sons, 2007.

[74] N. D. Young, G. Harkin, R. M. Bunn, D. J. McCulloch, R. W. Wilks, and A. G. Knapp, “Novel fingerprint scanning arrays using polysilicon TFT’s on glass and polymer substrates,” *IEEE Electron Device Lett.*, vol. 18, no. 1, pp. 19–20, 1997.

[75] J. Engel, J. Chen, and C. Liu, “Development of polyimide flexible tactile sensor skin,” *J. Micromech. Microeng*, vol. 13, no. 3, pp. 359–366, 2003.

[76] H. Sirringhaus *et al.*, “High-resolution inkjet printing of all-transistor circuits,” *Science.*, vol. 290, no. 2000, pp. 2123–2126, 2000.

[77] H. Gleskova and S. Wagner, “Amorphous silicon thin-film transistors on compliant polyimide foil substrates,” *IEEE Electron Device Lett.*, vol. 20, no. 9, pp. 473–475, 1999.

[78] N. Salowitz *et al.*, “Recent advancements and vision toward stretchable bio-inspired networks for intelligent structures,” *Struct. Heal. Monit.*, vol. 13, no. 6, pp. 609–620, 2014.

[79] Y. Hu *et al.*, “Large-scale sensing system combining large-area electronics and cmos ics for structural-health monitoring,” *IEEE J. Solid-State Circuits*, vol. 49, no. 2, pp. 513–523, 2014.

[80] A. Bsoul, M. Sultan Mohamed Ali, A. Nojeh, and K. Takahata, “Piezoresistive strain sensing using carbon nanotube forests suspended by parylene-C membranes,” *Appl. Phys.*

Lett., vol. 100, p. 213510, 2012.

[81] S. H. Park, Y. J. Kang, and S. Majd, “A review of patterned organic bioelectronic materials and their biomedical applications,” *Adv. Mater.*, vol. 27, no. 46, pp. 7583–7619, 2015.

[82] S. Park, M. Vosguerichian, and Z. Bao, “A review of fabrication and applications of carbon nanotube film-based flexible electronics,” *Nanoscale*, vol. 5, no. 5, pp. 1727–1752, 2013.

[83] C. K. Saner, L. Lu, D. Zhang, and J. C. Garno, “Chemical approaches for nanoscale patterning based on particle lithography with proteins and organic thin films,” *Nanotechnol. Rev.*, vol. 4, no. 2, pp. 129–143, 2015.

[84] A. Burton and J. P. Lynch, “Patterned carbon nanotube sensing skins for strain sensing,” in *Proceedings of the 9th International Workshop on Structural Health Monitoring*, 2013, p. Pages 2779-2786.

[85] K. Loh, *Development of multifunctional carbon nanotube nanocomposite sensors for structural health monitoring*. Ann Arbor, MI, 2008.

[86] J. H. Weng, C. H. Loh, J. P. Lynch, K. C. Lu, P. Y. Lin, and Y. Wang, “Output-only modal identification of a cable-stayed bridge using wireless monitoring systems,” *Eng. Struct.*, vol. 30, no. 7, pp. 1820–1830, 2008.

[87] A. T. Zimmerman, M. Shiraishi, R. A. Swartz, and J. P. Lynch, “Automated modal parameter estimation by parallel processing within wireless monitoring systems,” *J. Infrastruct. Syst.*, vol. 14, no. 1, pp. 102–113, 2008.

[88] D. S. Holder, *ELECTRICAL IMPEDANCE TOMOGRAPHY*. Philadelphia, PA: IOP

Publishing, 2005.

[89] A. P. Calderón, “On an inverse boundary value problem,” *Semin. Numer. Anal. its Appl. to Contin. Phys.*, vol. 25, no. 3, pp. 65–73, 1980.

[90] B. H. Brown, “Electrical impedance tomography (EIT): a review,” *J. Med. Eng. Technol.*, vol. 27, no. 3, pp. 97–108, 2003.

[91] M. Cheney, D. Isaacson, and J. C. Newell, “Electrical impedance tomography,” *SIAM Rev.*, vol. 41, no. 1, pp. 85–101, 1999.

[92] L. Borcea, “Electrical impedance tomography,” *Inverse Probl.*, vol. 18, no. 6, pp. R99–R136, 2002.

[93] K. J. Loh, T. C. Hou, J. P. Lynch, and N. A. Kotov, “Carbon nanotube sensing skins for spatial strain and impact damage identification,” *J. Nondestruct. Eval.*, vol. 28, pp. 9–25, 2009.

[94] T. N. Tallman, S. Gungor, K. W. Wang, and C. E. Bakis, “Tactile imaging and distributed strain sensing in highly flexible carbon nanofiber/polyurethane nanocomposites,” *Carbon N. Y.*, vol. 95, pp. 485–493, 2015.

[95] D. Zhang, L. Ye, D. Wang, Y. Tang, S. Mustapha, and Y. Chen, “Assessment of transverse impact damage in GF/EP laminates of conductive nanoparticles using electrical resistivity tomography,” *Compos. Part A Appl. Sci. Manuf.*, vol. 43, no. 9, pp. 1587–1598, 2012.

[96] C. Viets, S. Kaysser, and K. Schulte, “Damage mapping of GFRP via electrical resistance measurements using nanocomposite epoxy matrix systems,” *Compos. Part B Eng.*, vol. 65,

pp. 80–88, 2014.

[97] T. Takahashi, K. Takei, A. G. Gillies, R. S. Fearing, and A. Javey, “Carbon nanotube active-matrix backplanes for conformal electronics and sensors,” *Nano Lett.*, vol. 11, pp. 5408–5413, 2011.

[98] R. Yarahmadi, A. Safarpour, and R. Lotfi, “An improved-accuracy approach for readout of large-array resistive sensors,” *IEEE Sens. J.*, vol. 16, no. 1, pp. 210–215, 2016.

[99] R. S. Saxena, R. K. Bhan, and A. Aggrawal, “A new discrete circuit for readout of resistive sensor arrays,” *Sensors Actuators, A Phys.*, vol. 149, no. 1, pp. 93–99, 2009.

[100] L. Shu, X. Tao, and D. D. Feng, “A new approach for readout of resistive sensor arrays for wearable electronic applications,” *IEEE Sens. J.*, vol. 15, no. 1, pp. 442–452, 2015.

[101] J. Wu, “Scanning approaches of two-dimensional resistive sensor arrays: A review,” *IEEE Sens. J.*, vol. 17, no. 4, pp. 914–925, 2016.

[102] S. Jönsson, K. Caine-Winterberger, and R. Brånemark, “Osseointegration amputation prostheses on the upper limbs: methods, prosthetics and rehabilitation,” *Prosthet. Orthot. Int.*, vol. 35, no. 2, pp. 190–200, 2011.

[103] J. H. Healey, C. D. Morris, E. A. Athanasian, and P. J. Boland, “Compress® knee arthroplasty has 80% 10-year survivorship and novel forms of bone failure knee,” *Clin. Orthop. Relat. Res.*, vol. 471, no. 3, pp. 774–783, 2013.

[104] P. Kalansuriya, R. Bhattacharyya, and S. Sarma, “RFID tag antenna-based sensing for pervasive surface crack detection,” *IEEE Sens. J.*, vol. 13, no. 5, pp. 1564–1570, 2013.

[105] C. Cho, X. Yi, D. Li, Y. Wang, and M. M. Tentzeris, "Passive frequency doubling antenna sensor for strain and crack detection," *IEEE Sens. J.*, vol. 16, no. 14, pp. 5725–5733, 2016.

[106] J. Kim, Z. Wang, and W. S. Kim, "Stretchable RFID for wireless strain sensing with silver nano ink," *IEEE Sens. J.*, vol. 14, no. 12, pp. 4395–4401, 2014.

[107] X. Yi, C. Cho, J. Cooper, Y. Wang, M. M. Tentzeris, and R. T. Leon, "Passive wireless antenna sensor for strain and crack sensing—electromagnetic modeling, simulation, and testing," *Smart Mater. Struct.*, vol. 22, no. 8, p. 85009, 2013.

[108] S. Caizzone and E. DiGiampaolo, "Wireless passive RFID crack width sensor for structural health monitoring," *IEEE Sens. J.*, vol. 15, no. 12, pp. 6767–6774, 2015.

[109] S. L. Wood and D. P. Neikirk, "Passive sensors for infrastructure monitoring," in *Structures and Materials*, 2009, vol. 7292, p. 729202.

[110] Y. Zhang and L. Bai, "Rapid structural condition assessment using radio frequency identification (RFID) based wireless strain sensor," *Autom. Constr.*, vol. 54, pp. 1–11, 2015.